



# LUND UNIVERSITY

## Technology for biocomputational devices based on molecular motors

Lindberg, Frida

2019

*Document Version:*

Publisher's PDF, also known as Version of record

[Link to publication](#)

*Citation for published version (APA):*

Lindberg, F. (2019). *Technology for biocomputational devices based on molecular motors*. Department of Physics, Lund University.

*Total number of authors:*

1

### General rights

Unless other specific re-use rights are stated the following general rights apply:

Copyright and moral rights for the publications made accessible in the public portal are retained by the authors and/or other copyright owners and it is a condition of accessing publications that users recognise and abide by the legal requirements associated with these rights.

- Users may download and print one copy of any publication from the public portal for the purpose of private study or research.
- You may not further distribute the material or use it for any profit-making activity or commercial gain
- You may freely distribute the URL identifying the publication in the public portal

Read more about Creative commons licenses: <https://creativecommons.org/licenses/>

### Take down policy

If you believe that this document breaches copyright please contact us providing details, and we will remove access to the work immediately and investigate your claim.

LUND UNIVERSITY

PO Box 117  
221 00 Lund  
+46 46-222 00 00

010  
10110  
1010101  
010101010

# Technology for biocomputational devices based on molecular motors

FRIDA WILHELMINA LINDBERG  
DIVISION OF SOLID STATE PHYSICS | LUND UNIVERSITY

0011010101010  
01010101011101  
0010001010111  
010010111010  
11010110101  
0100101010  
101010





Technology for biocomputational devices based on molecular motors



# Technology for biocomputational devices based on molecular motors

*Doctoral thesis*

Frida Wilhelmina Lindberg



**LUND**  
UNIVERSITY

Division of Solid State Physics

Department of Physics

DOCTORAL DISSERTATION

by due permission of the Faculty of Engineering at Lund University, Sweden.  
To be publicly defended on Friday, June 7<sup>th</sup>, 2019 at 09:15 in Rydbergsalen,  
Sölvegatan 14, Lund, for the degree of Doctor of Philosophy.

*Faculty opponent*

Dr. Mihai Irimia-Vladu  
Joanneum Research

<b>Organization</b> LUND UNIVERSITY  Division of Solid State Physics Department of Physics P.O. Box 118, SE-221 00 Lund, Sweden	<b>Document name: DOCTORAL DISSERTATION</b>
	<b>Date of issue: 2019-04-25</b>  Author: Frida Wilhelmina Lindberg
<b>Title and subtitle: Technology for biocomputational devices based on molecular motors</b>	
<b>Abstract:</b>  For many multivariable problems there are no efficient algorithms for finding solutions. To this day, conventional electronic computers mainly solve problems in a sequential manner. This sequential operation prevents problem-solving within a reasonable time-frame due to superpolynomial, and sometimes even exponential, time complexities. Developing powerful parallel computation techniques has therefore gained increasing attention in science and industry to overcome this fundamental limitation.  This thesis is aimed towards developing network-based biocomputation using molecular motors for solving combinatorial problems in a massively parallel manner. Molecular motors have been previously used to compute a small scale subset sum problem encoded into a network of channels and junctions <sup>1</sup> . Here we tackle some of the engineering requirements of upscaling this system. Specifically, we have developed reliable surface treatments for chemical modification, the regeneration of surfaces for a more sustainable fabrication process, the development of high throughput fabrication with nanometre scale resolution, the design optimisation of the graphical encoding and the development of two architectural elements: programmable gates for versatile networks, and electric sensors for label free detection of filaments.  We show how the material chemistry of molecular motor devices can be altered in a controlled way to ensure selective protein binding, only promoting motility in designated areas. To reuse these devices, we developed a method to regenerate the surfaces with a non-destructive approach, which prolongs their life-time and enables them to be used multiple times. We also present a new device system using two new polymer resists with tuneable motility properties.  To be able to fabricate large-scale, high-resolution devices within a reasonable time-frame we optimised the patterning parameters for electron beam lithography. We also show that nanoimprint lithography can be used as a high-throughput, high-resolution fabrication method to pattern the type of structures needed for molecular motor devices. By adjusting the structural design and imprinting parameters we are able to fabricate high aspect ratio patterns that successfully promote motility.  We also demonstrate a method of translating the exact cover problem into the subset sum problem. We present the design optimisation of a large-scale network (~1000 solutions) encoding the two combinatorial problems mentioned, and our progress towards finding a solution using the molecular motor system actin-myosin II as exploratory agents.  Additionally, we describe a method of creating switchable motility to create programmable network-junctions to be able to compute different mathematical encodings. Such dynamic encodings are a necessity for any viable computer. Finally, we present the advancements towards creating an electric sensor for detection of cytoskeletal filaments, using a carbon nanotube as a tripwire, to enable a reliable readout method for highly parallel problem solving.  We conclude with a discussion of future challenges and prospects for network-based biocomputation employing molecular motors in the light of our findings presented here.	
<b>Key words: Molecular motors, nanofabrication, biocomputation, nanostructures</b>	
<b>ISBN:</b> 978-91-7895-131-4 (print) 978-91-7895-132-1 (pdf)	<b>Language:</b> English

I, the undersigned, being the copyright owner of the abstract of the above-mentioned dissertation, hereby grant to all reference sources permission to publish and disseminate the abstract of the above-mentioned dissertation.

Signature 

Date 2019-04-25

# Technology for biocomputational devices based on molecular motors

Frida Wilhelmina Lindberg



**LUND**  
UNIVERSITY

Cover photo by Frida Wilhelmina Lindberg

Back cover photo by Ivan Maximov

pp 1-98 © Frida Wilhelmina Lindberg

Paper 1 © 2018 American Chemical Society (open access)

Paper 2 © 2019 Materials and Research Express (gold open access)

Paper 3 © by the Authors (Manuscript unpublished)

Paper 4 © by the Authors (Manuscript unpublished)

Paper 5 © by the Authors (Manuscript unpublished)

Faculty of Engineering  
Department of Physics  
Division of Solid State Physics

ISBN

978-91-7895-131-4 (print)

978-91-7895-132-1 (pdf)

Printed in Sweden by Media-Tryck, Lund University  
Lund 2019



Media-Tryck is an environmentally certified and ISO 14001:2015 certified provider of printed material. Read more about our environmental work at [www.mediatryck.lu.se](http://www.mediatryck.lu.se)

**MADE IN SWEDEN** 

*To my mother, who showed me how to climb  
Mount Everest without oxygen*

# Table of Contents

<b>Abstract</b> .....	<b>10</b>
<b>Populärvetenskaplig sammanfattning</b> .....	<b>12</b>
<b>Popular science summary</b> .....	<b>14</b>
<b>List of papers</b> .....	<b>16</b>
<b>Abbreviations</b> .....	<b>18</b>
<b>Acknowledgements</b> .....	<b>20</b>
<b>1 Introduction</b> .....	<b>22</b>
<b>2 Background</b> .....	<b>30</b>
2.1 Molecular motor proteins .....	30
2.1.1 The actin-myosin II system .....	31
2.1.2 The microtubule-kinesin system .....	34
2.2 Patterning techniques for molecular motor devices.....	35
2.2.1 Electron beam lithography.....	35
2.2.2 Nanoimprint lithography .....	37
2.3 Solving combinatorial problems .....	38
2.3.1 Alternative parallel computation techniques .....	39
2.3.2 Computing with molecular motors .....	40
<b>3 Surface treatment</b> .....	<b>41</b>
3.1 Motivation and previous work.....	41
3.2 Controlled surface modification (Paper I) .....	43
3.3 Investigation of new polymer resists .....	46
3.4 Surface regeneration (Paper IV) .....	49
3.5 Concluding remarks.....	54
<b>4 Patterning nanostructures</b> .....	<b>55</b>
4.1 Motivation and previous work.....	55
4.2 Process optimisation for EBL (Paper III) .....	56
4.3 NIL for molecular motor structures (Paper II).....	58
4.4 Concluding remarks.....	63

<b>5</b>	<b>Computing with molecular motors</b> .....	<b>64</b>
5.1	Motivation and previous work.....	64
5.2	Conversion of EXCOV into SSP.....	65
5.3	Introducing “reset” junctions.....	65
5.4	Reducing the network size.....	66
5.5	Implementing the 1000 solution network.....	68
5.6	Concluding remarks.....	72
<b>6</b>	<b>Architectural elements</b> .....	<b>73</b>
6.1	Motivation and previous work.....	73
6.1.1	Switchable junctions for programmable gating.....	73
6.1.2	Electric sensors for label free detection.....	74
6.2	Programmable gating (Paper V).....	75
6.3	Electrical detection.....	79
6.4	Concluding remarks.....	84
<b>7</b>	<b>Conclusions and outlook</b> .....	<b>85</b>
	<b>References</b> .....	<b>89</b>

# Abstract

For many multivariable problems there are no efficient algorithms for finding solutions. To this day, conventional electronic computers mainly solve problems in a sequential manner. This sequential operation prevents problem-solving within a reasonable time-frame due to superpolynomial, and sometimes even exponential, time complexities. Developing powerful parallel computation techniques has therefore gained increasing attention in science and industry to overcome this fundamental limitation.

This thesis is aimed towards developing network-based biocomputation using molecular motors for solving combinatorial problems in a massively parallel manner. Molecular motors have been previously used to compute a small scale subset sum problem encoded into a network of channels and junctions<sup>1</sup>. Here, we tackle some of the engineering requirements of upscaling this system. Specifically, we have developed; reliable surface treatments for chemical modification, the regeneration of surfaces for a more sustainable fabrication process, the development of high throughput fabrication with nanometre scale resolution, the design optimisation of the graphical encoding and the development of two architectural elements: programmable gates for versatile networks, and electric sensors for label free detection of filaments.

We show how the material chemistry of molecular motor devices can be altered in a controlled way to ensure selective protein binding, only promoting motility in designated areas. To reuse these devices, we developed a method to regenerate the surfaces with a non-destructive approach, which prolongs their life-time and enables them to be used multiple times. We also present a new device system using two new polymer resists with tuneable motility properties.

To be able to fabricate large-scale, high-resolution devices within a reasonable time-frame we optimised the patterning parameters for electron beam lithography. We also show that nanoimprint lithography can be used as a high-throughput, high-resolution fabrication method to pattern the type of structures needed for molecular motor devices. By adjusting the structural design and imprinting parameters we are able to fabricate high aspect ratio patterns that successfully promote motility.

We also demonstrate a method of translating the exact cover problem into the subset sum problem. We present the design optimisation of a large-scale network (~1000

solutions) encoding the two combinatorial problems mentioned, and our progress towards finding a solution using the molecular motor system actin-myosin II as exploratory agents.

Additionally, we describe a method of creating switchable motility to create programmable network-junctions to be able to compute different mathematical encodings. Such dynamic encodings are a necessity for any viable computer. Finally, we present the advancements towards creating an electric sensor for detection of cytoskeletal filaments, using a carbon nanotube as a tripwire, to enable a reliable readout method for highly parallel problem solving.

We conclude with a discussion of future challenges and prospects for network-based biocomputation with molecular motors in the light of our findings presented here.

# Populärvetenskaplig sammanfattning

Molekylära motorprotein är små biologiska motorer som kan liknas med vilken annan motor som helst i det att de omvandlar energi till rörelse. De finns överallt i våra celler och deras huvudroll är att organisera logistiken inne i cellerna. Många molekylära motorsystem består av två delar: ett spår och en motor som spatserar på spåret. Idag kan vi ta ut hela motorsystemet ur cellen och fästa motorerna på en valfri yta. Efter extraheringen, kan spåren klippas sönder till trådliknande filament, och om vi tillför motorerna bränsle kan de gripa tag i filamenten och transportera dem, ungefär som en rockstjärna som surfar på publikhavet.

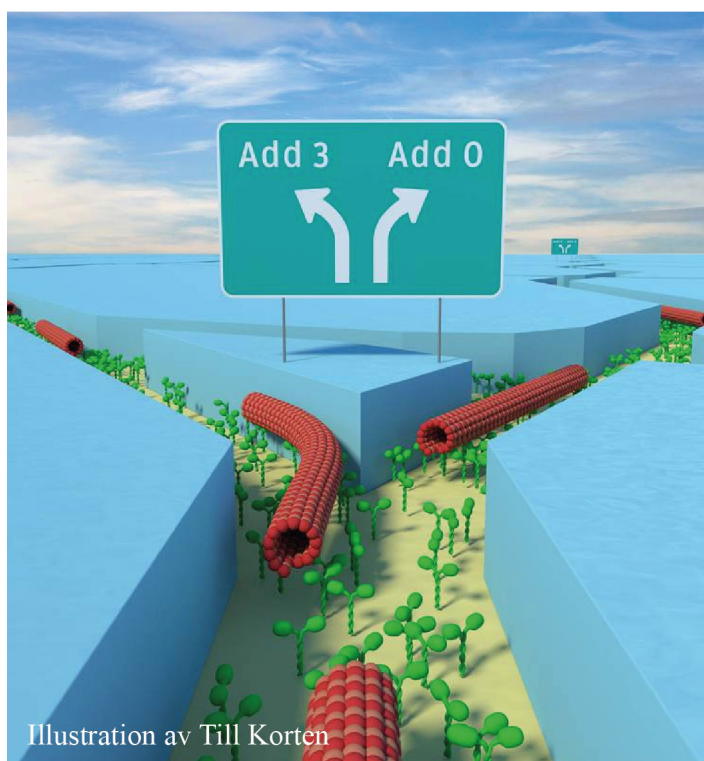
Det här är ju i sig själv ganska fascinerande, men vi skulle också vilja tillämpa det till något lite mer användbart i praktiken. Vad sägs om att försöka ge sig på ett riktigt, riktigt stort matematiskt problem som vanliga seriedatorer kämpar med att lösa? Sådana problem är exempelvis viktiga i optimeringen av rutter och elektriska kretsar, i kodknäckning och i skapandet av nya specifika läkemedel genom att man kan studera vilken form olika proteiner tar beroende på de ingående aminosyrorerna. Även om det låter näst intill otroligt, så är det faktiskt möjligt att utföra beräkningar med molekylära motorer och det är egentligen inte särskilt svårt. Tricket är att skapa en fysisk struktur av sitt matematiska problem, ungefär som en labyrint. Det är det vi kallar nätverksbaserad beräkning med molekylära motorer.

Nätverksbaserad beräkning med molekylära motorer består i princip bara av ett nätverk av sammansatta vägar, precis som vägarna vi kör våra bilar på. Filamenten matas in i ena änden av nätverket, eller vid särskilda positioner, och kan därefter komma ut vid olika platser beroende på vilken väg de väljer inne i nätverket. Varje rutt motsvarar olika beräkningar, och genom att filamenten går på upptäcktsfärd genom hela nätverket kan vi få reda på alla lösningar på en och samma gång. Givetvis gäller det då att vägarna är konstruerade på ett särskilt sätt så de verkligen kodar för olika beräkningar. Det gör vi bl. a. genom att tillsätta särskilda trafikregler som våra upptäcktsresande filament måste följa.

Nästa utmaning är att få våra filament att följa trafikreglerna. Genom att ha väldigt smala leder, kan vi skapa enkelriktade vägar där det inte går att göra U-svängar. Om vi istället breddar vägarna, öppnar vi upp för även mötande trafik. Vi kan också skapa rondeller och tillfälliga avspärningar som definierar vilka rutter som är tillåtna. Önskade svängar kan t.ex. motverkas genom att ha väldigt skarpa korsningar där filamenten bara fortsätter längs med den väg de kommer ifrån. Ett

ännu bättre sätt att förhindra oönskade svängar vore att använda sig av tunnelsystem med broar, men att implementera det kräver ytterligare teknikutveckling innan det är görbart. De mer drastiska avspärningarna kan användas för att ändra på vilka vägar som är tillgängliga. Detta innebär ju som tidigare skrivet, att vi ändrar på vilken beräkning vi utför, vilket gör hela nätverkssystemet flexibelt. Vi kan också skapa vägtullar som registrerar förbigående filament. Om dessa placeras vid de olika utgångarna kan vi registrera resultaten på våra beräkningar.

Som ni kanske redan misstänker så är molekylära motorer inte särskilt stora, vilket innebär att filamenten de driver behöver väldigt, väldigt små vägbanor. I den här avhandlingen beskriver jag hur dessa kan tillverkas med två olika metoder och hur vi selektivt kan placera våra motorer på gatorna inne i vår labyrint. Jag kommer att beskriva hur vi kan skapa reglerbara avspärningar som kan öppnas och stängas, och en tänkbar metod för att implementera elektriska tullar för att räkna förbigående filament. Dessutom kommer jag att beskriva hur vår labyrint ser ut i mer detalj och kommer att försöka förklara varför det är viktigt att utveckla parallella beräkningsmetoder som denna.



**Figur.** Röda filament på upptäcktsfärd genom ett nätverk. Filamenten transporteras ovanpå gröna molekylära motorer. Varje rutt i nätverket representerar en särskild beräkning, vilket innebär att vi kan finna alla lösningar parallellt.

# Popular science summary

Molecular motor proteins are small biological motors, similar to any other motor in that they convert energy into motion. They are omnipresent in our cells, and one of their main roles is to govern the logistics inside the cell. Many motor systems consist of two parts: a track and a motor walking on this track. Today, we can extract the entire motor system and glue the motors to a surface of our choice. Once extracted, the tracks can be cut up into filament-like structures and if we supply our motors with fuel, they're able to latch onto the filaments and kick them forward, like a crowd-surfing rock-star.

As fascinating as this is on its own, we would also like to apply this crowd-surfing to something practically useful. How about tackling a really, really big mathematical problem which our serially computing electronic computers struggle to calculate? Such problems are for instance important for optimising routes and circuits, to break encrypted codes and to create new specific target drugs by studying the shape of different protein compositions. Unbelievable as it may sound, it's actually possible to compute with molecular motors, and it's not really that complicated. The trick is to create a physical structure of this mathematical problem, sort of like a purposefully constructed maze. We call this network-based computation with molecular motors.

Network-based computation with molecular motors is in principle just a network of connected roads, just like the streets we drive our cars on. The filaments enter at a certain point and can exit at different streets depending on what pathway they select. Each street represents a different calculation, and so, by randomly exploring all possible paths we can solve the encoded problem in a massively parallel manner using our filaments as exploratory agents. Of course, the organisation of the streets is carefully designed and there are certain traffic rules that the agents have to obey.

So how can we make our agents follow traffic rules? By using very narrow roads, we can create one-way streets where U-turns are forbidden. If we broaden the streets however, also meeting traffic is allowed. Furthermore, we can implement roundabouts and roadblocks and define what paths are allowed and what paths are not. Turns can for instance be prevented by using very sharp crossing angles, causing agents to just pass straight by. An even better way to prevent turns would be to use tunnels and bridges, though implementing this requires further technology development. The more drastic roadblocks (or gates) can be used to change what

streets are accessible, which in turn means we change the calculation. We can also create check-points, similar to toll-stops or modern parking garages. These check-points don't do much more than register the passing of an exploring agent. However, if we place these check-points at the exiting streets, we can obtain information about what streets were accessible inside the network, which provides us with the correct solutions to the maze.

As you might have gathered already, molecular motors are not very large in size, meaning that the filaments they propel need very, very small roads. In this thesis I describe how we can build these small roads using two different methods and how we can selectively place our motors inside our maze of streets. I describe how we can create switchable roadblocks that can be opened and closed, and I describe our progress toward implementing electric check-points for detecting passing filaments. Furthermore, I describe the maze layout in more detail and explain why it is important to develop parallel computation techniques such as this.

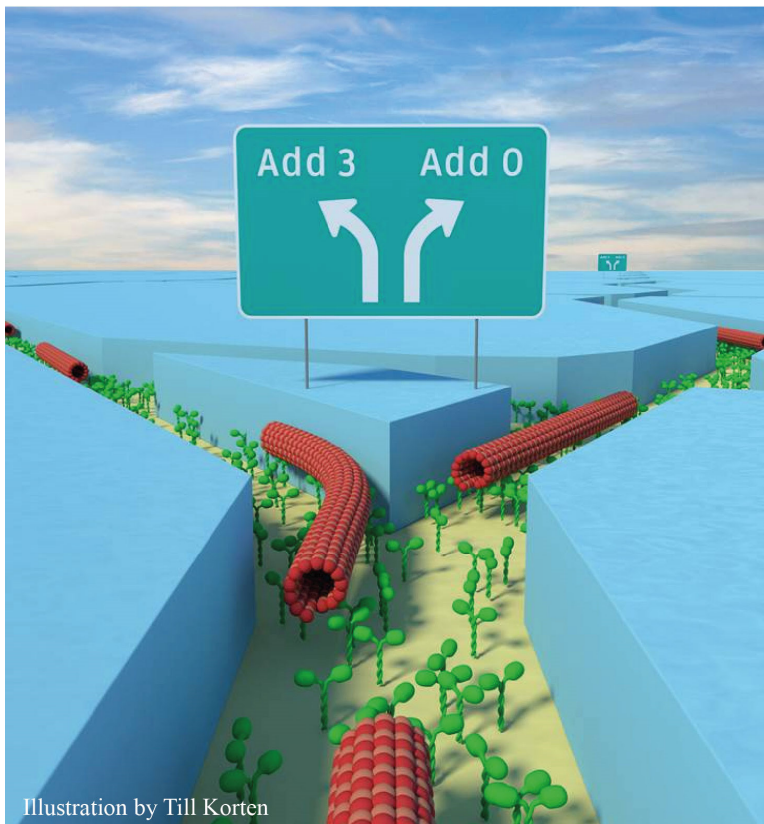


**Figure.** Red filaments crowd-surfing on green motors, exploring all possible paths inside a network. Each path represents a different calculation, enabling the encoded problem to be computed in a massively parallel manner.

# List of papers

This thesis is based on the following papers, referred to as Paper I-V in the text.

**I. Controlled Surface Silanization for Actin-Myosin Based Nanodevices and Biocompatibility of New Polymer Resists**

F. W. Lindberg, M. Norrby, M. A. Rahman, A. Salhotra, H. Takatsuki, S. Jeppesen, H. Linke, A. Månsson

*Langmuir* 34(30) 8777-8784 (2018).

I designed the project and performed the device fabrication and contributed to the motility assay experiments and analysis. I wrote the paper with input from co-authors.

**II. Design and development of nanoimprint-enabled structures for molecular motor devices**

F. W. Lindberg, T. Korten, A. Löfstrand, M. A. Rahman, M. Graczyk, A. Månsson, H. Linke, I. Maximov

*Materials Research Express* 6(2) 025057 (2019).

I designed the project and performed the device fabrication and contributed to the motility assay experiments and analysis. I wrote the paper with input from co-authors.

**III. Nanofabrication technologies for molecular-motor-powered network-based biocomputation structures**

C. Meinecke, T. Korten, F. W. Lindberg, H. Linke, G. Heldt, D. Reuter, S. Diez, S. E. Schulz

*Manuscript*

I designed and performed the device fabrication and analysis for the actin-myosin devices, contributed to the motility assay experiments and analysis and helped write the paper.

**IV. Regeneration of assembled molecular motor-based bionanodevices**

M. A. Rahman, C. Reuther, F. W. Lindberg, M. Mengoni, H. Linke, S. Diez, A. Månsson

*Manuscript*

I designed and performed the device processing of the actin-myosin devices and helped write the paper.

**V. Nanoscaled patterning of active molecular motor structured surfaces for switchable motility**

F. W. Lindberg\*, J. Zhu\*, T. Korten, C. Meinecke, S. Diez, H. Linke

*Manuscript*

I designed and performed some of the device fabrication and analysis and wrote the paper with input from co-authors.

\*Equal contribution

**Related publications**

The following papers are relevant, but outside the scope of this thesis.

**VI. Nanowires for Biosensing: Lightguiding of Fluorescence as a Function of Diameter and Wavelength**

D. Verardo, F. W. Lindberg, N. Anttu, C. S. Niman, M. Lard, A. P. Dabkowska, A. Månsson, T. Nylander, C. Prinz, H. Linke

*Nano Letters 18(8) 4796-4802 (2018)*

I performed the fabrication and growth of the nanowire samples and some of the analysis. I helped write the paper.

# Abbreviations

ATP	adenosine triphosphate
ADP	adenosine diphosphate
CNT	carbon nanotube
CNFET	carbon nanotube field effect transistor
CVD	chemical vapour deposition
DNA	deoxyribonucleic acid
EBL	electron beam lithography
EXCOV	exact cover
FET	field effect transistor
HMM	heavy meromyosin
IPS	intermediate polymer stamp
IVMA	in vitro motility assay
MEK	methyl ethyl ketone
NBC	network-based computation
NIL	nanoimprint lithography
NP	non-deterministic polynomial time
PEG	poly(ethylene glycol)
PMMA	poly(methyl methacrylate)
PMSF	phenylmethane sulfonyl fluoride
PNIPAM	poly( <i>N</i> -isopropylacrylamide)
PGMA	poly(glycidyl methacrylate)
T-NIL	thermal nanoimprint lithography
TEM	transmission electron microscope

TMCS	trimethylchlorosilane
SDS	sodium dodecyl sulphate
SSP	subset sum problem
UN	United Nations
UV	ultra violet
UV-NIL	ultra violet nanoimprint lithography
UVL	ultra violet lithography
3D	three dimensional

# Acknowledgements

Looking back at all the hard work, I know I would not be where I am today without the support and help from those around me. There are a few people I would like to give special thanks to:

To begin with, I would like to say thank you to my dearest supervisors, Heiner Linke and Alf Månsson, who told me that nothing is impossible and who opened up an entirely new world to me. Nothing will ever be the same again. Thank you for giving me space and freedom to grow and learn, and to catch me and guide me when I needed it the most. I am forever grateful for all you have done for me.

I've had the great pleasure of working with the best team for none less than two EU-projects in a row. A special thank you to Till Korten, you are real a champion and your skills seemingly endless, thank you for always being so helpful and supportive. To Stefan Diez, you light up the room with your presence and deep knowledge, and to Dan Nicolau Jr who mesmerises and amazes me. To Adam Micolich, your creativity and innovation is so extremely inspiring, there is never a dull moment working with you. To Marlene Norrby, Ashik Rahman and Aseem Salhotra, thank you for never giving up and always staying positive and supportive when I a hundred times over have yelled "this will be the one, I have a great feeling about this one!" Without your hard work this project would not have come this far, I owe you a great thank you. To Cordula Reuther, Sönke Steenhusen, Christoph Meinecke, Danny Reuter, Georg Heldt, Thomas Blaudeck, Venu Vemula and Hillel Kugler, it has been such a pleasure to work with you and to get to know you, your expertise has really driven us forward. And to my wonderful bio4comp fellows in Lund for making hard work so enjoyable, Jingyuan Zhu, Pradheebha Surendiran and Roman Lyttleton, thank you. Especially Roman, the endless hours we've spent in the lab, day and night and all the hours we spent on the phone and e-mail when you lived in Oz, your support and hard work has meant the world to me. And to Gerda Rentschler, the way you keep track of every detail and keep us all together and looking perfect, your tireless efforts are nothing less than amazing.

To Adam Burke and Mercy Lard, the first few years would not have been the same without you, thank you for everything.

To the people who keep the wheels turning, our past and present brilliant lab and administrative staff, I could spend pages and pages on how much you have helped

me through the years, I am so incredibly grateful to each and every one of you, especially to the ones I have pestered the most over the years: Louise Baldetorp, Charlotte Solberg, Anders Kvennefors, Mariusz Graczyk, Håkan Lapovski, George Rydnemalm, Janne Mårtensson, Johanna Mosgeller, Sören Jeppesen, Maria Huffman, Ivan Maximov, Dmitry Suyatin, Bengt Mueller, Peter Blomqvist, Mia Hedin, Margareta Forsberg, Eva Lenhoff, Marica Kolobaric, Abdul-Rehman Hakam and Line Lundfald, but also to all those who I have not mentioned by name here, a great thank you to you all, so much of what I have learnt over the years I owe to you and I am truly blessed to have learnt from such experts.

To my office mates Mercy, Gustav, Dmitry, Trung, Xulu, Vilgaile, I-ru, Nicklas, Laura, David, Florinda, Elke, Rebekah, Cassie and Inga, there is a special, deep bond between people who've shared an office together. Thank you for all the laughs we've had over the years. And to all my other wonderful colleagues at ftf, Reza, Oskar, Artis, Kush, Damiano, Lukas, Irene, Thanos, Bao, Anette, Neimantas, Malin, Anders, Kalle, Sara, Maria, Christelle, Stefan, Enrique, Pyry, Gaute, Jason, Magnus, Olof, Robert, David, Bekmurat, Jonatan, Sven, Zhen and the list goes on, thank you for making every day so perfect, for wonderful collaborations and heart-warming conversations filled with support and solidarity, thank you all for sharing your knowledge so freely and for such great inspiration.

An extra thank you to my trainers and coaches over the years, who taught me that I can do anything I set my mind to, that hard work pays off and that stopping is not an option, who inspire me to push harder and be the very best I can be every day and to never give up. This I take with me forever, and apply to all of life, including work and academia.

And finally, to my family and loved ones, Molly, Normha, Pentti, Nadia, Sarah, Henrik, Jenny, Johan, Jan, Annica, Nix, Nox and Lady for always being present or just one phone call away, I love you all and I would not be the person I am today without you.

Frida Wilhelmina Lindberg, Lund 2019

# 1 Introduction

Nanotechnology is often described as the manipulation of matter at a very small scale, in the range 1 to 100 nanometres ( $1-100 \cdot 10^{-9}$  m). It is an interdisciplinary field, where the laws of physics, biology, chemistry, materials science and engineering all blend and have to be considered together. The following text is a truly interdisciplinary thesis within nanotechnology, where all the fields mentioned above have been taken into consideration. The goal of this work has been to develop the requirements for a large-scale parallel computer based on molecular motors for solving combinatorial problems.

Naturally, the complexity of any computational problem grows when the number of variables that need to be observed increases. For mathematical problems with a combinatorial nature, an increase in the number of variables causes a superpolynomial, and sometimes even exponential, growth in time complexity. Let's assume a doctor, Sarah, is specialised in treating people suffering from the plague. The United Nations (UN) needs her to travel across the world to train and treat people as soon as possible. Sarah can therefore, not afford to re-visit a country as this would cause an international diplomatic crisis and outrage of why UN-funding is misdirected to privilege one country over another. What route can Sarah take, allowing her to cover all countries, exactly once as fast as possible before the disease spreads further? To find the answer to this question, all possible routes need to be explored. And as the number of countries Sarah needs to visit increases, so does the computational complexity and thus, the problem blows up exponentially.

Combinatorial problems like the one Sarah encountered, are known as non-deterministic polynomial time (NP) problems, problems with multiple solutions that cannot be verified within a polynomial timeframe<sup>2</sup>. These problems are very challenging for electronic computers that work in a sequential manner as often, no efficient algorithms exist and instead, parallel computation techniques are needed. To this date, existing parallel computation techniques such as, parallel electronic computers<sup>3,4</sup>, DNA computation<sup>5-7</sup>, microfluidics based computation<sup>8</sup> and quantum computation<sup>9</sup>, all have their own drawbacks and limitations for upscaling into more complex systems (further discussed in Chapter 2).

In this thesis we further explore a parallel computation method based on molecular motors. Molecular motors are a class of proteins that convert chemical energy into mechanical motion in a highly energy-efficient manner<sup>1,10,11</sup>, enabling them to

propel their corresponding cytoskeletal filamentous proteins. In the *in vitro* motility assay<sup>12–15</sup> (IVMA) the motors are first isolated in functional form from the cell and can then be adsorbed onto a surface with maintained function. The IVMA has enabled many new insights into the physiological properties of molecular motor systems<sup>16–19</sup>, and has also gained interest as a basis for nanotechnology applications<sup>1,20–23</sup>. The type of motility assay used here is the gliding assay<sup>15</sup>, where the molecular motors are immobilized on the substrate, while the filaments are propelled along the surface in a random motion. This motion can be directed by introducing chemically<sup>24,25</sup> and physically<sup>26–31</sup> confining tracks, which has led to the exploration of various lab-on-a-chip applications<sup>1,21,32,33</sup>.

In our motility assay system, we build a “flow cell” comprised of a thin, glass coverslip onto which we paste two pieces of tape spaced a few mm apart (**Figure 1.1**). The surfaces we study are mounted onto the tape, face down, enabling addition of protein and buffer solutions via capillary forces. We image the gliding assay through the glass coverslip using an inverted fluorescence microscope and fluorescently labelled actin filaments. To direct the motion of filaments, we use a combination of physically and chemically confining tracks. The nanostructures are created by lithography, providing channels with polymer walls. The channel floors are chemically treated to allow motor binding in a motility-promoting manner, while the walls are treated to inhibit this binding. The binding mechanism and motor confinement will be further discussed in Chapters 2 and 3, and the patterning of nanostructures is further discussed in Chapter 4.

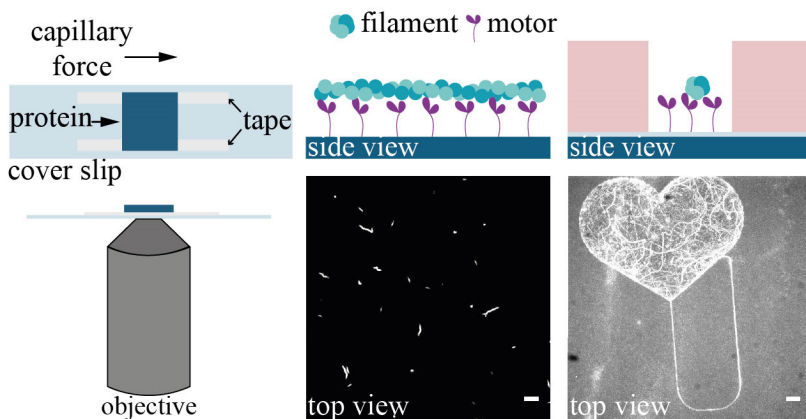


**Figure 1.1.** Schematic illustrations and fluorescence micrographs of (left) a flow cell and our experimental set-up, (middle) an *in vitro* motility assay on a flat surface and (right) on a structured surface. The flow cell consists of a glass slide with two pieces of tape onto which the sample is mounted upside down, creating an enclosed volume for the protein assays. The flow cell is mounted face down onto a microscope and imaged using a fluorescence microscope. Motors bound to a flat surface propel filaments in a random motion through active transport. The fluorescently labelled filaments appear as bright snakes on the dark surface. The nanostructured surface physically and chemically confines the motor system, only allowing the filaments to move from the large heart into the channel and back again. The lower right micrograph shows the maximum intensity of a 60 s time-lapse movie. The scalebar is 5  $\mu\text{m}$  in both fluorescence micrographs.

The use of molecular motor systems for network-based computation (NBC) was first reported in 2016<sup>1</sup>, in the form of a proof-of-principle small scale network solving a simple combinatorial problem known as the subset sum problem. The subset sum problem<sup>34</sup> (SSP) asks what sums are attainable given a set of numbers. For instance, given the set (2, 3, 9), the possible sums and correct solutions, correspond to (0), 2, 3, 5, 9, 11, 12, 14. For small sets, such as the one demonstrated<sup>1</sup>, it seems trivial and unnecessary to create a computer to find the solutions. However, the SSP is of a combinatorial nature as all combinations of numbers must be explored by brute force in order to find the correct answers. Therefore, the solution space and thus, the time required to solve the problem grows exponentially,  $2^n$ , with the number of integers<sup>6,34,35</sup>,  $n$ .

The motor systems are confined by a network of channels (**Figure 1.2**) consisting of two types of junctions: pass and split. The pass junctions are basic cross-overs, where filaments are supposed to continue along the straight path from which they came. At split junctions however, the filaments can turn and thus, spread across the network. The position of the split junctions define what numbers are encoded in the network, as this defines how far right a filament can travel before making a turn, and thus, at what positions filaments can exit the network. The farther right the filaments exit the higher the resulting sum.

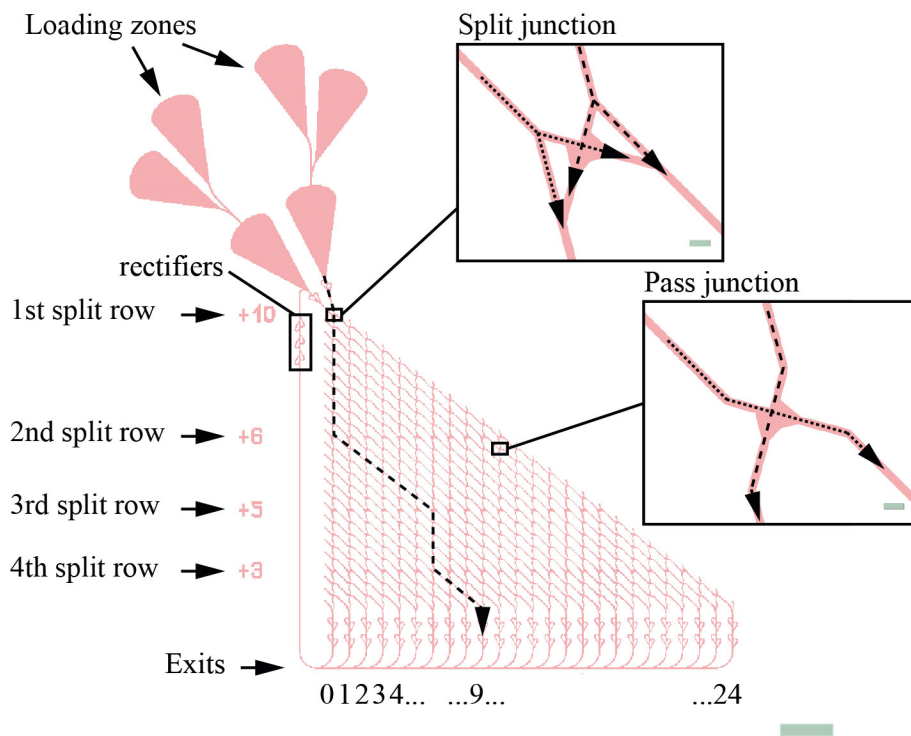


**Figure 1.2.** Schematic layout of a biocomputational network of the combinatorial problem subset sum encoding the numbers (10, 6, 5, 3). Filaments enter the network of split and pass junctions through large areas called loading zones. If the filaments try to enter the network from the wrong way, they are re-directed by rectifiers<sup>1</sup>. At the pass junctions the filaments travel straight along the path they came from, and at split junctions they can turn either left (straight down) or right. The farther right (when looking at the network at from above) a filament moves, the higher the resulting sum. The number of pass junctions between two split rows match the numbers encoded. In the example path (dashed line) the filament travels straight down through the first split junction encoding the number 10 (nothing is added). At the second split junction, encoding the number 6, the filament turns and moves right 6 pass junctions (+6). At the third split junction, encoding the number 5, the filament turns again and moves down (nothing is added), but at the fourth split junction, encoding the number 3, the filament turns right again and travels even farther right, 3 pass junctions (+3), and eventually exits at exit number  $6+3=9$ . The scalebar in the split and pass junction figures is 500 nm. The scalebar in the big figure is 25  $\mu\text{m}$ .

In this thesis we mainly use the relatively small<sup>36</sup> ( $\sim 10$  nm wide) actin-myosin II system. The semiflexible<sup>11,37</sup> filamentous actin is propelled by proteolytically cleaved myosin-II fragments (known as heavy meromyosin (HMM)), at high speeds<sup>11</sup>. To some extent, we also use the microtubule-kinesin system which has larger<sup>11</sup> ( $\sim 25$  nm wide) and more rigid microtubules<sup>11,37</sup> that are propelled by kinesin-1 motors at about 10-fold lower velocities<sup>38</sup>. The networks for the actin-myosin II system are fabricated with polymer resist channel walls that are patterned by electron beam lithography on channel floors made of  $\text{SiO}_2/\text{Si}$  substrates which are chemically modified to promote motility (described further in Chapter 3). This thesis tackles some of the engineering requirements related to upscaling the proof-

of-principle network demonstrated in 2016<sup>1</sup> and also demonstrates a method to translate another combinatorial problem, exact cover, into the SSP and describes our progress towards solving a larger scale network in the ~1000 solution range.

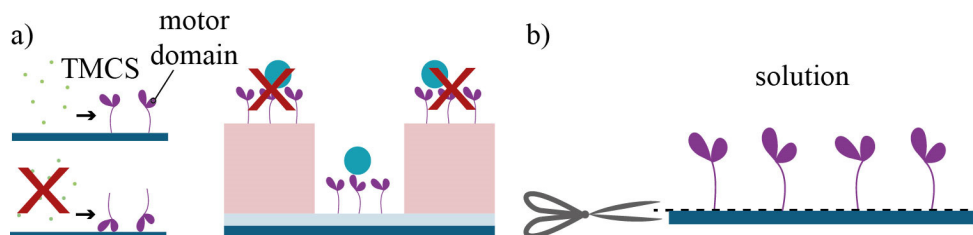


**Figure 1.3.** Schematic illustration of a) molecular motor-binding to a surface. To chemically confine the motor systems we need to ensure the motors bind in an upright, motility-promoting manner with the motor domains protruding into the solution. b) To enable a sustainable fabrication method we developed a procedure to cleave the motors off the surface, allowing the samples to be reused without disassembling the flow cell.

To chemically confine molecular motor systems, the surface chemistry must differ between the motility promoting (channel floor) and motility inhibiting (channel wall) area. Furthermore, the material chemistry must be compatible with the molecular motor system used, both in relation to toxicity as well as protein binding to ensure the motors bind with the motor domain protruding into solution (**Figure 1.3a**). The binding mechanism of HMM to a surface is complex and depends on both the surface charge<sup>39</sup> and the surface hydrophobicity<sup>40–42</sup>. Previous studies<sup>39,43</sup> have shown that trimethylchlorosilane (TMCS) functionalised SiO<sub>2</sub> surfaces created by chemical vapour deposition (CVD) promote high-quality actin filament motility. In these studies, the CVD process occurred in a fully saturated TMCS system. Initially, we used a similar process but noticed inconsistencies in sample behaviour with respect to both measured contact angles and the actin filament sliding velocities for different sample batches. We linked these observations to the limitations of the CVD process performed in a relatively uncontrolled environment. To provide more reliable results, we developed a CVD tool to enable silanisation in a more controlled manner, enabling us to tailor the surface hydrophobicity without changing the chemical composition of the surface (Paper I).

Furthermore, the re-use of nanostructured devices within molecular motor-based applications is highly desirable due to the expensive and time-consuming fabrication procedures, as well as from a sustainable perspective, as less material is used and samples shipped elsewhere can be recycled and used for multiple experiments. We therefore, developed a process for chemically cleaning the nanostructures (**Figure 1.3b**) from old proteins without disassembling the nanofluidic flow cells using a combination of the non-selective protease Proteinase K and the non-ionic surfactant Triton X100 (Paper IV).

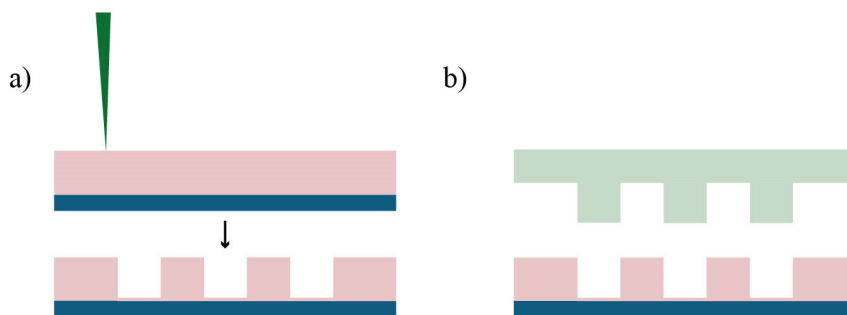


**Figure 1.4.** Schematic illustration of a) electron beam lithography and b) nanoimprint lithography for molecular motor devices. In electron beam lithography an electron beam is scanned across the surface, selectively exposing specific regions, causing cross-linking or cleavage of the polymer, making it more or less soluble in a developer. In nanoimprint lithography a polymer is heated above its glass transition temperature and a stamp is pressed down to physically imprint structures. Both methods enable high-resolution nanoscaled patterning.

The required dimensions for molecular motor structures depend on the motor system used. Channels can be designed so that they represent “one-way streets” by taking advantage of the persistence length of the filaments<sup>27,44</sup>, where an advantage of more rigid filaments are that wider channels can be used. The actin-myosin system requires high-resolution fabrication techniques based on the necessary feature size (channel widths around 200-300 nm<sup>27</sup>) to prevent U-turns. Such structures are patterned by electron beam lithography (EBL), where selective areas of a polymer are exposed with an electron beam causing cross-linking or cleavage of polymer chains (**Figure 1.4a**). This provides high flexibility in pattern design but at a very low throughput. We optimised the processing parameters for a new sensitive electron beam resist, CSAR62 in our currently available electron beam lithography system as well as a newly purchased system to improve the throughput of patterning larger-scale computational networks (Paper III).

Another fabrication method that can be used to achieve high-resolution patterns but with a higher throughput is nanoimprint lithography (NIL) where a stamp is used to imprint a polymer (**Figure 1.4b**). NIL was first used for fabricating narrow channels (100-400 nm) for molecular motor devices in 2005 by Bunk et al<sup>45</sup>. However, structures for molecular motors also require large open areas, “loading zones” (see **Figure 1.2**), to collect the filaments from solution and funnel them towards the connecting channels<sup>1,21</sup>. Such structures, with a large width relative to the height, are difficult to imprint with NIL as the imprinted polymer needs to be displaced across large distances<sup>46</sup>. We extended the previous imprinting study<sup>45</sup> for molecular motor devices to include a method of fabricating a new type of loading zone. By introducing pillars inside the loading zones, we could provide close by regions into which the resist could be displaced (Paper II). We also extended the previously results by optimising the process for a new imprinting resist, TU7, which has a low glass transition temperature allowing imprints below 100°C.

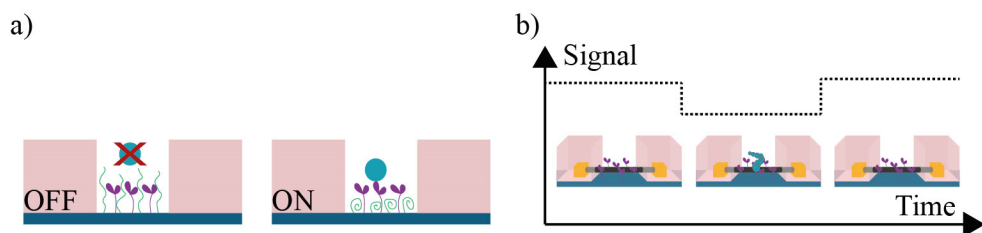


**Figure 1.5.** Schematic illustration of a) a programmable gate using the thermoresponsive polymer PNIPAM to switch between a blocked (OFF) and unblocked channel (ON) and b) a nanoFET with a carbon nanotube to create an electrical detection method enabling label-free and microscope-free experiments.

Allowing imprinting of large-scale networks and the re-generation of surfaces for multiple use, creates an attractive and sustainable computational method. However, to create a versatile computer that can be used to encode different numbers, a programmable gate is needed. Such a gate can be used to transform pass junctions into split junctions, and vice versa, by blocking and unblocking certain paths (**Figure 1.5a**). Initial studies<sup>47</sup> for blocking and promoting the motility of microtubules were done on Au patterned surfaces, and demonstrated the proof-of-principle of using a thermo-responsive polymer poly(N-isopropylacrylamide) (PNIPAM) to create physical roadblocks. At low temperatures, PNIPAM resides in an extended form, blocking the molecular motors, inhibiting motility. If the temperature is increased, the polymer curls up and exposes the motors, and the roadblock is lifted. We continued this work, aiming to create a gating mechanism inside our channel structures, to create switchable, and thus programmable, networks by selective patterning of a polymer linker for PNIPAM grafting (Paper V).

Another important enabler for large-scale biocomputation, is technology to detect a large number of filaments passing different check-points, e.g., at the network exits. If this detection is done electrically, the need for fluorescent labels becomes redundant, and neither labels nor microscopes need to be used. Additionally, electrical detection and read-out would enable a direct interface to traditional, electronic computers. We have begun development towards an electrical readout method using a single-walled carbon nanotube (CNT) as a nanoscale field effect transistor<sup>48</sup> (nanoFET) (**Figure 1.5b**). CNTs have previously been used as nanoFETs<sup>49–51</sup>, but to the best of our knowledge, not for detecting the passing of an unbound protein. A voltage is applied across the CNT, creating a current sensitive to the local charge environment. As a charged particle, e.g., a protein filament, passes in close proximity of the CNT, the charge environment changes which modulates the electric output signal. Therefore, the passing of a charged particle should be detectable as a function of time. Our molecular motor systems require buffer solutions with different ionic constituents. This affects the distance at which our protein charges can be detected as the electrolytes screen the electric potential.

We examined the effect of the local environment in terms of ionic strength; how close the filaments need to pass the CNT and the quality of motility at very low ionic strengths. We found that the CNTs have to be placed on top of pedestals to allow filaments being propelled above the surface to graze across the CNT, and that there is a trade-off between retaining function of the biological system and what gap size is possible between filament and CNT.

The developments presented in this thesis, provide stepping stones towards using large-scale biocomputational networks to solve combinatorial problems in a massively parallel manner. Further development of parallel computation techniques for solving these types of problems, opens up for exploring entirely new scientific questions that previously were impossible to manage within, e.g., artificial intelligence<sup>52,53</sup>, complex studies of protein folding<sup>54,55</sup>, network route optimisations<sup>56</sup> and many more.

The remaining chapters of this thesis are laid out as follows:

Chapter 2 introduces molecular motor systems, in particular the actin-myosin II and microtubule-kinesin I system in more detail, to provide a background for how these motor systems can be used in nanotechnology devices, in particular for computation. A theoretical background on the type of computational problems studied is also introduced. Furthermore, a brief review of the two main patterning techniques (EBL and NIL) used throughout this thesis is presented.

Chapter 3 focuses on the surface chemistry of the devices and describes how surfaces can be modified in a controllable manner to ensure selective motility (Paper I) and how surfaces can be cleaned and reused multiple times (Paper IV).

Chapter 4 describes the optimisation and development of nanopatterning for EBL (Paper III) and NIL (Paper II) to enable higher throughput fabrication of large networks without loss of structural resolution.

Chapter 5 demonstrates our efforts towards solving an upscaled network encoding the combinatorial problem exact cover. The algorithm for translating the exact cover problem into the previously demonstrated subset sum problem is presented as well as the design optimisation for this new network and preliminary results on a  $10^3$ -solution-space order.

Chapter 6 presents the progress towards developing a programmable gate for switching the number encoding inside a network (Paper V), and the progress towards developing an electric readout method using a CNT as a nanoFET.

Chapter 7 summarizes the results presented and describes future improvements and developments in this area.

# 2 Background

*This chapter aims to provide sufficient background knowledge for the reader to be able to understand the results presented in the chapters to follow, and to appreciate their scientific significance. A brief introduction to molecular motor systems is given, in particular the actin-myosin II and the microtubule-kinesin I system, together with a few notes on what to consider when selecting a new system. The second part of this chapter introduces the two main patterning techniques used in this thesis: electron beam lithography and nanoimprint lithography. The third and final part of this chapter presents the type of mathematical problems that are of interest in parallel computation and how these can be solved. A short introduction is given to some pertinent techniques including quantum computation and DNA computation, as well as an introduction of network-based computation with molecular motors.*

## 2.1 Molecular motor proteins

Molecular motors are proteins that govern the active and directed movement in all eukaryotic cells. The motors convert chemical energy of adenosine triphosphate (ATP) hydrolysis into mechanical motion in a highly energy-efficient manner<sup>1,10,11</sup>. In the *in vitro* motility assay<sup>12–15</sup> (IVMA) the motors are isolated from the cell and adsorbed onto a surface. In the presence of ATP, the corresponding cytoskeletal filaments are propelled in a random direction through active transport by the motors. This motion can be directed using chemically<sup>24,25</sup> and physically<sup>26–31</sup> confining tracks, but the efficiency of the guiding along these tracks is highly dependent on the persistence length of the filaments<sup>24,27,31,44</sup>, i.e., their flexural rigidity. The most important properties to consider when choosing a molecular motor system for nanotechnology applications are:

- Persistence length: defines the dimension requirements of the nanostructures. Very flexible filaments require narrow tracks<sup>24,27</sup> to ensure unidirectional motion but also enable very compact nanostructures as the filaments can turn through steeper radii. More rigid filaments allow for larger nanostructures which simplifies fabrication but puts constraints on

imaging techniques due to the increase in size as the structures will expand outside the imaging field of view.

- Filament gliding velocity: defines how fast filaments run through a device and what temperature range<sup>57</sup> the system needs to be operated in. It may be preferential to decrease the filament speed in certain devices or regions to facilitate readout or detection, while larger nanostructure systems could benefit statistically from higher velocities due to an increased current density of filaments.
- Processivity: defines if the filaments are more or less likely to detach from the motors and is usually negatively correlated with the gliding speed. Non-processive motors require many motors to propel the filaments, making it difficult for filaments to escape via side-wall interactions. These motors detach readily from their filaments, usually providing higher gliding velocities than processive motors.

### 2.1.1 The actin-myosin II system

Striated muscle tissue is composed of repeating units known as sarcomeres which consist of thin actin containing filaments and thicker myosin II containing filaments<sup>58</sup> (**Figure 2.1**). Upon activation, the filaments slide along each other driven by a cyclic binding-unbinding process between myosin motor domains and actin filaments. This, so called the cross-bridge cycle, is the molecular basis for muscles contraction<sup>59,60</sup>.

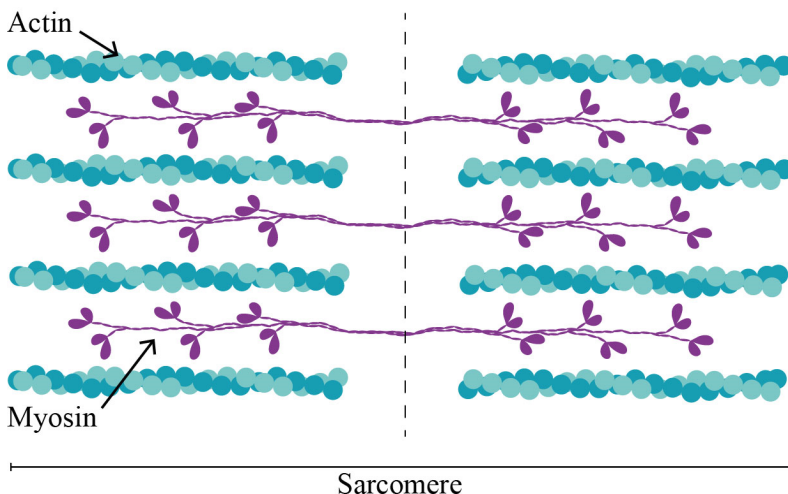


**Figure 2.1.** Schematic illustration of a sarcomere, showing the actin filaments in aqua shades and myosin filaments in purple. Figure freely interpreted from<sup>61</sup>.

The actin filaments consist of globular monomers, G-actin, arranged in a helical structure<sup>62</sup> which creates polar filaments, F-actin, with one end denoted the plus end or barbed end and the other the minus end or pointed end. During actin polymerization, the filament preferentially elongates by monomers binding to the plus end<sup>63</sup>, hence the terminology. Each actin filament has a diameter of  $\sim 9$  nm<sup>36</sup> and can grow several micrometres long. Due to their structural composition, actin filaments are semi-flexible on the length scale of a cell with a persistence length around 10-20  $\mu\text{m}$ <sup>11,37</sup>. In this thesis, mainly rhodamine-phalloidin labelled actin filaments have been used, which usually have a persistence length in the upper part of the mentioned range<sup>37,64,65</sup>.

The myosin super family consists of 35 different myosin classes<sup>66,67</sup>. In this thesis we have used (rabbit) skeletal muscle myosin II. Muscle myosin II forms thick bipolar filaments with globular units, heads, that are around 10 nm long and 5 nm wide. These heads contain the motor domains: a catalytic site for ATP turnover and positively charged surface loops with central roles in actin binding<sup>68</sup>. Myosin II can be proteolytically cleaved into subunits<sup>69</sup>, resulting in light meromyosin and heavy meromyosin (HMM). The HMM tail is negatively charged and forms a coiled-coil consisting of  $\alpha$ -helical segments of the two myosin heavy chains that make up the bulk of each myosin molecule<sup>70</sup>. **Figure 2.2** shows two transmission electron microscope (TEM) images of negatively stained myosin II (**a**) and HMM bound to actin filaments (**b**). Both samples have been stained with uranyl acetate<sup>71</sup> on square meshed TEM Cu grids with pioloform membranes. The concentration of myosin II is 2550  $\mu\text{g/ml}$  and the actin-HMM concentration is 630  $\mu\text{g/ml}$ , both contained in LISS buffer (1 mM  $\text{MgCl}_2$ , 10 mM MOPS, 0.1 mM  $\text{K}_2\text{EGTA}$  in 1M KOH) with 3M KCl. The images are taken with a JEOL JEM-1400 Plus TEM at 100 kV acceleration voltage.

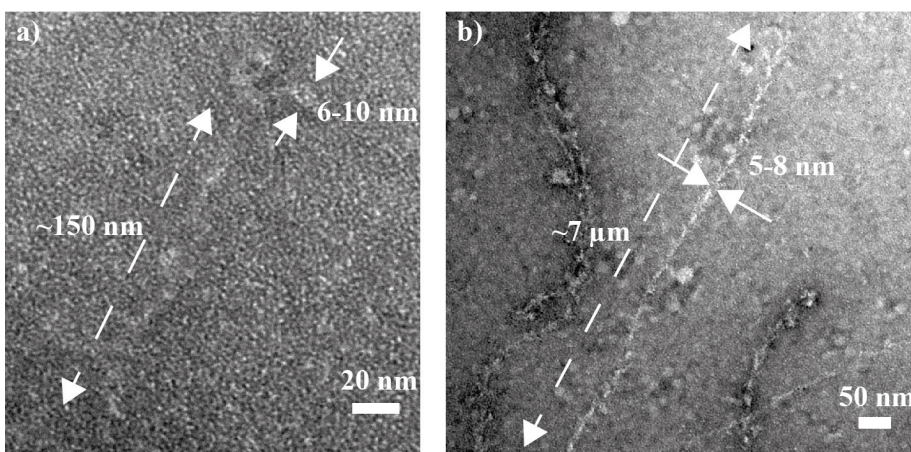


**Figure 2.2.** TEM images of negatively stained myosin II (a) and HMM bound to actin filaments (b).

### *The cross-bridge cycle*

The cross-bridge cycle is a cyclic process of binding and unbinding of myosin to actin powered by ATP. Upon binding of an ATP molecule, myosin undergoes a conformational change<sup>60,72</sup> that lowers the actin-myosin binding affinity (**Figure 2.3a**). Associated with hydrolysis of ATP into adenosine diphosphate (ADP) and inorganic phosphate ( $P_i$ ), the myosin motor undergoes a larger conformational change, forcing the head with its lever arm structure into a pre-power stroke, cocked position (**Figure 2.3b**). Initially, the myosin binding sites on actin filaments are blocked by two proteins: troponin and tropomyosin. When troponin binds  $Ca^{2+}$  it undergoes a conformational change<sup>73</sup> which in turn induces the position of tropomyosin to shift, allowing myosin to bind to actin. The binding of myosin to actin (**Figure 2.3c**) leads to an accelerated dissociation of  $P_i$  (**Figure 2.3d**) followed by the release of ADP (**Figure 2.3e**). These chemical changes are closely associated with a force-generating structural change; a swing of the lever arm creating a power-stroke, that pulls the actin filaments toward the centre of the sarcomere. The cycle is repeated if a new ATP molecule binds to the myosin motor. Thus, each cycle or “step” ( $\sim 10$  nm)<sup>74</sup> only consumes one ATP molecule under physiological conditions which corresponds to approximately 25 kT ( $100 \cdot 10^{-21}$  J)<sup>10,11</sup>. This makes these motors highly energy efficient with a maximum thermodynamic efficiency for an ensemble of motors of up to  $\sim 50\%$ <sup>10</sup>. Furthermore, myosin II always moves toward the plus end of an actin filament and is a non-processive motor, allowing propulsion of actin filaments at high velocities ( $\sim 10$   $\mu\text{m/s}$ )<sup>11</sup>.

As mentioned in the introduction, we use a combination of TMCS-derivatised channel floors and polymer channel walls to chemically and physically confine the actin-myosin II system in our devices.

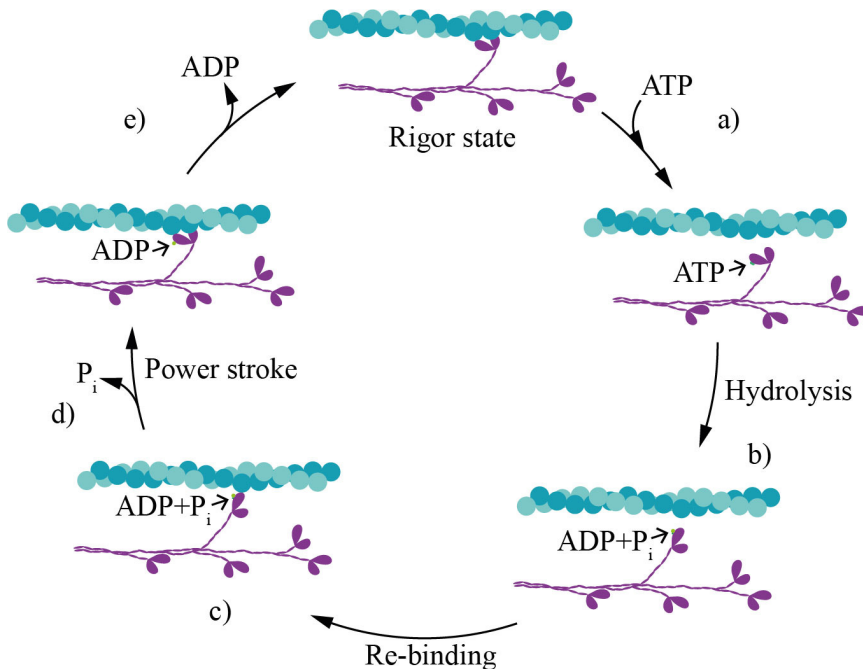


**Figure 2.3.** Schematic illustration of the cross-bridge cycle. a) The binding of ATP to myosin causes a weaker interaction between actin and myosin. b) The ATP molecule is hydrolysed into ADP and inorganic phosphate (P<sub>i</sub>), which causes a conformational change in the myosin, forcing the motor domain and its lever arm into a cocked position. c) The myosin head re-binds to the actin filament causing d) dissociation of inorganic phosphate from the catalytic site followed by a power-stroke, pulling on the actin filament, and e) ADP dissociates. As a new ATP molecule binds in the cycle is repeated. Figure freely interpreted from<sup>61</sup>.

### 2.1.2 The microtubule-kinesin system

Microtubules consist of tubulin protofilaments arranged in a 3-start helical structure running parallel to the axis of the filament<sup>75</sup>. This creates stiff, hollow tubes with a diameter of 25 nm<sup>11</sup> with a several millimetre long persistence length in solution<sup>11,37</sup>. If transported along kinesin motor tracks, microtubules have a shorter persistence length around 100 μm<sup>76</sup> (albeit, this depends on the filament length). Similar to actin, microtubules have a plus and a minus end due to the asymmetry of the dimers.

Kinesin 1 is a motor protein highly involved in cargo transport within the cell<sup>77</sup>. Like myosin, kinesin has two heads containing the binding sites for microtubules<sup>78</sup>. The binding mechanism is similar to that of the actomyosin system<sup>60,72</sup> involving varying binding affinities coupled to different states in the ATP turnover cycle<sup>38</sup>. Unlike myosin-II, kinesin 1 is a processive motor<sup>11,38</sup> which means that at least one of the heads is bound to the microtubule at all times. Related to this processivity, kinesin-1 propels microtubules at a slow rate (1 μm/s). The step size is around 8 nm<sup>1</sup>.

Due to the longer persistence length of microtubules<sup>42</sup> as compared to actin filaments<sup>25</sup> wider channels, up to 19  $\mu\text{m}$  wide<sup>79</sup>, can be used in nanotechnology devices. However, any interaction of microtubules with the side-walls causes a re-direction of their pathway, both along and up the wall, which may lead to detachment<sup>25</sup>. Wider channels enable microtubules to approach the wall at larger angles, increasing the risk of detachment. Therefore, they are better guided in narrower tracks below 1  $\mu\text{m}$ <sup>25</sup>.

For the microtubule-kinesin system we use a combination of  $\text{SiO}_2$  channel walls and Au channel floors in our devices. The motility on the  $\text{SiO}_2$  can be suppressed by preventing kinesin binding through polyethylene glycol (PEG) treatment<sup>80</sup> and a high density of kinesin motors can be bound to Au to promote motility<sup>81</sup>. Thus, the combination of PEGylated  $\text{SiO}_2$  walls and Au floors provides a high contrast in motility on the floors as compared to the walls<sup>81</sup>.

## 2.2 Patterning techniques for molecular motor devices

The physical confinement of the molecular motor systems is done by nanoscale channels. For the actin-myosin II system the confining channels are made directly in polymer resist, whereas for the microtubule-kinesin I system, these channels are defined in polymer resist and subsequently etched down into  $\text{SiO}_2$ . The following section gives a brief introduction to the two lithography methods used in this thesis for defining the channel structures: electron beam lithography and nanoimprint lithography.

### 2.2.1 Electron beam lithography

Electron beam lithography (EBL) uses high-energy electrons to pattern a polymer resist, which enables patterning with a high resolution (sub 10 nm)<sup>82,83</sup>, using commercially available tools and materials. Unlike the most common forms of ultra violet lithography (UVL), EBL does not require the use of a mask for selective exposure. Instead, the structures are patterned by selective exposure in an adjustable pattern by an electron beam scanning across the surface (**Figure 1.4a**). Therefore, EBL is a very adaptable method well suited for research.

To create the electron beam, primary electrons are extracted from an electron source and accelerated towards the specimen with an energy corresponding to the acceleration voltage. The electron beam is focused by electromagnetic and/or electrostatic lenses as it travels towards the specimen. It travels through the electron column (all kept in high vacuum), creating a very small, few nanometres wide<sup>84</sup>,

focused electron probe. When the primary electrons reach the sample, they begin interacting with the resist.

There are two classes of resists, negative tone and positive tone resists<sup>85</sup>. Positive tone resists have long polymer chains that are cleaved upon electron beam exposure, making the exposed areas more soluble. Negative tone resists consist of shorter polymer chains that are cross-linked upon exposure, making these areas less soluble. Obviously, there are a range of different polymer chain lengths and compositions, affecting both the contrast and sensitivity for each resist while also making them more or less soluble in different types of developers.

There are different types of electron-matter interaction depending on the electron energy. Low-energy electrons can scatter both elastically and inelastically<sup>86</sup>. Elastic scattering will cause the primary electrons to slightly deflect, causing beam broadening. Inelastic scattering will generate (shorter-range) secondary electrons in the resist, which in turn may lead to proximity exposures. Higher energy electrons penetrate the sample deeper, all the way into the substrate. Here, they can backscatter and re-enter the resist layer, causing a larger proximity exposure, which can overexpose or even distort the pattern. If the acceleration voltage is increased, the number of inelastic scattering events in the resist will decrease as the electron energy increases, and less beam broadening will occur<sup>86</sup>. However, this increased substrate interaction will cause a longer-range proximity effect than at lower voltages. As the electron energy is increased, the sensitivity of the resist is decreased, i.e., the number of chain scissions or cross-links per electron will decrease, and higher exposure doses are required, due to that it is mostly scattered, low-energy electrons that interact with the resist. In turn, the exposure dose strongly affects the pattern quality, as a too low electron dose leads to underexposure, and the structure will not be fully patterned. A too high electron dose will cause an overexposure, resulting in broadening of the pattern, as well as possible feature collapses in very dense patterns. It is therefore, very important to choose the correct resist and developer for each purpose, as well as the appropriate hardware parameters. The overall pattern resolution will depend on the probe size, the type of resist and developer used, the type of electron scattering occurring as well as the range of any secondary electrons generated<sup>85</sup>.

Albeit the high flexibility of use, EBL also has several drawbacks. A drawback related to beam scanning is the long exposure time needed as compared to the flood-like exposure during projection UVL. Furthermore, depending on the exposure parameters and the resist material used, scattered electrons can be an issue by causing proximity effects<sup>85</sup>. Also, electrostatic charging may occur in non-conductive materials, causing defocusing of the electron beam (due to Coulomb interactions), which decreases the resolution<sup>85</sup>.

## 2.2.2 Nanoimprint lithography

Nanoimprint lithography (NIL) is a high-throughput technique suitable for large-scale fabrication while providing sub-10 nm resolution<sup>87,88</sup>. There are two main types of NIL, UV-NIL<sup>89</sup> and thermal NIL (T-NIL)<sup>88</sup>. In both instances, a polymer resist is heated above its glass transition temperature and a stamp is uniformly pressed down into the resist at a high pressure, transferring the stamp pattern into the polymer, by physically displacing the polymer and filling the stamp protrusions (**Figure 1.4b**). In T-NIL the polymer resist is cured by cooling, whereas in UV-NIL the polymer resist is cured using UV-light. Therefore, mainly negative tone resists are used for NIL. The mother-stamp for T-NIL is made out of a hard material, e.g., a metal or SiO<sub>2</sub> on Si<sup>90</sup>. However, the resist in UV-NIL needs to be flooded with UV-light to initiate the catalytic cross-linking reaction to cure the resist<sup>89</sup>. This means that the stamp or substrate needs to be transparent. In this thesis a hard mother-stamp is used to create a transparent intermediate polymer stamp (IPS<sup>®</sup>) by T-NIL. The IPS<sup>®</sup> is then used to imprint a UV-curable resist with UV-NIL. Usually, the stamp is not pushed into contact all the way down to the substrate, but a thin residual layer of resist is left to protect the structures. This residual layer can be removed by oxygen-plasma treatment. A schematic illustration of a NIL process is seen in **Figure 2.4**.

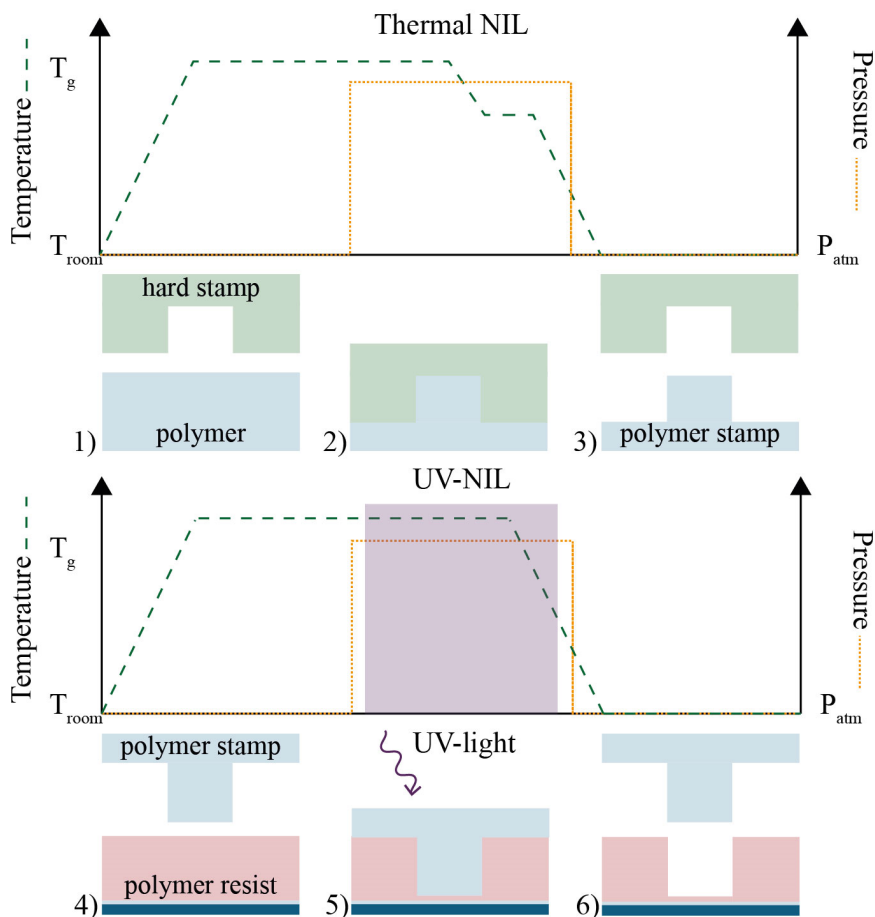


**Figure 2.4.** Schematic illustration of a NIL processes. In thermal imprinting 1) the polymer is heated above its glass transition temperature,  $T_g$ , and 2) imprinted with a hard stamp at an elevated pressure. The polymer is cured by cooling at the elevated pressure. The pressure is then decreased to atmospheric pressure and 3) the stamp is released. In UV-NIL 4) the resist is heated above  $T_g$  and 5) imprinted at an elevated pressure. The resist is cured by UV-light exposure before 6) releasing the stamp. Figure designed based on the process used in our imprinting tool.

## 2.3 Solving combinatorial problems

Many important mathematical problems are of combinatorial nature: the correct solution(s) consist of a combination of input objects. These problems are important in for instance, developing artificial intelligence<sup>52,53</sup>, optimal network routing<sup>56</sup>, game theory<sup>91</sup>, protein folding<sup>54</sup> and cryptography<sup>92</sup>.

A specific subarea of combinatorial problems is the non-deterministic polynomial time (NP) problems. These are problems with multiple solutions that cannot be

verified within a polynomial timeframe<sup>2</sup> as the number of input objects,  $n$ , increase, such as the Travelling Salesman problem Sarah encountered in the introduction. Polynomial time-complexities can be described as  $n^2$ , whereas many combinatorial problems that must be solved by brute force, such as the SSP, are described by an exponential time-complexity,  $2^n$ . Sequentially solving these problems quickly becomes intractable as a function of  $n$  due to the exponential scaling, and instead, parallel computation techniques are required. However, if different NP-problems can be reduced to other NP-problems by algorithms that scale polynomially<sup>93–95</sup>, they are considered complete, i.e., “NP-complete”. Thus, solving one NP-complete problem, offers in principle, a way to solve all problems in this class.

Apart from high-power consuming multi-core processing with electronic parallel computers<sup>3,4</sup>, there are several other alternative parallel computation techniques currently being explored. A few instances of these are: microfluidics based computation<sup>8</sup>, DNA computation<sup>5–7</sup> and quantum computation<sup>9</sup>, described briefly in the section below.

### 2.3.1 Alternative parallel computation techniques

Microfluidics based computation<sup>8</sup> is an NBC technique, in which liquids with fluorescent beads are pushed through channels to explore all possible paths encoding a mathematical problem<sup>8</sup>. External pressures are required<sup>96</sup> to maintain flow along the channels, and the pressure requirements increase impractically as a function of  $n$ . In addition, the architecture becomes intractably complex for larger instances, which prevents the technique from scaling well.

DNA (deoxyribonucleic acid) computation<sup>5–7</sup> uses large amounts of nucleotide (adenosine, thymidine, cytosine and guanidine) combinations, i.e., single stranded DNA, as computing agents. The solutions to the problem are encoded as unique nucleotide sequences and the agents compute by selectively combining with their complementary strands, creating double stranded DNA. This enables all excess single stranded DNA agents with the “wrong” sequence to be discarded. If the paired sequences are immobilized on the surface<sup>7</sup>, the doubled stranded DNA can be extracted and further sorted, so that only the correct solution(s) remain (if there is a correct solution). Another method<sup>97</sup> is to generate an output signal in the form of a single DNA strand with a specific sequence upon activation by DNA agents (complementary DNA strands). The DNA agents combine with partially doubled stranded DNA and then release the originally bound strand after branch migration has occurred, generating the output signal. Despite its versatility, high energy efficiency<sup>5</sup> and parallelism, the major drawback with DNA computation is the quite large error-rate<sup>98</sup>. As a consequence of this, impractical amounts of DNA<sup>7,99</sup> are required to ensure statistically significant results for large problems.

The basis of quantum computation is to process coherent quantum mechanical waves using “qubits”, which are quantum systems with two states that can be superpositioned<sup>9</sup>. Furthermore, in the world of quantum mechanics, the qubits can also be entangled providing even more states which makes this technique massively parallel. However, quantum computation is currently underdeveloped, though a huge effort is ongoing to develop new qubit systems and optimizing computational designs to limit decoherence-causing destructive noise.

### 2.3.2 Computing with molecular motors

All parallel computation methods mentioned in the previous section suffer from drawbacks, and are currently not able to solve large instances of NP-complete problems. We have chosen to explore the possibility of using molecular motors as computing agents in nanoscaled NBC systems, i.e., where the mathematical problem is graphically encoded into a network of channels and junctions (see example in **Figure 1.2**). Each pathway in the network corresponds to a different solution, which means that a large number of proteins can be used to compute problems in a massively parallel manner. Since the agents are self-propelled, no external forces (e.g., pressure difference or electricity) are needed.

A major benefit of computing with molecular motors is the low energy requirement. The self-propelling mechanical work, is fuelled by the chemical energy molecule ATP in a highly energy-efficient<sup>1</sup> manner, as mentioned in section 2.1. For comparison, the Landauer limit, stating the minimal energy cost due to heat generation for any computational system, and is defined as  $kT \ln 2 \approx 2.9 \cdot 10^{-22}$  J per binary operation<sup>100</sup>. The energy cost in molecular motor-powered computational systems can be defined as the amount of energy required to perform one computational operation, such as moving a cytoskeletal filament past one split-junction point to another. This in turn, is determined by the step size and energy cost per step which depends on the number of heads binding to each filament, as each unbinding event requires 1 ATP molecule (corresponding to  $25kT \approx 100 \cdot 10^{-21}$  J). The energy consumption per operation for a molecular motor-based NBC computer<sup>1</sup>, encoding the SSP (see example in **Figure 1.2**) of the 30 first prime numbers, is on average  $\sim 2 \cdot 10^{-14}$  J for both myosin II and kinesin 1 propelled filaments, i.e., the energy required to travel between two split junctions. This is much lower than for an electronic super computer which requires approximately  $2.3 - 5.3 \cdot 10^{-10}$  J per binary operation (see more detailed calculations in Nicolau et al.<sup>1</sup> supporting information S7), several orders of magnitude more than molecular motors. This makes molecular motor-based computation a very viable and worthwhile parallel computation technique, promising also for larger instances of NP-complete problems.

# 3 Surface treatment

*The material chemistry of molecular motor devices must be compatible with the sensitive biological systems used to ensure selective motility and protein binding. This chapter describes how we have optimized the chemical surface treatment of the channel floors (Paper I) and developed a method for cleaning and re-using our nanodevices (Paper IV). We also describe the initial results of a new device system using two different polymers as both channel walls and floors.*

## 3.1 Motivation and previous work

To enable selective motility in biomolecular devices (**Figure 1.3**), the surface chemistry of the channel floors must differ from that of the channel walls. This is achieved here, by using different materials for the floor as compared to the walls, where the motility on the walls is suppressed and the motility on the floors is promoted.

Both the surface charge<sup>39</sup> and surface hydrophobicity<sup>40–42</sup> affect the binding mechanism of HMM to a surface. As mentioned in Chapter 2, the HMM tail has an excess negative charge, whereas its two heads have an excess positive charge. Earlier studies<sup>101–103</sup> have shown motility on positively charged surfaces, suggesting that electrostatic forces promote the adsorption of the negatively charged HMM tail<sup>104,105</sup>. Further studies on the actin-myosin system<sup>29,39,42,43</sup>, indicate that more hydrophobic surfaces tend to promote actin motility due to HMM configurations with the heads extending out into solution<sup>39</sup>. This entropically driven adsorption<sup>40</sup> is believed to be related to partial unfolding<sup>41</sup> of the HMM tail, at the point where it was been cleaved off from light meromyosin by chymotrypsin.

There are several methods to change the surface hydrophobicity, e.g., by oxygen plasma treatment or through surface functionalization with different silanes<sup>43,102,106</sup>. Previous studies<sup>39,43</sup> have shown that trimethylchlorosilane (TMCS) functionalised surfaces promote high quality actin filament motility. The SiO<sub>2</sub> channel floors in the actin-myosin devices form silanols (SiOH) that are easily derivatized with e.g., TMCS. TMCS reacts with surface silanols and forms a monolayer of hydrophobic methyl groups through a chemical vapour deposition (CVD) process (**Figure 3.1**).

To introduce more hydroxyl groups, the SiO<sub>2</sub> surface can be activated with oxygen plasma. This oxygen plasma treatment also oxidizes the surrounding polymer walls used in our devices, making them more hydrophilic, allowing motility to be suppressed.

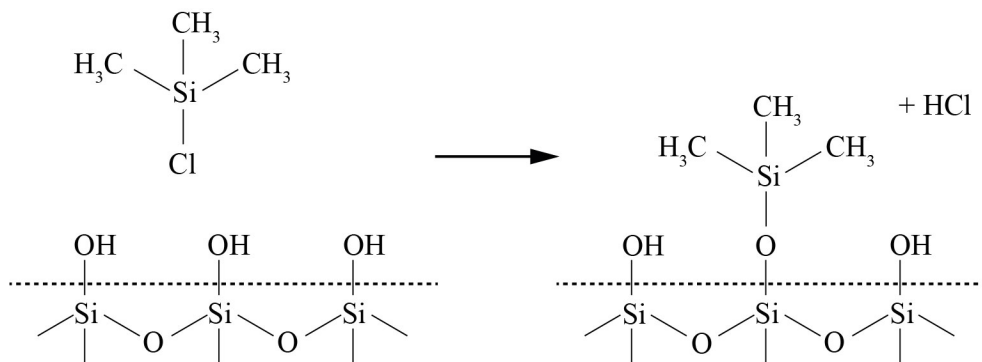


**Figure 3.1.** Schematic illustration of the trimethylchlorosilane (TMCS) reaction with hydroxyl groups on a SiO<sub>2</sub> surface. The chlorine group in TMCS reacts with hydroxyl groups on SiO<sub>2</sub> forming a monolayer of methyl groups (hydrophobic moieties).

In previous TMCS studies<sup>39,43</sup>, the CVD process occurred in a fully saturated TMCS system. Initially, we used a similar process but noticed inconsistencies in sample behaviour, with respect to both the measured static water contact angles and the actin filament sliding velocities for different sample batches. We linked these observations to the primitive nature of the used CVD process, performed in an uncontrolled environment in a glass jar or petri dish, in a glove-box used by multiple users for a large variety of different chemical procedures.

To provide more reliable results, with a consistent device performance in terms of motility on the SiO<sub>2</sub> channel floors, we developed a CVD tool to enable silanisation in a more controlled manner (Paper I), described in more detail in section 3.2 below. We found that the surface hydrophobicity could be tailored by varying the TMCS partial pressure and silanisation duration.

Hitherto, mainly poly(methyl metacrylate) (PMMA) has been used, both for EBL<sup>1,21</sup> and NIL<sup>45</sup> for actin-myosin II devices. Previous actin-myosin motility studies on different polymers<sup>20,29,30,107</sup> was published over a decade ago, and new and improved materials are constantly being developed. Therefore, we studied two new and improved polymer resists, CSAR62 and TU7, for channel wall structures patterned by EBL and NIL, respectively. We found that motility could be suppressed by oxygen plasma treatment, making both polymers a suitable material choice for channel walls. Moreover, no autofluorescence was observed during IVMA with rhodamine-phalloidin labelled actin filaments and both polymers supported motility when left un-treated by oxygen plasma, indicating a lack of protein-toxicity. We also

developed a new device system using a combination of the two polymers as channel floors and channel walls, completely removing the requirement of modifying the SiO<sub>2</sub> surface by silanisation. Albeit observing motility, the filament velocity was still lower on these surfaces as compared to that than on TMCS-derivatised SiO<sub>2</sub> and will need further development before being a viable contender. These studies are further described in section 3.3.

The re-use of nanostructured devices within molecular motor-based applications is highly desirable due to the expensive and time-consuming fabrication procedures, as well as from a sustainability perspective as less material is used and samples shipped elsewhere can be recycled for multiple experiments. Therefore, we developed a process for chemically cleaning the nanostructures from old proteins without disassembling the nanofluidic flow cells (Paper IV, section 3.4).

## 3.2 Controlled surface modification (Paper I)

**Figure 3.2** shows a 3D-render of our home-built CVD set-up for silanisation. The silanisation chamber is pumped down to vacuum pressure ( $10^{-2}$  bar) to reduce the amount of contamination and oxygen levels. The valve system enables nitrogen purging to clean the surfaces and the chamber, before and after silanisation. Since the TMCS is never exposed outside the system, the shelf-time of the silane can be expected to be prolonged and the tool can be located in a fume hood instead of inside a glove box. Furthermore, the valve system enables silanisation at various partial pressures of TMCS.

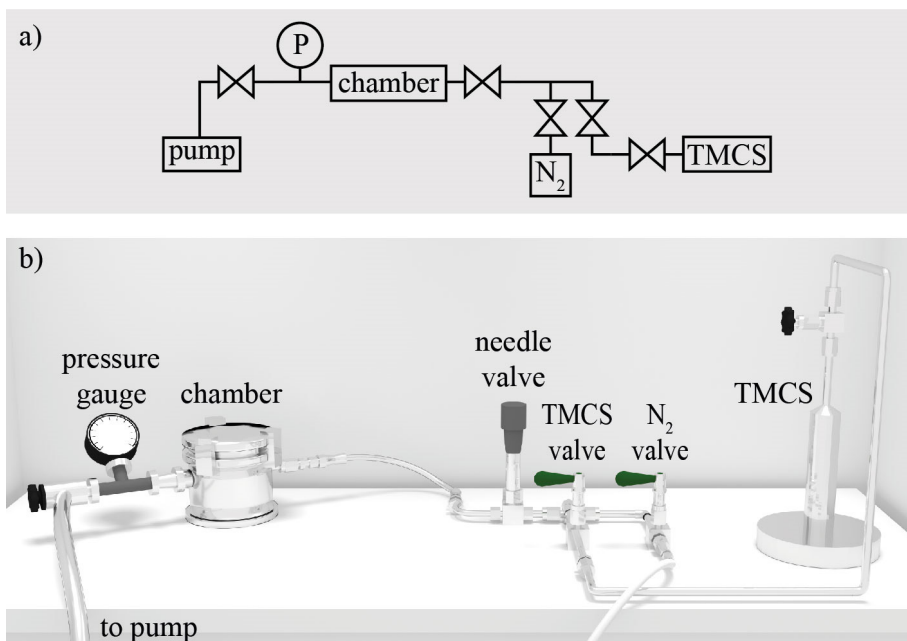


**Figure 3.2.** a) Schematic diagram and b) 3D-render of the chemical vapour deposition tool built for silanisation. The silanisation chamber is pumped down to vacuum pressure and flushed with N<sub>2</sub> in repeated cycles to limit the amount of contamination. The partial pressure of TMCS in the chamber is controlled by valves.

Earlier studies<sup>23,42,108</sup> show an increase in the actin filament sliding velocity with an increasing water contact angle, up to  $\sim 80^\circ$ . At higher contact angles, the HMM proteins are likely to denature, causing a reduction in motility. Also other factors may affect the sliding velocity, including surface roughness<sup>43,109</sup>, due to friction or non-uniform coverage with HMM. All previous studies of motility variations vs contact angle have been done using a range of different surface materials. **Figure 3.3** shows how we were able to tailor the surface hydrophobicity using only one type of silane (TMCS) by varying the silanisation time and partial pressure of TMCS.

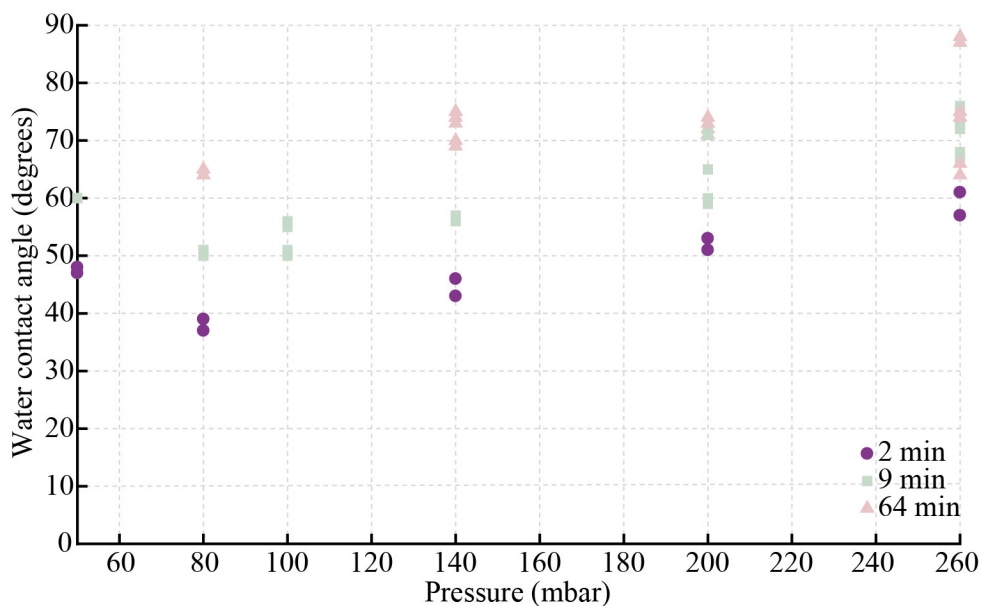


**Figure 3.3.** Water contact angle as a function of chamber pressure at different silanisation times. The chamber pressure is pumped down to  $10^{-2}$  mbar and increased by flowing in TMCS. The silanisation time is defined as the time after reaching the respective chamber pressure. The water contact angle increases with an increased chamber pressure and increased silanisation duration.

The measured water contact angle increased with the silanisation duration and chamber pressure, indicating a higher surface coverage of TMCS. The highest chamber pressure we could obtain was 260 mbar, which corresponds to a fully saturated TMCS system at room temperature. To study the actin filament sliding velocity at different degrees of TMCS coverage, we used two types of protein assay solutions, amc130 (ionic strength 130 mM with methylcellulose) and a60 (ionic strength 60 mM). The higher ionic strength in the amc130 solution promotes fewer, but longer actin filaments as the interaction strength between actin monomers is stronger. Furthermore, the amc130 solution contains methylcellulose which prevents actin filaments from diffusing away from the surface even if they are not tethered by HMM. **Figure 3.4** shows the obtained sliding velocities in both assay solutions for different water contact angles. At the lowest contact angles ( $10^\circ$  and  $28^\circ$ ), only the methylcellulose-containing amc130 solution showed motile actin filaments, albeit at reduced velocity. At these low contact angles on negatively charged  $\text{SiO}_2$ , the majority of the HMM molecules are expected to bind via their motor domains and not via their tail segment<sup>23,42,103,105</sup>, causing a decrease in the number of motility-promoting HMM molecules. The sliding velocities increasing with an increased contact angle is consistent with previous ideas<sup>23,105</sup>, suggesting that the fraction of HMM molecules bound via their tail domain increases with larger contact angles. However, despite the observed higher velocity of actin

filaments at higher contact angles, also the variability within the samples was larger. At  $86^\circ$  we could observe areas with little to no motility. Overall, the total number of motile filaments was also very low on these samples, suggesting stochastic variations in the density of adsorbed functional HMM molecules in different regions.

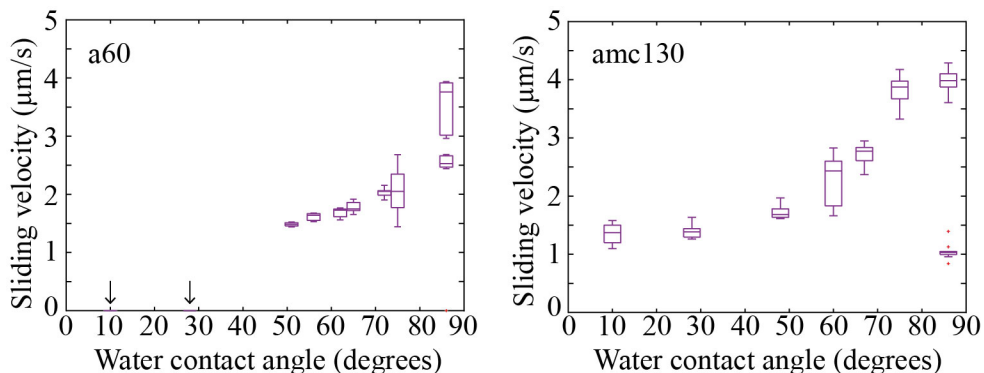


**Figure 3.4.** Actin filament sliding velocities at different water contact angles on TMCS-derivatised  $\text{SiO}_2$  surfaces using a60 and amc130 protein assay solutions. The sliding velocity increases with an increasing water contact angle. At the lowest contact angles in a60 no motility was observed (indicated by arrows). The motility experiments were performed at  $25.3 \pm 0.6^\circ\text{C}$  (a60) and  $24.8 \pm 0.9^\circ\text{C}$  (amc130). 10 filaments/contact angle were analysed. The central mark of the boxplot shows the median of the data set, the top edge of the box shows the 75<sup>th</sup> percentile and the lower edge of the box shows the 25<sup>th</sup> percentile. The whiskers show the most extreme data points not considered to be outliers, where an outlier is defined as a point greater than 1.5 times the interquartile range away from the top or bottom of the box (marked in red). Reprinted with permission from<sup>110</sup>. Copyright (2018) American Chemical Society.

### 3.3 Investigation of new polymer resists

The two main requirements for polymers to be able to be used for molecular motor-based nanotechnology devices are 1) the biocompatibility of the resist with the molecular motor system and 2) the ability to suppress motility to ensure selective motility only the nanostructured channels with TMCS. Furthermore, as the experiments utilise fluorescence microscopy, it is also important that the polymers are not autofluorescent.

Our standard devices are made with polymer walls and TMCS-derivatised  $\text{SiO}_2$  floors. Therefore, all test-devices also went through the necessary steps for processing nanostructured devices; baking, development, cross-linking etc. (details in Paper I). Post-processing, a few chips were exposed to oxygen plasma, and a subset of these were silanised with TMCS. We measured the static water contact angles of the differently treated samples (**Table 3.1**) and compared this to the actin filament velocity results obtained during IVMA experiments.

The oxygen plasma treated surfaces showed a large decrease in the contact angle as compared to the untreated chips. None of the surfaces were affected by the silanisation, indicating that the polymers are very suitable for selective HMM-binding onto the channel floors, and not to the polymer walls. This was confirmed by the results from the IVMA experiments, which showed no motility on the polymer surfaces that had been oxygen treated. Furthermore, we observed high-quality motility, with comparable actin-filament sliding velocities to that on TMCS derivatised SiO<sub>2</sub><sup>110</sup>, on both TU7 and CSAR62 (that had not been exposed to oxygen plasma). These results indicate that both resists are also biocompatible with our system.

**Table 3.1.** Water contact angle measurements on TU7, CSAR62 and SiO<sub>2</sub>.

	TU7 <sup>1</sup>	TU7 <sup>2</sup>	CSAR62 <sup>1</sup>	CSAR62 <sup>2</sup>	SiO <sub>2</sub> <sup>1</sup>
no TMCS	24±1°	65±1°	33±1°	71±1°	<5°
TMCS	26±1°	63±1°	35±1°	71±1°	67±1°

<sup>1</sup>Exposed to oxygen plasma at 5 mbar for 15 s.

<sup>2</sup>Not oxygen plasma treated

To further expand our device tool-box we made new devices with TU7 floors and CSAR62 walls. After spin-coating and baking the TU7, we cross-linked the polymer through a UVL flood exposure (365 nm, 20 s) and then spun a layer of CSAR62 on top. After a second bake, we patterned the top CSAR62 layer by EBL and performed an oxygen plasma treatment before developing the structures in O-xylene. By oxygen plasma treating the surface before development, we expected the top CSAR62 surface to be oxidized while the TU7 channel floors were protected by the undeveloped CSAR62. As a reference, we ran IVMAs on a non-plasma treated CSAR62 surface (showed motility) as well as a CSAR62 surface that had been oxygen plasma treated and then submerged in O-xylene (showed no motility), indicating our plasma treatment was unaffected by the development.

In the nanostructured surfaces with CSAR62 channel walls, we observed selective motility limited to the TU7 channel floors, however, at a reduced actin filament velocity and longevity. **Figure 3.5a** shows the summarised results of actin filament sliding velocities on TMCS derivatised SiO<sub>2</sub> reference surfaces for two temperatures (19°C and 26°C), on flat CSAR62 (also at two temperatures) and TU7 surfaces, and inside nanostructures made with CSAR62 walls with both TMCS derivatised SiO<sub>2</sub> channel floors as well as TU7 channel floors. As could be expected, the velocities are much higher in the higher temperature region. A noticeable difference between the two different types of nanostructured surfaces (CSAR62-TU7 and CSAR62-TMCS) is the much lower velocity on the TU7 floors as compared to the TMCS floors. **Figure 3.5b** shows atomic force micrographs of flat CSAR62, flat TU7 and the nanostructured CSAR62/TU7. The measured root mean square roughness was

similar for both TU7 and CSAR62 ( $0.47 \pm 0.05$  nm and  $0.41 \pm 0.02$ ), but both higher and more uneven for the TU7 channel floors ( $1.90 \pm 0.78$  nm) which likely contain a lot of resist residue due to lack of oxygen treatment after EBL exposure and development. These results are consistent with the idea that rougher surfaces might cause a decrease in the sliding velocity due to friction<sup>43,109</sup>. Further processing optimisations and nanostructuring in these polymer resists are discussed in section 4.4 (Paper III) and 4.5 (paper III).

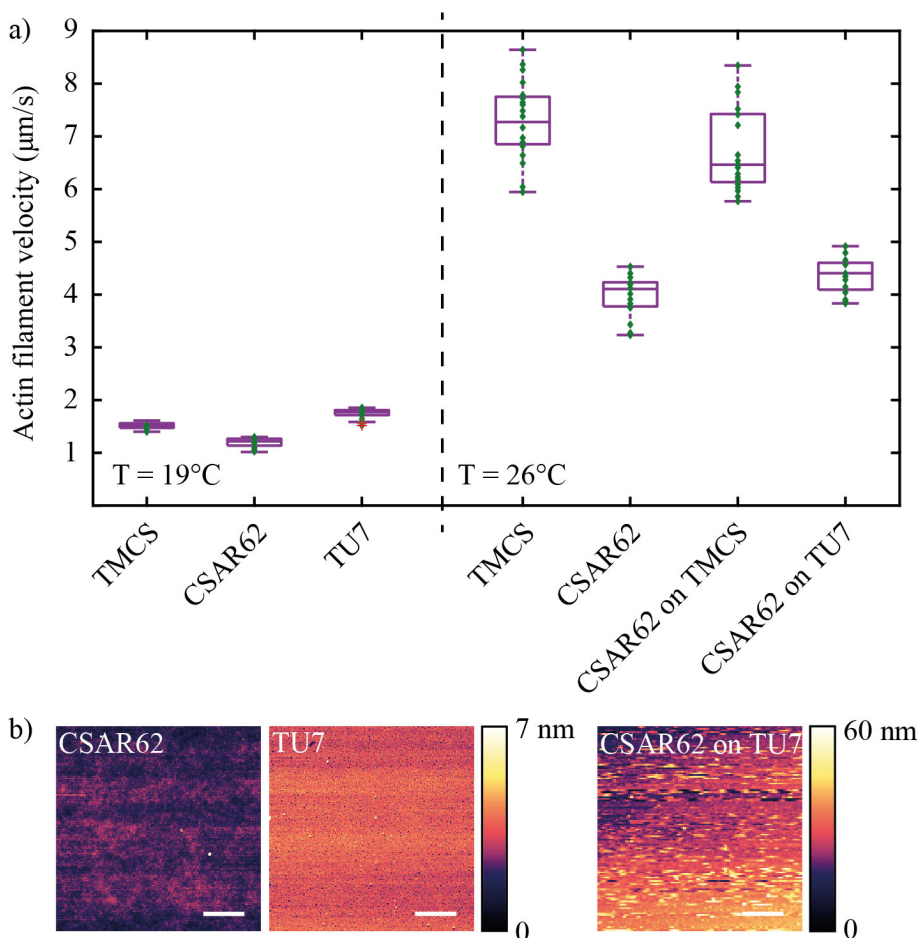


**Figure 3.5.** a) Actin filament sliding velocities on flat TMCS derivatised SiO<sub>2</sub> surfaces, on flat CSAR62 surfaces and flat TU7 without oxygen plasma exposure, and on nanostructured TMCS-derivatised SiO<sub>2</sub> and TU7 channel floors with CSAR62 walls. The motility experiments were performed at 19°C (left) and 26°C (right). 20 filaments/boxplot were analysed. The central mark of the boxplot shows the median of the data set, the top edge of the box shows the 75<sup>th</sup> percentile and the lower edge of the box shows the 25<sup>th</sup> percentile. The whiskers show the most extreme data points not considered to be outliers, where an outlier is defined as a point greater than 1.5 times the interquartile range away from the top or bottom of the box (marked in red). The green markers show all individual data points. b) Atomic force micrographs of flat CSAR62, flat TU7 and of the TU7 floor inside a larger structure in patterned CSAR62.

### 3.4 Surface regeneration (Paper IV)

During IVMA experiments, we have repeatedly observed how filaments tend to follow the sidewalls of nanostructures. To enable better studies of the effect of different chemical modifications of channel floors, independent of the influence of the walls, we developed some new structures which evenly distribute the filaments across a limited surface area. To try and re-direct the filaments away from the channel walls we introduced *bulges* or *petals*, creating flower-like structures. Before fabricating any real structures, we first ran Monte Carlo simulations (designs and analysis done by me, simulations done by Till Korten, see paper II for more details) to provide a prediction of the filament behaviour (**Figure 3.6**). These simulations were done for the microtubule-kinesin 1 system. In our initial designs we introduced a central pillar to try and increase the number of re-directing events further. However, according to the simulations, these pillars had no evident effect (compare A, B with C, D, E, F). The difference between A and B is a central circle squeezing the flower pattern to different extents, causing different angles at the petal intersections. Clearly, a smaller circle (and thus, higher angle) pushes the filaments more towards the centre. We varied the number of petals from 6 (A), 8 (G), 9 (H), 10 (I) to 12 (J) and found that more petals provide a more delocalised filament distribution. Thus, for the devices, we designed structures with different numbers of petals: 8 and 12, with different inner circle radii: 52, 54, 56, 58, 60  $\mu\text{m}$  and with varied petal radii between 10 and 15  $\mu\text{m}$ . **Figure 3.6K** and **Figure 3.6L** show the maximum projection of two fluorescence microscopy time-lapse movies of an actual device with microtubules evenly distributed across the surface.

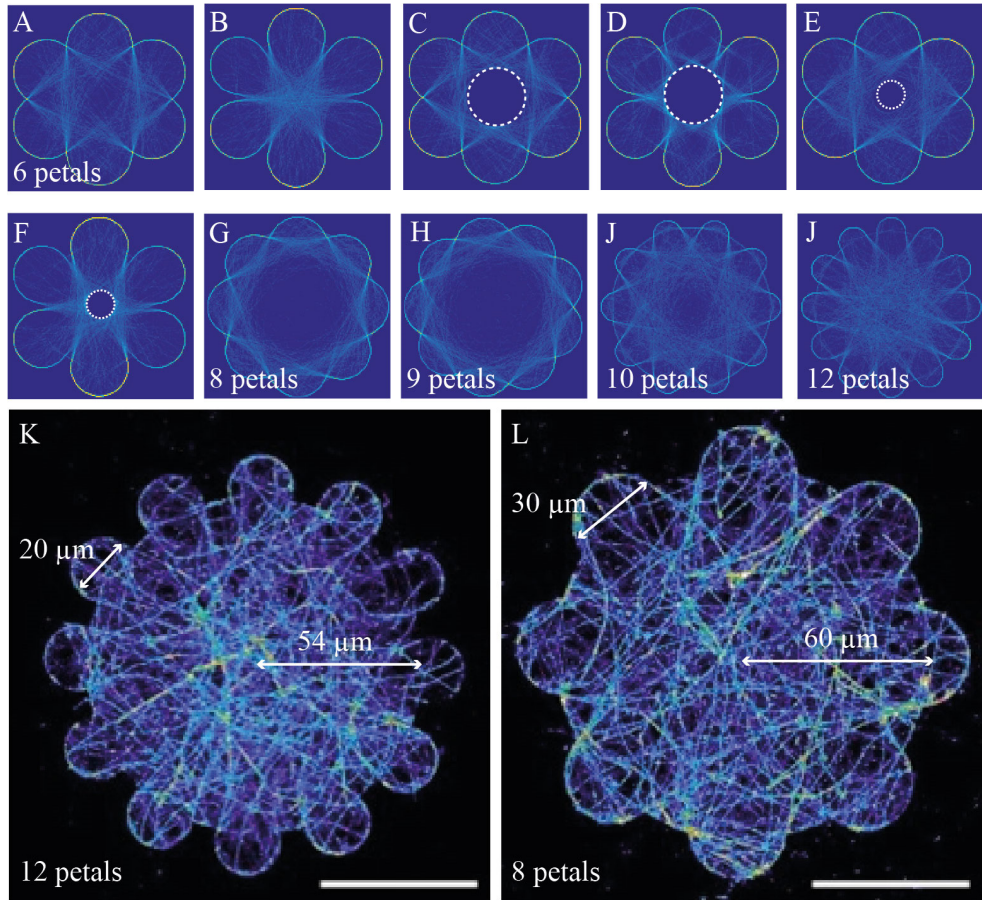


**Figure 3.6.** Heat maps from Monte Carlo simulations (A-J) and fluorescence micrographs (K-L) of microtubules in flower structures with varying properties regarding the number of petals, petal diameter and inner circle radius. Some structures also contain a central pillar (white dashed line). The scale bars in K and L are both 50 μm.

For our initial actin-myosin experiments, we used flat surfaces of TMCS-derivatised glass and SiO<sub>2</sub>, before moving on to large areas of un-patterned CSAR62 EBL resist, partially covering a TMCS-derivatised SiO<sub>2</sub> surface, and finally nanostructures with CSAR62 channel walls and TMCS-derivatised SiO<sub>2</sub> channel floors.

**Figure 3.7** schematically illustrates the developed protocol for surface regeneration involving the proteolytic enzyme proteinase K and the detergent Triton X100. Proteinase K is a non-selective, highly active protease that attacks the peptide bonds between several different amino acids<sup>111</sup>, and it has been used previously to cleave actin<sup>112</sup>. Therefore, we expected the proteinase K to appreciably lower the local protein concentration through proteolysis. Detergents weaken hydrophobic

interactions and are therefore, also likely to weaken the interaction between the HMM molecules and the surface.

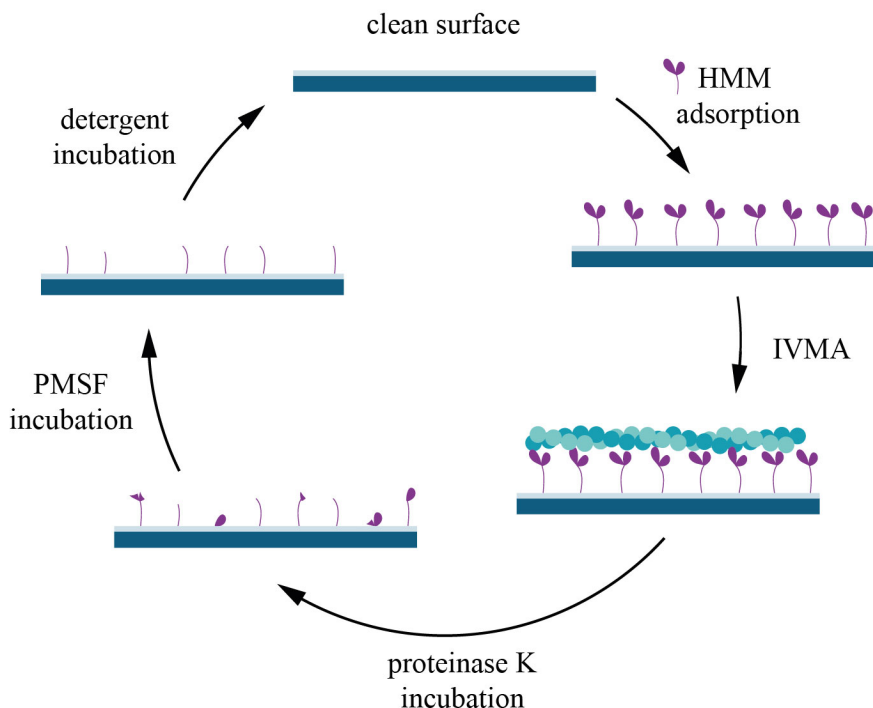


**Figure 3.7.** Schematic illustration of the surface regeneration process. HMM molecules are adsorbed onto a clean surface and an IVMA experiment is run. The sample is then incubated with the non-selective proteolytic enzyme proteinase K in order to cleave the HMM molecules into fragments. To inactivate proteinase K the sample is incubated with phenylmethane sulfonyl fluoride (PMSF) before finally cleaning the surface with the detergent Triton X100 to remove any remaining protein fragments.

**Figure 3.8** shows the regeneration results using different detergents and protocols. Our initial tests were done on TMCS derivatised glass surfaces and no detergent was used. However, we observed a decrease in the actin filament sliding velocity after regeneration, as well as an increased average filament length, while shorter filaments detached more rapidly. This led us to believe that the HMM density was lower on the regenerated surfaces, possibly due to steric hindrance to adsorption of fresh HMM by HMM remnants from the previous IVMA experiment. We were able to optimize this regeneration and obtain full surface recovery in terms of actin filament velocity by including an additional cleaning step with the detergent sodium dodecyl sulphate (SDS). This approach gave good motility quality even after multiple regeneration cycles. We then moved on to the partially covered CSAR62/TMCS-derivatised SiO<sub>2</sub> chips, with equally successful surface

regeneration of the TMCS-derivatised SiO<sub>2</sub> area without sacrificing the motility inhibition on the CSAR62 resist.

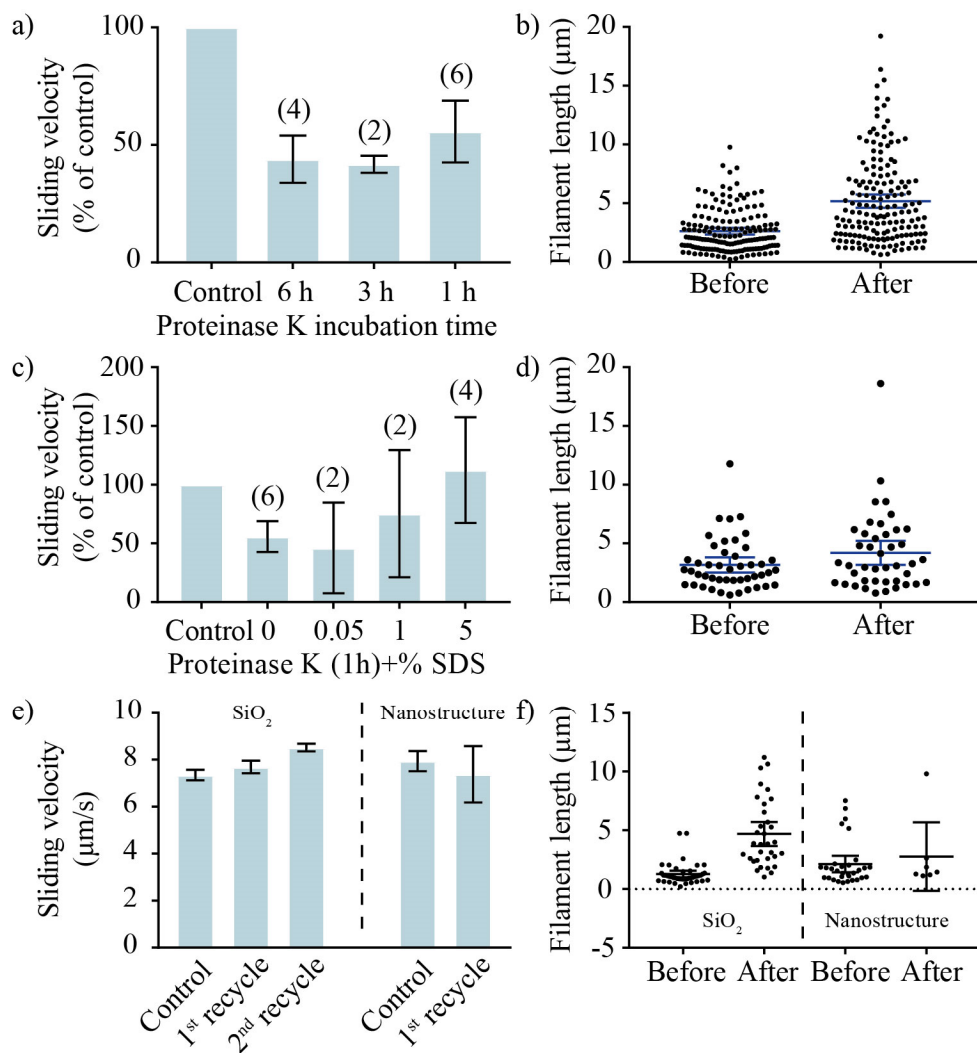


**Figure 3.8.** Actin filament velocity and length on TMCS-derivatised glass surfaces. a) For different incubation times with proteinase K, the number of surfaces are stated in parentheses (). Between 9-30 filaments were analysed for each experiment. b) Before and after regeneration with proteinase K (incubated 1 h) at 6 different experimental occasions. c) For 1 h proteinase K incubation followed by 5 min SDS treatment at 0, 0.05%, 1%, 5%, the number of surfaces are stated in parentheses (). Between 9-30 filaments were analysed for each experiment. The mean sliding velocities are normalised to the same surface before regeneration. d) Before and after regeneration with 1 h proteinase K incubation followed by 5 min 5% SDS treatment at 2 different experimental occasions. e) For 1 h proteinase K incubation followed by 5 min Triton X100 (0.05%) treatment on flat SiO<sub>2</sub> (1 surface, 18-25 filaments analysed) and in nanostructures (1 surface, 3-12 filaments analysed). f) Before and after regeneration with 1 h proteinase K incubation followed by 5 min Triton X100 (0.05%) treatment on flat SiO<sub>2</sub> and in nanostructures. All data are given as the mean ±95% confidence interval.

However, after the regeneration treatment of the nanostructures including CSAR62 channel walls and TMCS-derivatised SiO<sub>2</sub> channel floors, no motility could be observed. One possible basis for this decrease in performance could be interactions between the long hydrocarbon chains in SDS with the ester groups in CSAR62. Another reason could be the anionic nature of SDS, adversely affecting the performance of CSAR62, more prominent in the nanochannels than for larger surfaces. Therefore, we tested a new non-ionic detergent, Triton X100, which does not contain any long hydrocarbon chains. We were then able to obtain successfully regenerated surfaces with high-quality actin filament motility on both TMCS-derivatised glass and on nanostructured surfaces.

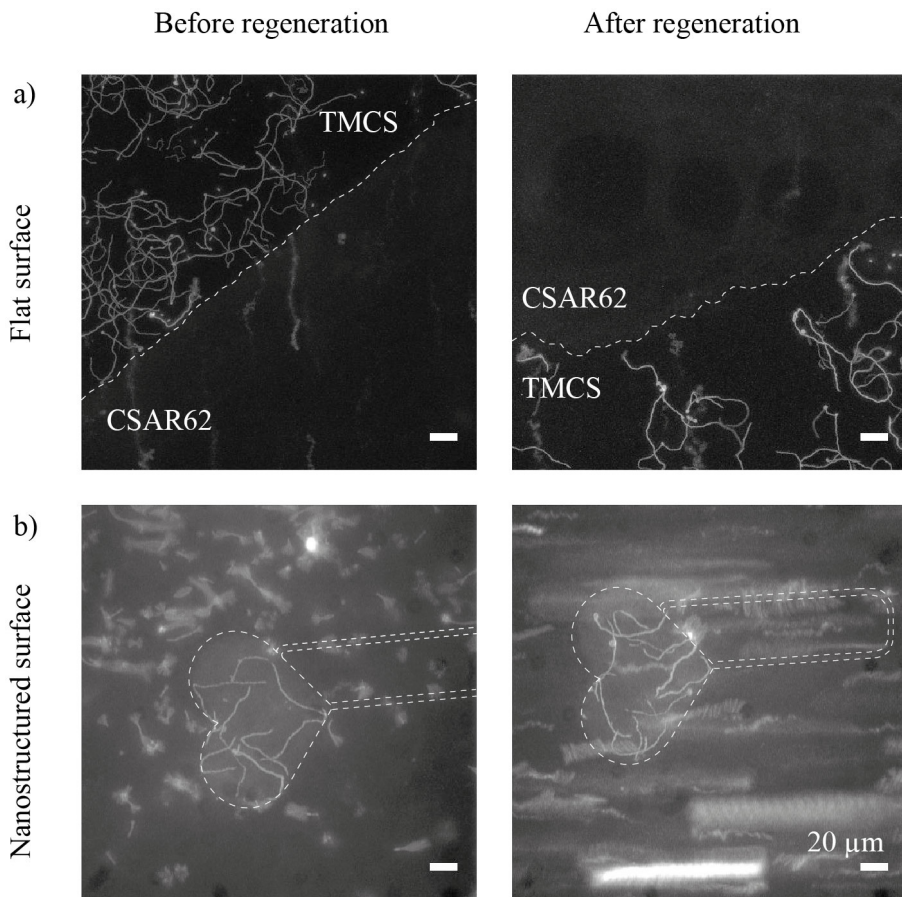


**Figure 3.9.** Maximum projections of fluorescence microscopy recordings (3.8 s) before and after regeneration of a) a partially covered CSAR62 and TMCS-derivatised SiO<sub>2</sub> using proteinase K and 5% SDS and b) nanostructures in CSAR62 with TMCS-derivatised SiO<sub>2</sub> floors using proteinase K and 0.05% Triton X100. The scalebar is 20 μm in all images. CSAR62 was spin-coated and then partially removed from the central region of the sample in a) and b) (both images are from the sample sample but at different locations).

### 3.5 Concluding remarks

By modifying the surface hydrophobicity in a controlled manner, we were able to tune the actin filament sliding velocity without changing the type of silane or material, which has greatly improved the yield of successful devices. We also demonstrated a novel method for fabricating nanodevices using the two polymer resists CSAR62 and TU7 as they both promote motility if they are left untreated, as well as inhibit motility if they are treated with oxygen plasma. Therefore, both resists serve well as channel walls inhibiting motility. However, channel floors made of motility-promoting (untreated) TU7 with motility-inhibiting (oxygen treated) CSAR62 walls need further optimization, likely by improving residual resist removal after EBL exposure. This may be done by further expanding the study to include different developers or chemical cleaning procedures. Moreover, we developed a technique for recycling molecular motor-based devices using the non-selective protease Proteinase K and surfactant Triton X100, creating a more sustainable fabrication process. These findings strengthen and expand the studies of chemically confining molecular motors in nanotechnology devices by including new materials and treatment protocols, the impact of which, is further discussed in the final chapter of this thesis.

# 4 Patterning nanostructures

*The scalable fabrication of our biocomputation devices require advanced nanofabrication techniques to provide nanometre-scale features, combined with a high throughput of larger scale samples for system development and experimental optimisation. This chapter describes the development of fabrication methods for patterning the channel walls for the actin-myosin II system by electron beam lithography and nanoimprint lithography.*

## 4.1 Motivation and previous work

The nanostructures used for physically confining molecular motor systems can be patterned by multiple techniques. The actin-myosin II system requires a high spatial resolution down to a few nanometres based on the necessary feature size (channel widths around 200-300 nm with details requiring sub 10 nm resolution, for junction details, see Chapter 2). Larger structures can be patterned by UVL, while the majority of the patterns need to be patterned by EBL. NIL can also be used to enable a higher fabrication throughput of larger devices, while still maintaining a high resolution.

The major drawbacks of UVL and NIL for our current experimental system is the requirement for a UVL mask for selectively exposing a photosensitive resist, and the necessity of a NIL stamp for imprinting features. This limits the flexibility in developing new structures within a reasonable time-frame, as new masks and stamps need to be fabricated for each new feature. However, when a suitable device design is defined, both these techniques can be used for large-scale fabrication in a feasible and sustainable manner. There are different UVL methods, the more commonly used tools use visible wavelengths providing a resolution  $\sim 50$  nm<sup>82</sup> due to diffraction limits, which makes this technique less suitable for actin-myosin devices. There are also more advanced methods like extreme UVL, pushing the resolution to sub 10 nm<sup>113,114</sup> by using very short wavelengths of light. However, for design development, EBL is still the preferred lithography method because of the flexibility, despite the longer exposure times required.

The device fabrication done by our group<sup>1</sup> prior to this thesis work, was relatively inexpensive and time-efficient due to the limited pattern size. However, the increased dimensions associated with an upscaled complexity, require optimisations for higher throughput fabrication (Paper III). We have therefore, optimised the EBL processing parameters and developed a process for fabricating devices by NIL.

To reduce EBL exposure times, we began with switching the EBL resist from PMMA to CSAR62, which has a higher sensitivity (allowing shorter exposure times). Similar to PMMA, CSAR62 is a methacrylate based polymer<sup>115</sup> but it has a higher contrast and resolution as compared to PMMA<sup>115,116</sup>. For PMMA, sub-10 nm<sup>117,118</sup> resolution is possible, but it requires higher electron doses for a given EBL system and developer. The exposure parameters for patterning actin-myosin II structures in CSAR62 are presented in Paper III and section 4.2.

NIL has previously been used for fabricating narrow channels (100-400 nm) for actin-myosin II devices in PMMA by Bunk et al.<sup>45</sup>. PMMA has a glass transition temperature around 95-106°C, and was in Bunk et al.<sup>45</sup> imprinted at 200°C. At temperatures above 100°C, thermal expansion can cause pattern deformations if the substrate and stamp are not thermally matched<sup>119</sup>. Here we use a new imprinting resist, TU7, developed by Obducat, with a lower glass transition temperature that can be imprinted at 75°C.

Furthermore, structures for molecular motors also require large open areas, loading zones (see **Figure 1.2**), to collect the filament agents from solution and funnel them towards the connecting channel network<sup>1,21</sup>. These loading zones are difficult to imprint by NIL, as areas with a large width relative to the height require the displacement of polymer across large distances<sup>46</sup>. We extended the previous study, to include a method of fabricating a new type of loading zone that was re-designed to contain nanoscaled pillars to provide close by regions into which the resist could be displaced (Paper II). By choosing the resist layer as thin as possible, we were able to optimise the stamp filling, allowing polymer to displace into the pillars. We managed to obtain motility inside the loading zones, albeit, at a lower velocity as compared to EBL patterned loading zones. Interestingly, after simulating the filament movement (simulations done by Till Korten, analysed by me) inside the new loading zones containing pillars, we found that the overall filament movement can be shifted to distribute the filaments evenly across the surface or towards one side. The developed imprinting process is described in Paper II and in section 4.3.

## 4.2 Process optimisation for EBL (Paper III)

**Figure 4.1** shows a dose test for exposing CSAR62 at 20 kV acceleration voltage. Previously, we were exposing PMMA950K at 20 kV with dose 250  $\mu\text{C}/\text{cm}^2$  and

developing in a 3:1 mixture of isopropanol and methyl isobutyl ketone mixture. By switching to CSAR62, we were able to reduce the exposure dose (using the same acceleration voltage, 20 kV) down to  $60 \mu\text{C}/\text{cm}^2$  when developed in O-xylene, which enables  $\sim 4$  times shorter exposures, while maintaining a high resolution.

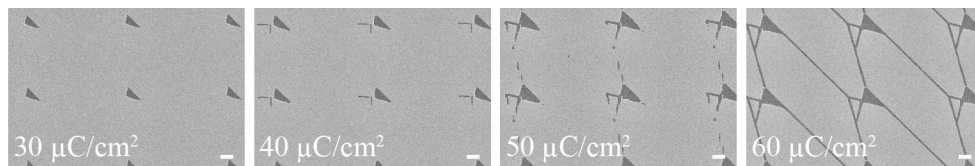


**Figure 4.1.** Scanning electron micrographs of CSAR62 exposed at 30, 40, 50 and 60  $\mu\text{C}/\text{cm}^2$  at 20 kV, and developed in O-xylene. The scalebar is  $1\mu\text{m}$  in all images.

To further decrease the exposure times, we tried increasing the aperture size in the electron column. This can however, cause a decrease in resolution due to a broader electron probe. Therefore, we performed IVMA experiments to examine if this possible decrease in resolution would affect the actin filament motility in our channels, most importantly if we would still observe unidirectional motion. **Figure 4.2** shows two fluorescence micrographs of patterns exposed with 10 and 20  $\mu\text{m}$  apertures. No noticeable loss in feature details and no U-turns were observed in the higher aperture structures, indicating we could expose our structures using a larger aperture, here 20  $\mu\text{m}$  instead of 10  $\mu\text{m}$ . This in turn increased our beam current from  $\sim 0.014 \text{ nA}$  to  $\sim 0.12 \text{ nA}$ , increasing our throughput by a factor of 8.5.

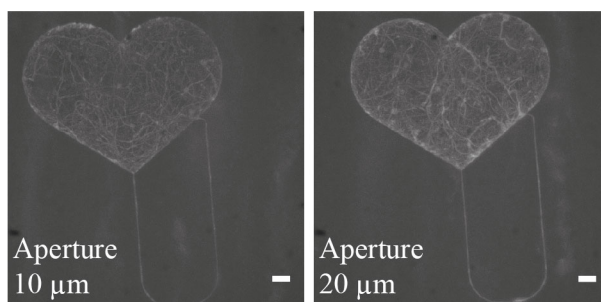


**Figure 4.2.** Fluorescence micrographs of patterns exposed with a 10  $\mu\text{m}$  aperture and 20  $\mu\text{m}$  aperture at 20 kV. The images show the maximum intensity for a 60 s time-lapse movie of an actin-myosin IVMA experiment. The scalebar is  $5 \mu\text{m}$  in both images.

A few years into this thesis work, our lab bought a new EBL system with a higher acceleration voltage, 50 kV, that, together with a 40  $\mu\text{m}$  aperture, provided beam currents of  $\sim 0.60 \text{ nA}$ . Thus, this would enable an even higher throughput due to faster exposure times. However, as mentioned in Chapter 2, higher acceleration voltages will decrease the number of forward-scattered primary electrons, and

higher electron doses will be required. Furthermore, the increased electron energy will cause the beam to penetrate deeper into the substrate, causing more backscattered and secondary electrons generating proximity exposures. To examine the pattern broadening at different doses, we performed a new dose test ranging from  $175 \mu\text{C}/\text{cm}^2$  to  $275 \mu\text{C}/\text{cm}^2$  in steps of  $25 \mu\text{C}/\text{cm}^2$ . We also switched the developer to amyl acetate which is supposed to provide an even higher contrast between exposed and unexposed CSAR62<sup>116</sup>. However, amyl acetate also leaves large amounts of residue on the channel floor as compared to O-xylene<sup>116</sup>, which is why O-xylene was used as a developer in the double resist (CSAR62/TU7) IVMA experiment described in section 3.3. As seen in **Figure 4.3**, we found that it was possible to achieve well defined features at  $250 \mu\text{C}/\text{cm}^2$  with an acceptable pattern broadening (40-50 nm).

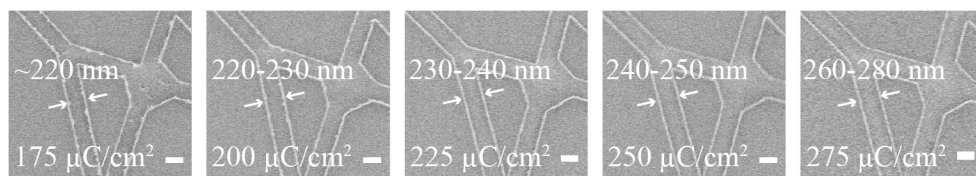


**Figure 4.3.** Scanning electron micrographs of CSAR62 exposed at 175, 200, 225, 250 and  $275 \mu\text{C}/\text{cm}^2$  at 50 kV developed in amyl acetate. The scalebar is 250 nm in all images.

### 4.3 NIL for molecular motor structures (Paper II)

**Figure 4.4** shows heat maps of Monte Carlo simulations (analysis done by me, simulations by Till Korten, TUD, see details in Paper II) estimating what effect a structural re-design of the loading zone with pillars would have on the actin filament behaviour. We found that the structural design and placement of the pillars can be used to tailor the emptying rate (**Figure 4.5**) from the loading zone as well as filament guidance. Designs A, B, F and G all have three sharp corners which seems to provide a larger difference in the emptying rate between the hexagonal and square placed pillar patterns as compared to designs D and E, which just have one sharp corner. Furthermore, the completely symmetrical pillar shapes in designs H and I are nearly identical, both compared to each other as well as between the hexagonal and square patterns. According to the heatmaps in **Figure 4.4**, the latter two (completely symmetrical) designs also seem to distribute the filaments more evenly inside the loading zone. The patterns with a sharp corner pointing towards the exit both have an overall higher emptying rate than their corresponding patterns rotated  $180^\circ$  (compare A vs B, D vs E and F vs G), as well as a higher emptying rate in the square pattern repetition as compared to the hexagonal repetition. The most noticeable effect in both **Figure 4.4** and **Figure 4.5** can be seen between patterns F

and G which have three sharp corners and a concave arc in the pattern causing the filaments to clearly shift towards one side of the loading zone. The reason for this is likely that the filaments hitting the concave wall are constantly re-directed according to their impinging angle<sup>25</sup>. This coincides well with the simulations and experimental results described in section 3.4. Similar simulations to these have also been successfully used for predicting the behaviour of the actin-myosin II and microtubule-kinesin 1 system in nanostructures<sup>1,120</sup>.

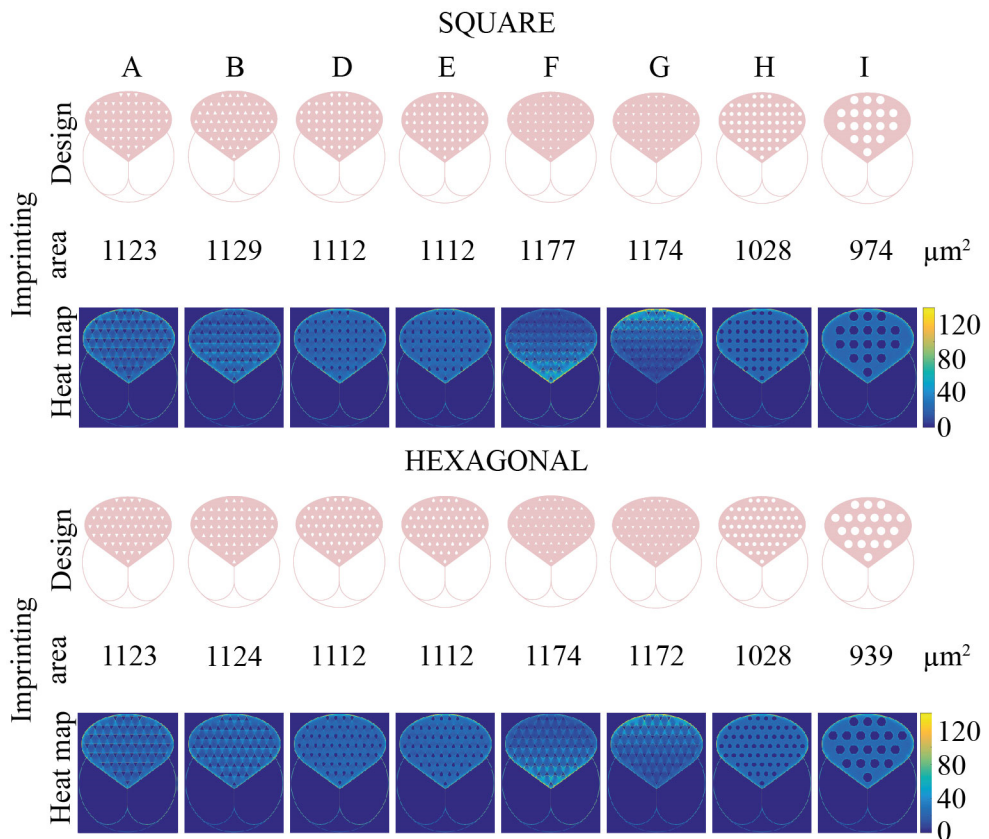


**Figure 4.4.** Loading zone designs for nanoimprint lithography. We created eight different pillar patterns placed in both a square and hexagonal pattern repetition. The heat maps show the filament distribution of 240 actin filaments (10  $\mu\text{m}$  persistence length) simulated for 1500 s, the colour bar corresponds to the number of filaments visiting each pixel. The imprinting area corresponds to the amount of open  $\text{SiO}_2$  available for HMM binding. Reprinted from<sup>121</sup>. Copyright (2019) IOPScience (gold open access).

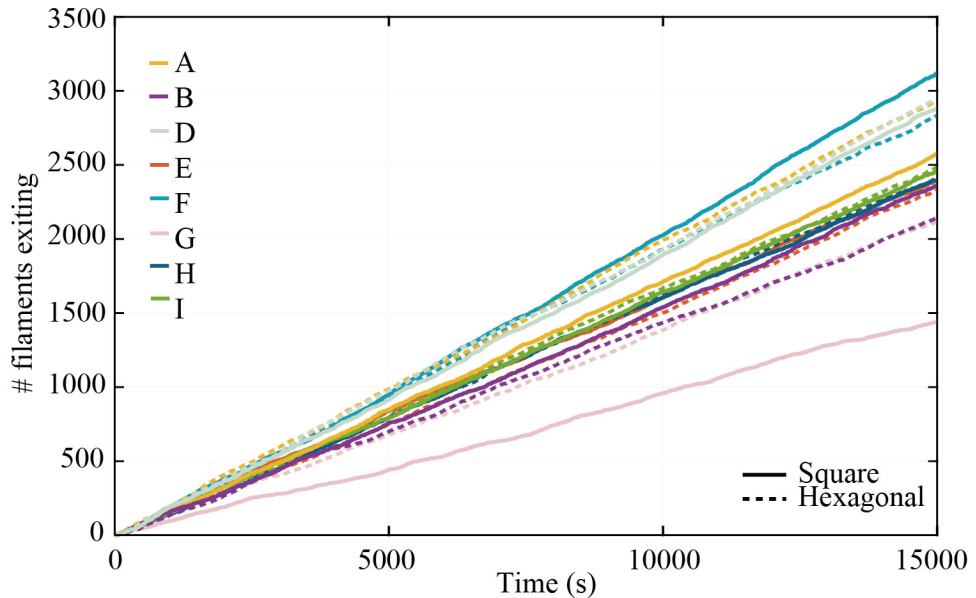


**Figure 4.5.** Emptying rate for the different loading zone designs shown as the number of filaments exiting as a function of time. The emptying rate varies depending on the pattern shape as well as the pattern repetition design (square or hexagonal). Reprinted from<sup>121</sup>. Copyright (2019) IOPScience (gold open access).

As mentioned, one of the difficulties for imprinting features with a large difference between height and width, is related to displacing large amounts of polymer. By including pillars into our design, we expected to provide regions into which polymer could be displaced. Furthermore, we aimed to limit the amount of displaced polymer by minimizing the resist layer thickness in order to obtain capillary flow upwards into the cavities, without suffering from insufficient filling during imprint. In standard NIL procedures, the resist layer is chosen thicker than the stamp protrusions to prevent damaging the stamp and deforming the pattern. However, by using a soft intermediate polymer stamp, IPS<sup>®</sup>, this risk is eliminated. To test this approach, we spin-coated TU7-220 at various spin-speeds ranging from 1000-3000 rpm. To imprint our structures, we fabricated a hard stamp in SiO<sub>2</sub> on a 4" Si wafer. A new IPS<sup>®</sup> for imprinting TU7 was made through thermal NIL for each wafer using the hard stamp. **Figure 4.6** shows the resulting TU7-220 thickness for different spin-speeds and scanning electron micrographs of the structures. Only the thickest TU7-220 layer used (~350 nm, still thinner than the 380 nm stamp cavities) provided sufficient filling of the stamp protrusions.

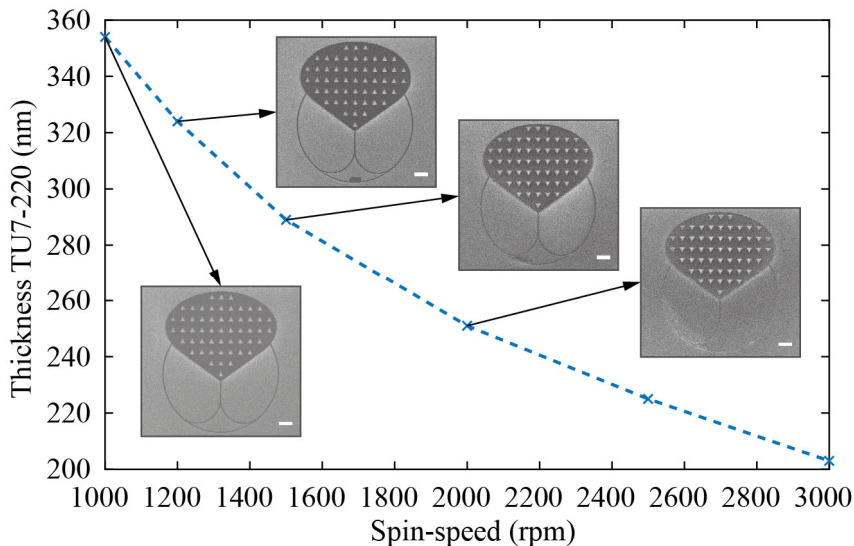


**Figure 4.6.** Spin-curve of TU7-220 and scanning electron micrographs of the imprinted structures for each resist thickness. The structures in the thickest TU7 were imprinted without defects, while the thinner layers had an increasing number of air-pockets present due to insufficient stamp filling. The scalebar is 10  $\mu\text{m}$  in all images. Reprinted from<sup>121</sup>. Copyright (2019) IOPScience (gold open access).

To measure the residual layer, we made a small scratch across the samples. **Figure 4.7** shows AFM scans of the residual removal of TU7 at different reactive ion etching times in oxygen plasma. It is important that the residual TU7 layer is completely removed as the underlying  $\text{SiO}_2$  must be fully exposed to enable silanisation and HMM binding.

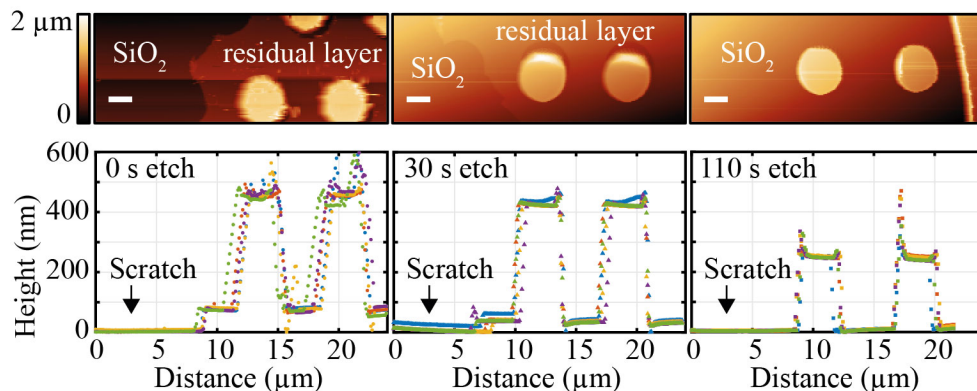


**Figure 4.7.** Atomic force measurement scans of the residual TU7 layer in the imprinted structures. The colours in the graphs represent different (single pixel) profile scans across the pillars. The scalebar is 2  $\mu\text{m}$  in all images. Reprinted from<sup>121</sup>. Copyright (2019) IOPScience (gold open access).

Scanning electron micrographs of the resulting structures are seen in **Figure 4.8** together with a series of fluorescence micrographs during an IVMA experiment with actin-myosin. We were able to obtain motility inside both the loading zones and the channels, with a good spread of filaments across the entire loading zone. However, the total number of filaments observed was very low, and we observed several detachment events upon head-on collisions, similar to previous findings<sup>24,47</sup>. The decrease in filament number may be related to a lower surface area (see **Figure 4.4**) as compared to loading zones without any pillars (which have an area of  $1200 \mu\text{m}^2$ ), in combination with filament detachment due to an increased number of collisions caused by the increase in wall surface.

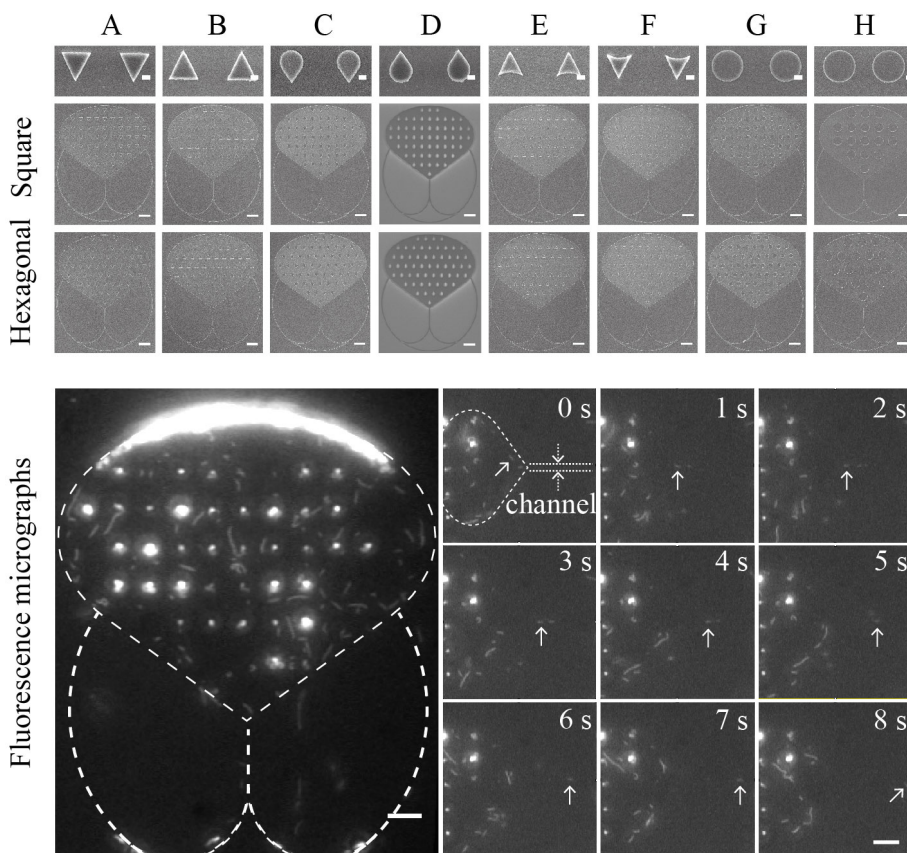


**Figure 4.8.** Scanning electron micrographs of the imprinted structures and fluorescence micrographs of an IVMA experiment with actin-myosin II showing a wide-spread filament distribution across the surface and a sequence of snap shots showing how an actin filament moves from the loading zones into a nanochannel. The scalebar for the zoom-in SEM images is  $1 \mu\text{m}$  and  $10 \mu\text{m}$  for the larger SEM images. The scalebar for the fluorescence micrograph is  $5 \mu\text{m}$  in all images. Reprinted from<sup>121</sup>. Copyright (2019) IOPScience (gold open access).

## 4.4 Concluding remarks

We demonstrated that CSAR62 is a suitable resist for patterning molecular motor-based devices by electron beam lithography, providing higher throughput than PMMA-based devices in the EBL systems used for this work. Furthermore, it is possible to fabricate both loading zones and channels in TU7 using NIL. However, the latter fabrication process needs further optimization before it can be used as a reliable method, both to improve motility inside the loading zones and to expand the imprinting to include large networks of channels. A very interesting effect to consider for future applications is the possibility of directing the motion of filaments by placing structures in specific formations, e.g., to separate different sensing areas. Moreover, it is important to keep studying the processing parameters of new resist materials as they will keep expanding the current limitations of devices and what structures are possible to fabricate. These findings strengthen and expand the studies of physically confining molecular motors in nanotechnology devices by developing processing methods in two new resists for high-throughput fabrication by EBL and NIL.

# 5 Computing with molecular motors

*This chapter describes the progress toward computing in large-scale networks using molecular motors. The so-called exact cover (EXCOV) problem is presented in more detail and the conversion into the subset sum problem is described. We present the measures taken to realise large-scale computation with molecular motors as well as the progress towards experimentally solving a ~1000-solution parallel computation network.*

## 5.1 Motivation and previous work

NBC with molecular motors was first published in 2016<sup>1</sup>, solving a small proof-of-principle SSP<sup>34</sup>, which asks what sums are possible to create from a given set of numbers (see example in Chapter 1). As described in the previous study<sup>1</sup>, we use a channel network with two different types of junctions, split and pass, to direct the motion of our agents. The filaments are collected from the buffer in the large loading zones which guide them into the networks (see **Figure 1.2**). Filaments entering a pass junction are only allowed to travel straight, following the path from which they came. At the split junctions, the filaments can turn either right or travel straight down (looking at the network from above). If they go right a number is added, and if they go straight down, no number is added. The value of the added number matches the number of pass junctions the filament will pass until the next split junction. Each exit at the end of the network, corresponds to a different solution in increasing order, meaning that the farther right a filament travels (when viewing the network from above), the higher the resulting sum of numbers added. By using these traffic rules, the problem encoded can be solved in a massively parallel manner within polynomial time, without knowing the solutions in advance, i.e., the numbers and solutions will be defined by the junction positions.

During the course of this thesis, we expanded this encoding to include the exact cover problem (EXCOV), by a theoretically converting (conversion developed by our collaborators<sup>122</sup>) the EXCOV problem into the SSP. The aims were to (i) implement a larger experimental network with around 1000 solutions (compared to tens previously)<sup>1</sup>, and (ii) to demonstrate the conversion of one NP-complete problem into another for NBC with molecular motors.

## 5.2 Conversion of EXCOV into SSP

The EXCOV problem asks if an exact cover of numbers can be created of a given set of sets. For instance, given the sets (1,3), (2,3), (2,4), (3,4), the exact cover corresponds to a combination of sets that, together, include each number (1-4) exactly once. In the problem Sarah encountered in the introduction, the exact cover would be the set of trips where she visits each country exactly once and thus, prevents a diplomatic crisis and mass extinction. To convert the number sets into an SSP network, we first translate each set into a binary number, where each bit represents an element in the set. In the set (1,3), position 1 and 3 will be represented by a 1, and position 2 and 4 (absent in the set) will be represented by a 0, i.e., 1 0 1 0. The set (2,3) will be represented by a 1 in position 2 and 3, and by a 0 in position 1 and 4, i.e., 0 1 1 0, see more examples in **Table 5.1**. Thereafter, each binary number is translated into its decimal number, providing a new set of numbers, which are encoded in an SSP network (see **Figure 1.2**).

**Table 5.1.** Translation of a small example of EXCOV subsets into a SSP set.

	Set	Binary number	Conversion	Decimal number
Set 1	(1,3)	1 0 1 0	$2^3+2^1$	10
Set 2	(2,3)	0 1 1 0	$2^2+2^1$	6
Set 3	(2,4)	0 1 0 1	$2^2+2^0$	5
Set 4	(3,4)	0 0 1 1	$2^1+2^0$	3
Exact cover	(1,2,3,4)	1 1 1 1	$2^3+2^2+2^1+2^0$	15

Using this encoding, the exact cover of the numbers (1-4) corresponds to the binary number (1 1 1 1) = 15. Thus, we know what sum an exact cover corresponds to, and therefore, only need to look at this network exit to find out whether or not an exact cover exists. If filaments exit at this exit, then the set of sets contains an exact cover, which for this small instance corresponds to Set 1 and Set 3.

## 5.3 Introducing “reset” junctions

As described in the introduction, the channel network consists of two types of junctions: split and pass junctions. A drawback of the binary conversion introduced in the previous section is the case of carrying numbers. When adding binary numbers,  $1+0=1$ ,  $0+0=0$  and  $0+1=1$ , but  $1+1=0$ , carrying 1 to the next bit, see example in **Table 5.2**.

**Table 5.2.** Binary addition with and without carrying numbers.

Binary addition without carry	Binary addition with carry
1 0 0 1 0 0 1	1 0 1 1 0 0 1
<u>+ 0 1 1 0 1 0 0</u>	<u>+ 0 1 1 0 1 0 0</u>
1 1 1 1 1 0 1	1 0 0 0 1 1 0 1

If numbers are carried, a subset of sets can add up to what seemingly is an exact cover but may include multiples of an element, e.g. the subsets (1,3)=1 0 1 0, (3)=0 0 1 0, (3,4)=0 0 1 1 do not contain an exact cover (as the number 2 is missing and element 3 is present in multiple sets) but still sum up to the binary number (1 1 1 1) due to carry. To avoid carrying of numbers, a third junction-type was introduced: reset junctions<sup>122</sup>, to replace split junctions where binary carry-over could occur. At reset junctions, filaments from both junction inlets exit one collective path downward, meaning no addition can occur (**Figure 5.1**).

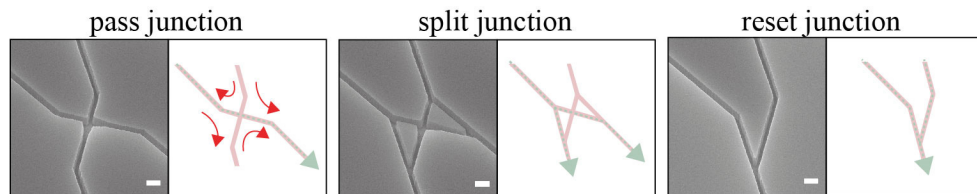


**Figure 5.1.** Scanning electron micrographs and schematic illustrations of the different junction types used in the biocomputational network. The green dashed lines mark the allowed paths and the red full lines mark illegal paths. At pass junctions the filaments continue along the same path they came from. At split junctions the filaments can turn right to add a number or travel straight down (nothing is added). At reset junctions the filaments can only travel straight down and no numbers are added. The scalebar is 500 nm for all micrographs.

## 5.4 Reducing the network size

The position of the split rows define what numbers are encoded in the network, as they define how far right a filament can travel before encountering the next split junction (see example in **Figure 1.2**). The subsets given in **Table 5.3** encodes an EXCOV problem with a solution-space of about 1000 solutions, meaning that a brute force approach would need to check about 1000 possible solutions. The encoded numbers are placed in descending order inside the network. This means that the first addition combination encountered in the sets seen in **Table 5.3** corresponds to whether or not to add 244. This is followed by the option of adding 234, 228, 224 and so on for each combination, see **Figure 5.2**. However, we do not need to encode all solutions. The number combinations creating sums above 255 as well as their corresponding exits can be discarded as they all contain multiples of the same number/bit (see **Table 5.3** and dashed lines in **Figure 5.2**). Therefore, these

sections of the network can be removed. Instead, the numbers that cannot be combined to create an exact cover can be used as entrance points. In **Figure 5.2** these numbers correspond to columns 0, 224, 228, 234 and 244. The remaining network is so small, that the agents entering at 0 cannot reach exit 255, and therefore, this entrance does not need to be part of the network. By introducing multiple inlets, we not only reduce the network size, but we also decrease the bottle-neck effect of feeding in filaments to a large network through just one inlet.

**Table 5.3.** Translation of a large example of EXCOV subsets into a SSP set.

	Set	Binary number	Conversion	Decimal number
Set 1	(7,8)	0 0 0 0 0 0 1 1	$2^1+2^0$	3
Set 2	(6,8)	0 0 0 0 0 1 0 1	$2^2+2^0$	5
Set 3	(6,7)	0 0 0 0 0 1 1 0	$2^2+2^1$	6
Set 4	(6,7,8)	0 0 0 0 0 1 1 1	$2^2+2^1+2^0$	7
Set 5	(5,8)	0 0 0 0 1 0 0 1	$2^3+2^0$	9
Set 6	(4,6,8)	0 0 0 1 0 1 0 1	$2^4+2^2+2^0$	21
Set 7	(1,2,3)	1 1 1 0 0 0 0 0	$2^7+2^6+2^5$	224
Set 8	(1,2,3,6)	1 1 1 0 0 1 0 0	$2^7+2^6+2^5+2^2$	228
Set 9	(1,2,3,5,7)	1 1 1 0 1 0 1 0	$2^7+2^6+2^5+2^3+2^1$	234
Set 10	(1,2,3,4,6)	1 1 1 1 0 1 0 0	$2^7+2^6+2^5+2^4+2^2$	244
Exact cover	(1,2,3,4,5,6,7)	1 1 1 1 1 1 1 1	$2^7+2^6+2^5+2^4+2^3+2^2+2^1+2^0$	255

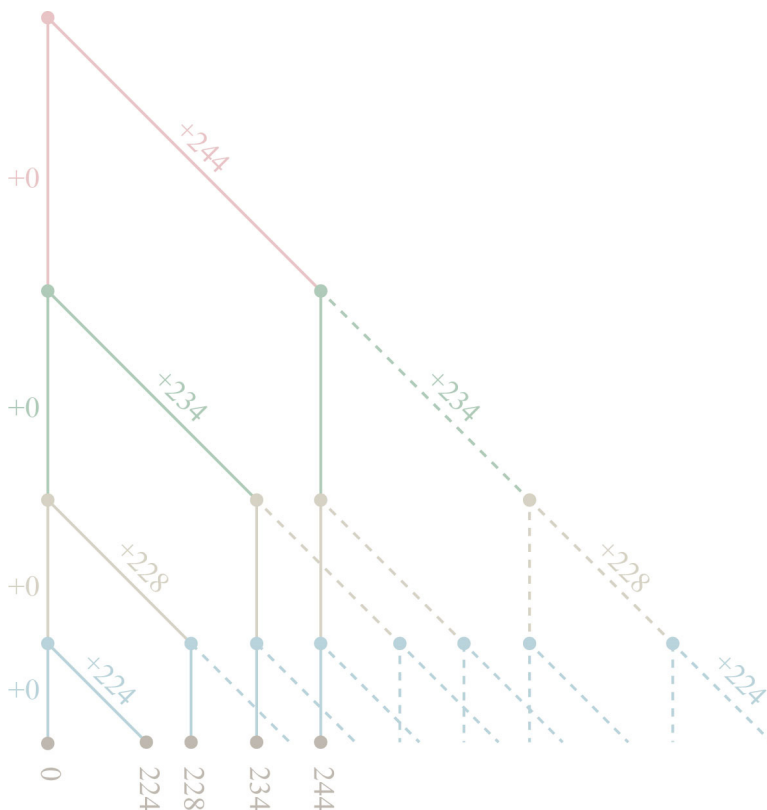


**Figure 5.2.** Top section of the network encoding the four largest decimal numbers in Table 5.3. The full lines correspond to possible paths, while the dashed lines create sums above the EXCOV sum 255. Split junctions are marked with a filled circle. At each split junction the filaments can either turn right to add a number or move downwards (no number is added). The farther right a filament moves the higher the resulting sum. Exits corresponding to sums larger than 255 can be removed as these sums contain multiple elements of the same number. Instead, a smaller network can be created, with inlets at the marked exits, increasing the number of filaments that can be fed into the network simultaneously and reducing the trajectory path of each filament.

## 5.5 Implementing the 1000 solution network

We fabricated an SSP network encoding the sets in **Table 5.3**, with the network size-reductions described in the previous section. This network encodes an EXCOV problem with  $\sim 1000$  solutions, although, only one exit, the exact cover exit, is of interest (255). The resulting design and network are seen in **Figure 5.3**. The network was fabricated in CSAR62 resist by EBL and treated with the optimised silanisation method described in Chapter 3.

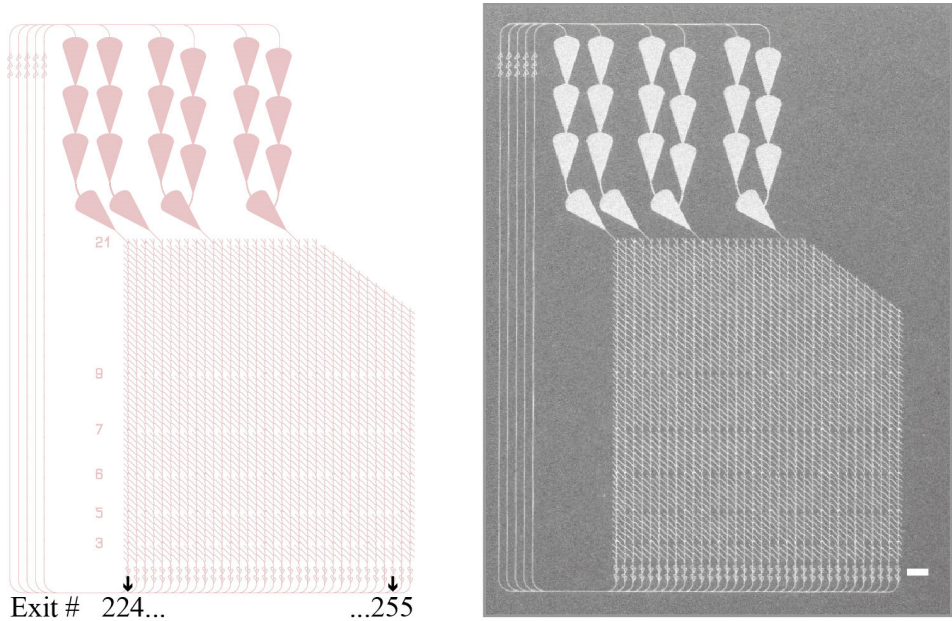


**Figure 5.3.** EBL pattern and scanning electron micrograph of the SSP sets described in **Table 5.3** after reducing the size of the networks by removing exits and number combinations above 257 (256-257 could also be removed but we left these). The scalebar in the micrograph is 20  $\mu\text{m}$ . N.B. the numbers were not exposed.

We performed motility tests using HMM (120  $\mu\text{g}/\text{ml}$ ) and Rhodamine-Phalloidin labelled actin filaments (100 nM) at 22°C. The number of filaments exiting was counted by hand and is seen in **Figure 5.4**. The pink bars represent incorrect solutions and the green bars represent correct solutions. In principle, if filaments did not make any wrong turns, we would only need one filament exiting at each correct exit to find all possible solutions to the SSP. For the EXCOV problem, this means we would only need to observe a single filament exiting at the exact cover exit.

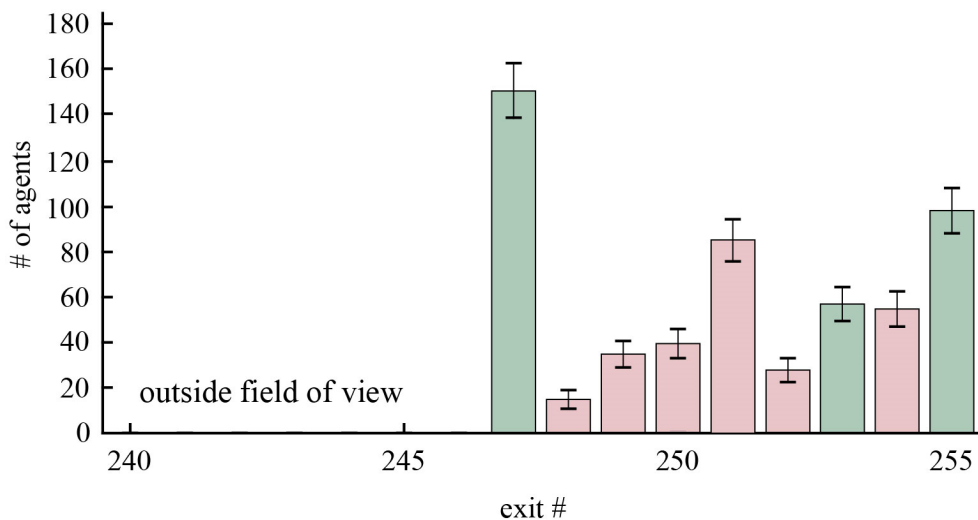


**Figure 5.4.** Histogram showing the number of filaments exiting at exits 247-255. The bars show the total number of filaments exiting each exit in seven different data sets. The error bars show the square root of the number of actin filaments per exit.

Unfortunately, in these first test devices, a large number of filaments exit at incorrect solutions, which creates false positives that prevent the true positives from being distinguishable with statistical significance. These errors arise from filaments making wrong turns in pass junctions causing them to enter illegal paths. Nicolau et al.<sup>1</sup> describe how the fraction of useable filaments,  $f(x)$ , decreases exponentially with the number of pass junction crossings,  $x$ , depending on the fractional error-rate,  $E$ :

$$f(x) = (1 - E)^x. \quad (1)$$

To calculate the error-rate we counted, by hand, the number of filaments making wrong turns in our largest data set (**Figure 5.1**). We observed 89 wrong turns out of 2306 counted filaments, providing an error-rate of 3.86% (fractional error-rate 0.0386). Nicolau et al.<sup>1</sup> found that, based on **Eq. 1**, the correct results could still be distinguished from the background noise if  $f \geq 0.15$ . In the network seen in **Figure 5.3**, the fraction of useable filaments is  $\sim 0.17$  (45 pass junction crossings), indicating that the correct results would be just about distinguishable (although not considering the number of filaments, only the error-rate and number of pass junctions). We used the error-rate to simulate the results (simulations done by Till Korten, TUD) of the filament distribution (**Figure 5.5c**) in a network with the same error-rate (here also considering the number of filaments exiting). The simulation result coincides well with the obtained experimental results (**Figure 5.5b** and **Figure 5.4**). **Figure 5.5a** shows a summed stack of the maximum intensity of a 300 s time-lapse movie of the

analysed set. The EXCOV exit has been marked with two loading zones (these are not connected to the network).

Despite our efforts to reduce the size of the network, and thus, the number of pass junction encounters, the error-rates still seem to be too high to be able to distinguish the correct solutions with the total number of filaments we were able to test so far. One reason for this difference compared what Nicolau et al.<sup>1</sup> found, is likely caused by the reset junctions presented in section 5.3. As the reset junctions concentrate filaments from two paths, this also means concentration of erroneous filaments making the error-rate distribution difficult to predict. However, reset junctions are still required to prevent errors in the calculation caused by carrying numbers. A possible solution would be to discard filaments that try to turn right at positions with reset junctions, although, this would mean that the overall signal would be decreased due to a decrease in the number of filaments. Furthermore, discarding of filaments is also problematic from an engineering perspective, as this would require yet further junction crossings, pass junctions, which may lead to an even more complex error-rate distribution. Therefore, an important necessity for network-based biocomputing to progress in the future is to reduce the number of wrong turns filaments make in the pass junctions. We have begun exploring options using 3D junctions, however, this lays beyond the scope of this thesis.

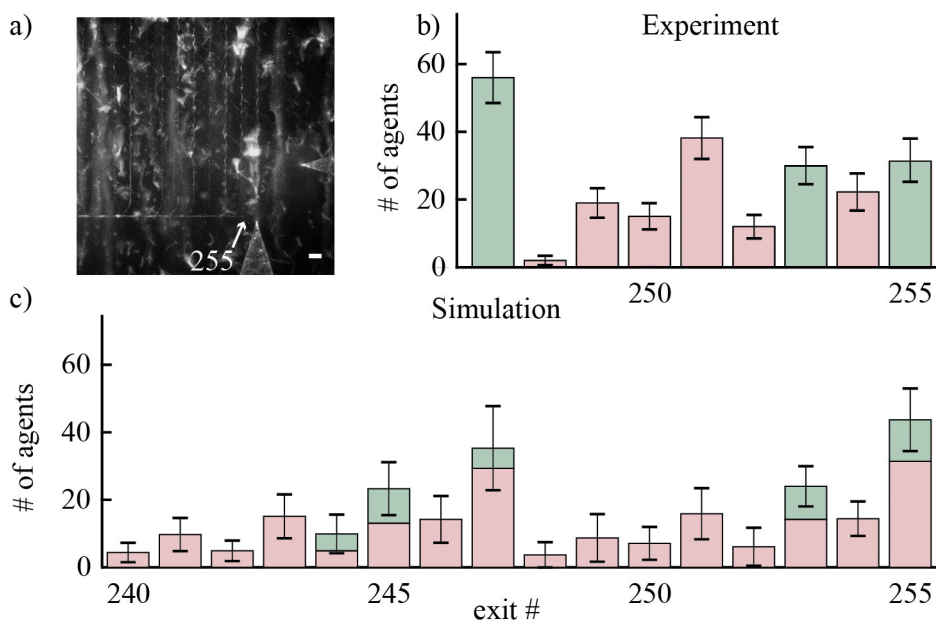


**Figure 5.5.** a) Fluorescence micrograph (scalebar 15 μm) showing the maximum intensity of a 200 s time-lapse movie at the lower right corner of the EXCOV network shown in **Figure 5.3**. The exact cover exit (255) has been marked with two loading zones. b) Experimental data for the analysed set showing the number of filaments exiting at each exit 247-255. Correct solutions are marked in green and incorrect solutions are marked in pink. c) Simulated data for error-rate 3.86%. The pink bars represent erroneous filaments that have taken illegal paths.

## 5.6 Concluding remarks

By translating sets of numbers into binary numbers and then back to a single decimal number we were able to create a theoretical conversion of the EXCOV problem into the SSP. We introduce a new network design including a new type of junction to avoid carrying numbers in binary addition, and describe how to optimise the size of the network. By minimising the size of the network, we managed to reduce the number of pass junction crossings, which contribute to a decreased fractional number of filaments. However, despite our efforts to reduce the number of pass junctions, the error-rates are still too high to clearly distinguish between correct and incorrect solutions, and need further optimisations before we can solve the encoded EXCOV problem in a statistically significant manner. Nevertheless, these developments will enable successfully solving of larger scale problems within the nearby future once the error-rates of the pass junctions can be reduced.

# 6 Architectural elements

*This chapter describes the development of two architectural elements for NBC with molecular motors. The first section presents the progress towards developing a method for creating a programmable gate, with the aim to enable versatile networks where the mathematical numbers encoded can be tuned by switching between pass and split junctions. The second section of this chapter describes the progress towards developing an electric readout method for detection of filaments passing certain check-points by using a CNT as a nanoscale field effect transistor.*

## 6.1 Motivation and previous work

### 6.1.1 Switchable junctions for programmable gating

The numbers in the mathematical problem encoded in our current network design (**Figure 1.2** and **Figure 5.3**), are defined by the placement of split and pass junctions. Different number sets have split rows located at different positions, and at different distances relative to each other. Currently, this is hard-coded into the network design during fabrication of the structures. By creating a programmable gate to transform pass junctions into split junctions and vice versa, we aim to be able to vary both the numbers within the sets, as well as the number of numbers encoded in the same network. This is highly desirable in upscaled versions of biocomputational devices, as it enables a broad variety of permutations for a dynamic algorithm using a standard large-scale network, patterned by e.g., NIL.

Previous studies of physically blocking and unblocking kinesin-1 motors have been done using the thermally activated polymer poly(N-isopropylacrylamide) (PNIPAM) on Au patterned surfaces<sup>47</sup>. These studies demonstrate the proof-of-principle of creating physical roadblocks on chemically confined tracks. PNIPAM resides in an extended form at low temperatures, blocking the motors, and curls up at higher temperatures, unblocking the motors. If the PNIPAM density is too low, the motors will still be able to bind and propel filaments. However, if the PNIPAM density is too high, motility will be completely inhibited as no motors will be able

to bind to the surface. Thus, the motor-blocking properties are determined by the density of the polymer, which can be tuned by the PNIPAM grafting temperature<sup>123</sup>.

We extended the previous PNIPAM study<sup>47</sup> by combining physical and chemical confinement of the motor system inside SiO<sub>2</sub> channels with Au floors (Paper V). To enable a switchable gating mechanism for transforming junctions between split and pass formation, we only patterned selective areas using a polymer linker for PNIPAM grafting.

## 6.1.2 Electric sensors for label free detection

In large-scale networks, a large number of filaments need to be detected at e.g., the network exits (**Figure 1.2**). For very big networks, optical readout methods are intractable, and pose limitations regarding network size as they expand outside the microscope field of view. An alternative method is instead to use nanoscale field effect transistors<sup>48</sup> (nanoFETs) for electrical detection. This would remove the need of fluorescence microscopes altogether by enabling label-free detection and thus, also eliminate drawbacks related to fluorophore bleaching and restrictions on the use of auto-fluorescent materials. Furthermore, an electrical readout method provides a better interface with electronic computers which may be of importance for future hybrid computers.

A transistor is a three-terminal device, where the conductance between two terminals is dependent on the voltage applied to a third terminal. A voltage,  $V_{SD}$ , is applied across the electrical source and drain contacts, generating a current,  $I_{SD}$ , through the transistor channel. The number of available charge carriers, and hence the current through the device, can be tuned by applying a second voltage,  $V_G$ . A schematic example of a nanoFET in a liquid is illustrated in **Figure 6.1**.

Several different types of nanoFETs have been realised based on e.g., silicon nanowires (SiNWs) or carbon nanotubes (CNTs). SiNW FETs have been used to detect changes in the pH<sup>48</sup>, by functionalising them with groups sensitive to protonation and deprotonation at different pH-values, chemically gating the SiNWs. They have also been used to detect reversible protein binding<sup>48</sup> by functionalising the SiNWs with complementary proteins, and to detect DNA hybridisation by functionalising the wires with target DNA<sup>124,125</sup>. CNT FETs (aka CNFETs), have also been used to detect DNA hybridisation in a similar manner, even down to a single molecule level<sup>49</sup>. Furthermore, CNFETs have been used for bacterial lectin detection using glycoconjugated CNTs<sup>50</sup>, and for detecting cancer biomarkers<sup>51</sup> by functionalisation of complementary proteins.

In this thesis, we try to use a (non-functionalised) single-walled CNFET to detect the passing of an actin filament (a charge particle) as a function of time due to a change in the local charge environment. To the best of our knowledge, this would

be the first nanoFET detecting an unbound protein, and would provide a reliable readout method for determining the number of filaments passing. To the date of the printing of this thesis, we have not yet been able to measure the crossing of an actin filament. So far, we have studied the buffer requirements in terms of ionic strength for a functioning biological system and for electrical detection to be possible. We also expect that the CNT needs to be raised up to the travelling height of the actin filaments to ensure that the charged filaments pass close enough (within the Debye length) to be detected. Therefore, we developed a process for fabricating pedestals for this purpose.

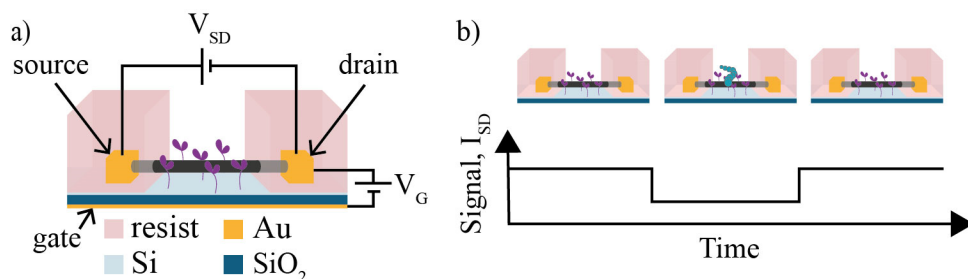


**Figure 6.1.** Schematic illustration of a nanoscale field effect transistor inside a nanochannel. a) A current,  $I_{SD}$ , is passed through the transistor by applying a voltage,  $V_{SD}$ , across the source and drain contacts. Charge carriers can be injected or depleted increasing or decreasing the conductivity through the transistor channel by applying a second voltage,  $V_G$ , across the transistor and e.g., a back gate. b) As a charged particle (here an actin filament) passes in close proximity of the transistor, the electric output signal ( $I_{SD}$ ) changes as a result of the a change in the local charge environment.

## 6.2 Programmable gating (Paper V)

**Figure 6.2** shows a schematic illustration of a programmable gate designed to switch between a pass and a split junction using the polymer PNIPAM. At low temperatures PNIPAM is extended and the junction corresponds to a pass junction. At higher temperatures, PNIPAM curls up and the junction is intended to transform into a split junction.

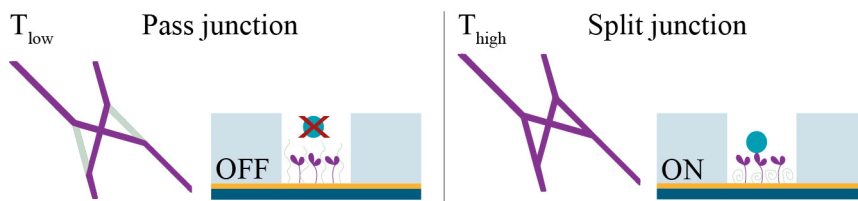


**Figure 6.2.** Schematic illustration of a switchable gate using a thermo-responsive polymer. At low temperatures the junction corresponds to a pass junction as the molecular motors are blocked by the polymer. At high temperatures the junction is transformed into a split junction as the polymer curls up, exposing the motors, enabling filament binding.

The gating mechanism only works if the PNIPAM polymer is grafted in specific regions, otherwise motility would be blocked and unblocked everywhere. To selectively graft a carboxy-terminated version of PNIPAM we used the negative tone resist poly-glycidyl methacrylate<sup>126</sup> (PGMA) as a coupling agent<sup>127</sup>, which can be patterned by EBL and developed in methyl ethyl ketone (MEK). To prevent the filaments from encountering a large step inside the channels, we diluted PGMA in anisole to two concentrations (1% and 6%), to try and obtain an as thin layer as possible. On flat surfaces, both PGMA concentrations provided uniform films (~15 nm for 1% PGMA and ~146 nm for PGMA 6%), however, on the structured surfaces we observed polymer accumulation inside the channels for the higher PGMA concentration (Figure 6.3).

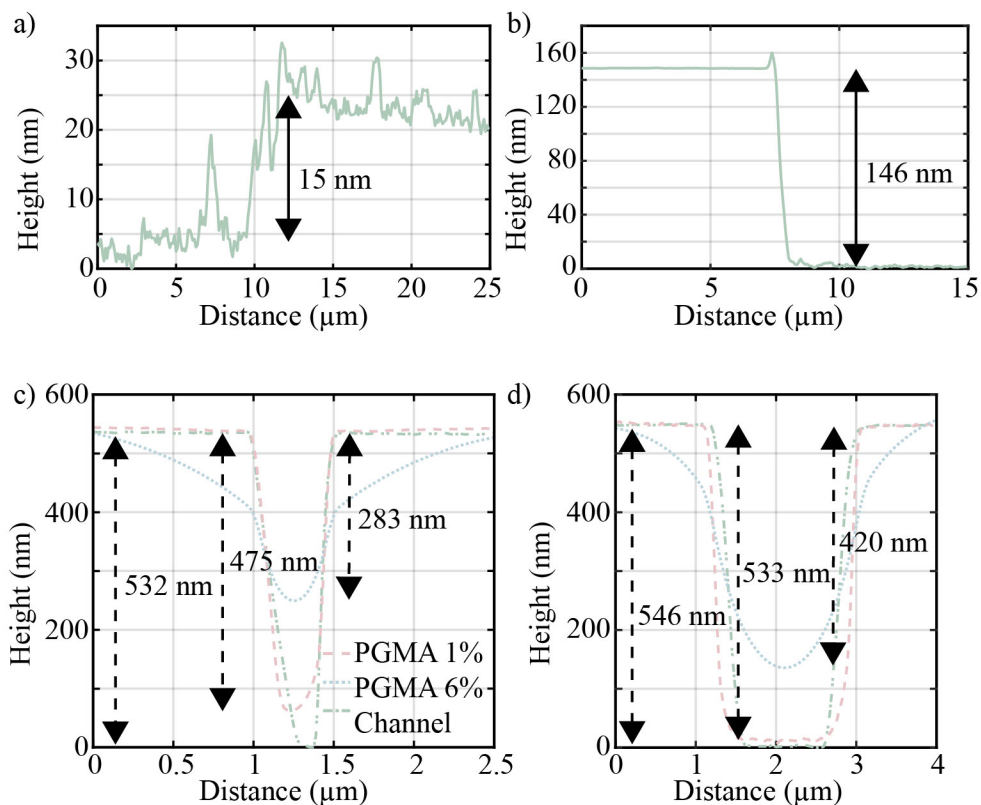


**Figure 6.3.** Profile graphs extracted from AFM scans on nanostructured surfaces (1 scan = 50 px wide). A scratch was made on a flat region of the surface to measure the thickness of a) PGMA 1% (~15 nm) and b) PGMA 6% (~146 nm). Both PGMA 1% and 6% accumulated in the c) 500 nm wide channels, but in the d) 2  $\mu\text{m}$  wide channels, only PGMA 6% was accumulated. N.B. The thinner channels suffer from AFM artefacts making it difficult to see the precise contours due to broadening effects of the AFM tip in high aspect ratio structures.

**Figure 6.4a** shows the dose test done for PGMA to find the suitable EBL exposure parameters. The doses tested ranged from  $12 \mu\text{C}/\text{cm}^2$  to  $60 \mu\text{C}/\text{cm}^2$  and, as can be seen in the optical micrograph, the pattern was overexposed for all doses but the lowest one. Furthermore, we found that a thin (7 nm) layer of PGMA always remains on the unexposed surface (measured by ellipsometry) despite longer development times (**Figure 6.4b**) and can only be removed by oxygen plasma treatment.

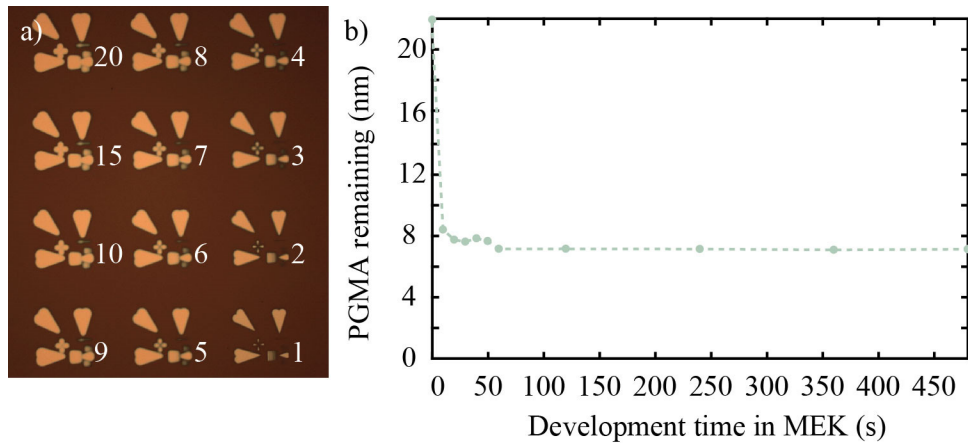


**Figure 6.4.** a) Optical micrograph of an EBL dose test showing the dose factor in white, base dose =  $12 \mu\text{C}/\text{cm}^2$ . b) Unexposed PGMA remaining on the surface after different development times in MEK.

**Figure 6.5** shows the resulting PGMA (1%) pattern inside a nanochannel after EBL exposure at  $12 \mu\text{C}/\text{cm}^2$ . The PGMA thickness is around 27 nm, although, the exact thickness is difficult to measure due to possible AFM tip broadening effects. However, as seen in **Figure 6.3**, the resist will accumulate more inside smaller channels. The PGMA thickness can be reduced further (post patterning) by etching with oxygen plasma.

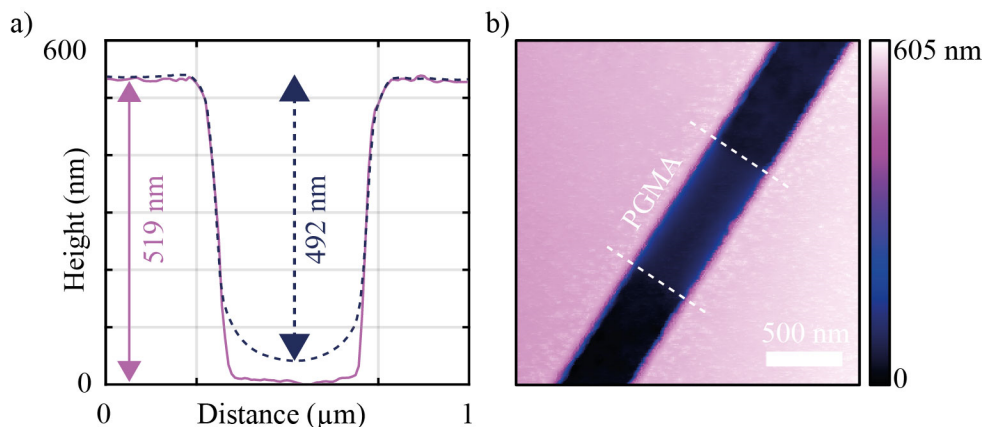


**Figure 6.5.** a) Profile plot of the b) atomic force micrograph showing the patterned PGMA patch inside a nanochannel.

**Figure 6.6** shows how motility is first inhibited (filaments are blurry) on a PNIPAM patch grafted on PGMA when the polymer is in its extended form ( $T = 25^\circ\text{C}$ ). When the temperature is increased ( $T = 35^\circ\text{C}$ ), the PNIPAM collapses, and motility is promoted (filaments appear as straight lines). **Figure 6.6** also shows how the PNIPAM grafting temperature affects the motor blocking properties. When using  $140^\circ\text{C}$  as the grafting temperature, there are still some motile filaments visible on the extended-PNIPAM patch, indicating that some filaments are still being propelled. At grafting temperature,  $T_{\text{grafting}} = 143^\circ\text{C}$ , no motile filaments can be observed on the extended-PNIPAM patch, indicating successful motor-blocking. However, at the number of filaments is lower on the contracted PNIPAM patch at  $T_{\text{grafting}} = 143^\circ\text{C}$  as compared to at  $T_{\text{grafting}} = 140^\circ\text{C}$ , indicating that the PNIPAM density could likely be further optimised between  $140\text{--}143^\circ\text{C}$ . However, these results provide a good baseline for studying switching inside nanochannels, where the system is likely to also be slightly different. The next step is to perform IVMA experiments on selectively patterned nanochannels. We are currently awaiting the first results of these experiments.

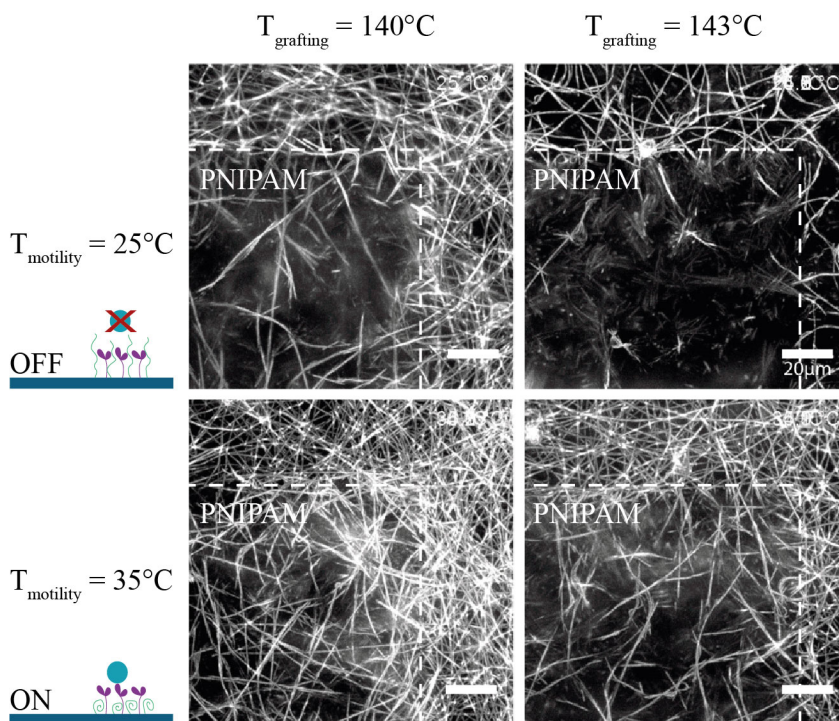


**Figure 6.6.** Data demonstrating local switching of motility on PNIPAM patches grafted on patterned PGMA. The fluorescent micrographs show the maximum projection of 85 s long movies of the local PNIPAM grafting tests. At  $T = 25^{\circ}\text{C}$  the PNIPAM is in an extended form, blocking the molecular motors and inhibiting motility (filaments appear blurry on the patch). At  $T = 35^{\circ}\text{C}$  the PNIPAM collapses and exposes the molecular motors, thus, enabling motility across the polymer patch (filaments appear as straight lines). The two columns show how the grafting temperature affects the blocking properties of PNIPAM as the polymer density varies. At the lower grafting temperature,  $T = 140^{\circ}\text{C}$ , the PNIPAM density is slightly lower and does not completely block all motors as compared to the higher grafting temperature,  $T = 143^{\circ}\text{C}$ , where no filaments move across the polymer patch. The scalebar is  $20\ \mu\text{m}$  in all images.

## 6.3 Electrical detection

An important consideration for electrical detection of charged particles, in a liquid using CNFETs, is the distance at which a particle with a specific charge is detectable. This depends on the sensitivity of the CNFET, the electric noise present in the measurement and the ionic strength of the liquid.

The sensitivity of a CNFET detector can be defined as the change in charge required to cause a detectable change in the electrical output signal ( $I_{SD}$ ), i.e., the current flowing through the CNT. This will depend on several things, including the electrical properties of the transistor itself and the type of electric contacts used. By changing the gate voltage, we can tune the region we will operate in, see **Figure 6.7**.

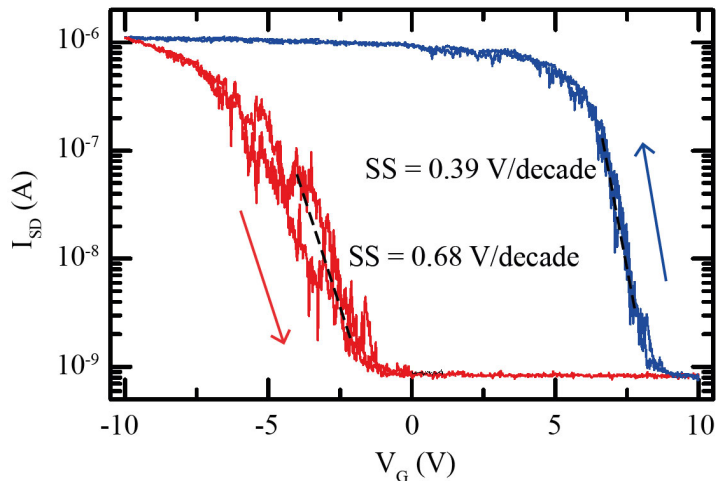


**Figure 6.7.** Measured source-drain current ( $I_{SD}$ ) of a single-walled CNFET as a function of the gate voltage ( $V_G$ ) with an applied source-drain voltage of 5 V. The dotted line shows the log linear region with a subthreshold swing of 0.39 V/decade. The arrows indicate the direction of the gate voltage-sweep. Reprinted with permission from Roman Lyttleton’s doctoral thesis<sup>128</sup>.

Here, the most sensitive region can be approximated by the log linear regime (dotted line in **Figure 6.7**), where a small change in  $V_G$  causes a large change in  $I_{SD}$ . For our best devices (developed and fabricated by Roman Lyttleton, UNSW), the subthreshold swing is 0.39 V/decade<sup>128</sup>, i.e., introducing a 390 mV voltage will change the  $I_{SD}$  by a factor 10. At typical currents of 0.5-1  $\mu\text{A}$ , our devices show an inherent pink noise width of 5-10%<sup>128</sup> of the applied current (external noise was filtered out by encapsulating the set-up in a Faraday cage). Therefore, for charged species to be detectable, they need to cause a 10% change in  $I_{SD}$ , i.e., by a factor 1.1. In the log linear regime, the current is proportional to the gate voltage as:

$$I_{SD} \propto e^{AV_G} \rightarrow \Delta I_{SD} \propto e^{A\Delta V_G} \quad (2)$$

meaning that if  $\Delta V_G = 0.39$  V causes  $\Delta I_{SD} = 10$ , then  $A \approx -5.76$ . A 10% change means  $\Delta I_{SD} = 1.1$ , which with  $A \approx -5.76$  means that  $\Delta V_G \approx 0.02$  V. Thereby, the voltage step required to detect an actin filament is 20 mV. The next question is, at what distance away from the CNT does a charged actin filament passing by exert a 20 mV potential on the CNFET?

As a measure for that we first consider the Debye length, which is defined as the length for which the electric potential of a local surplus charge decreases by  $1/e$ . The Debye length is strongly dependent on the local charges present in the liquid, here, the ionic strength of the solution, as electrolytes screen the electric potential.

The higher the ionic strength, the more heavily the electric potential from a charged filament will be screened by the intermediary electrolyte between the filament and the detector. Therefore, we want to reduce the ionic strength of our protein solutions, increasing the Debye length, which will reduce the screening effect. However, there is a biological limit to the minimum ionic strength, dictated by the biology of the molecular motor system.

**Figure 6.8** shows a simulation of how the voltage step in the output signal changes with the gap size between the filament and CNT by accounting for the Debye screening in some commonly used buffer solutions, and assuming an actin filament with a linear charge density of  $-4000 \text{ e}/\mu\text{m}^{129,130}$  (simulations done by Adam Micolich, UNSW, Manuscript in preparation). The 20 mV detection limit is marked with a red dashed line.

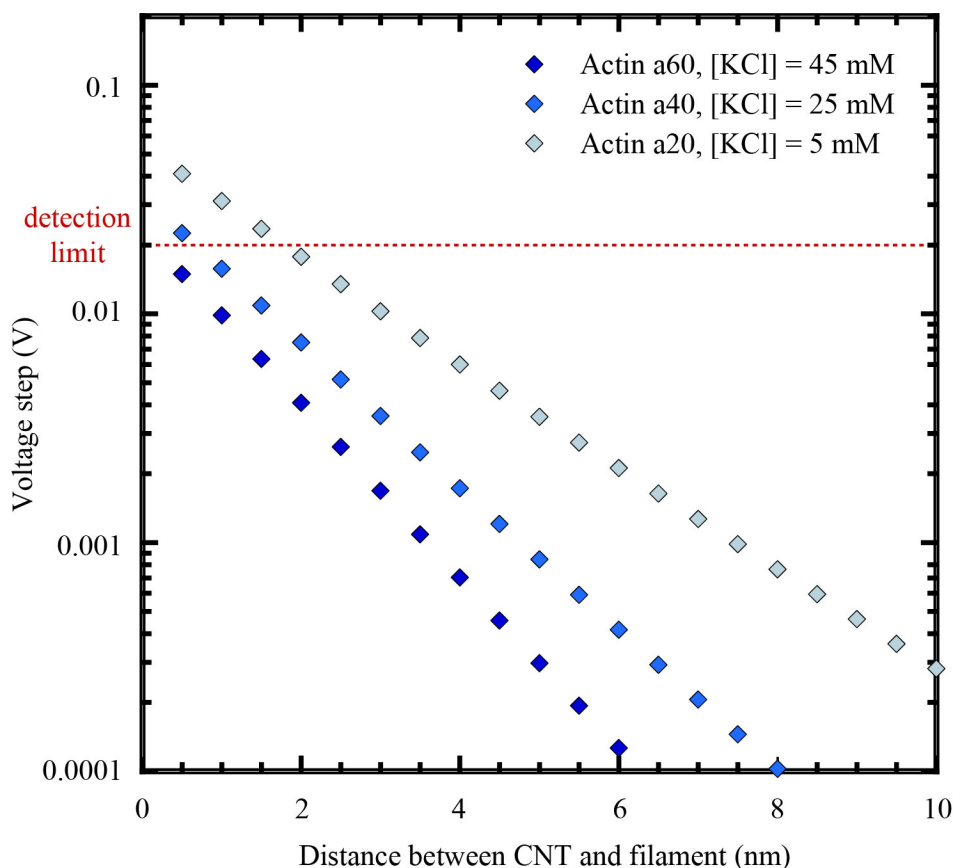


**Figure 6.8.** Simulation showing the change in potential exerted on the CNT depending on the distance between the passing actin filaments and the CNT for different buffer solutions. The red dashed line marks the detection limit (20 mV) of the current actin-myosin II CNFET devices with a sensitivity of 0.39 V/decade and pink noise  $\sim 10\%$ .

The main contribution to the ionic strength for the actin myosin system is the concentration of  $\text{KCl}^{128}$ . According to the simulations in **Figure 6.8**, the actin filaments are unlikely to be detectable in the current devices, with the  $\text{KCl}$  concentrations in the typically used a60 buffer (45 mM), but possibly in the a40 buffer (25 mM) as well as the a20 buffer (5 mM). Decreasing the  $[\text{KCl}]$  will also cause a decrease in actin filament gliding velocity as previously described<sup>131</sup>. To this end, we performed IVMA experiments to compare the motility at two different  $\text{KCl}$  concentrations, using the standard 45 mM  $\text{KCl}$  buffer and an extreme 0 mM  $\text{KCl}$  buffer. **Figure 6.9** highlights the threefold drop in velocity when decreasing the  $[\text{KCl}]$  from 45 mM to 0. The fluorescence micrographs also show an increased fragmentation of actin filaments at the lower  $[\text{KCl}]$ , consistent with the idea that the interaction strength between actin monomers is appreciably reduced at lower ionic strengths.

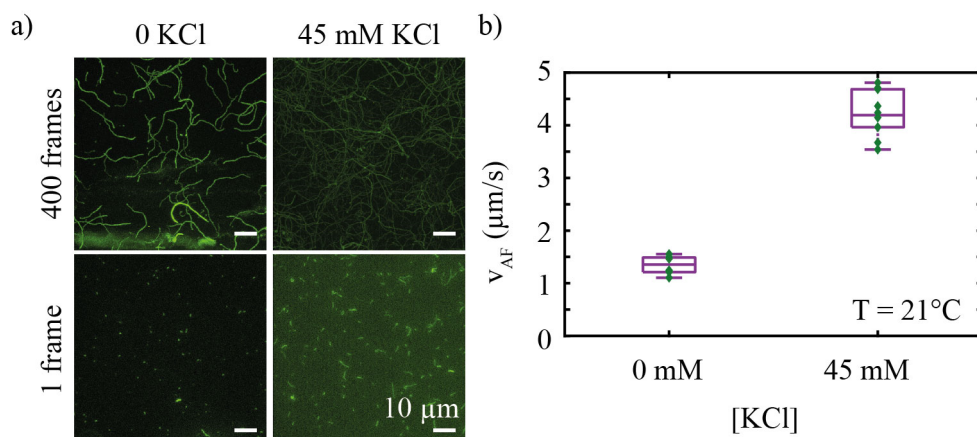


**Figure 6.9.** a) Fluorescence micrographs at 0 mM  $\text{KCl}$  and 45 mM  $\text{KCl}$  concentration. The bottom images show one frame. For the lower ionic strength, increased filament fragmentation is clearly visible. The top images show the sum of 400 frames. They show a clear difference in the actin filament path length, where the higher ionic strength provides much faster filaments. This is confirmed by point tracking 10 filaments and analysing their velocities in b) which shows that the actin filament velocity,  $v_{\text{AF}}$ , is around x3 higher at 45 mM  $\text{KCl}$  concentration as compared to at 0 mM  $\text{KCl}$ . The central mark of the boxplot shows the median of the data set, the top edge of the box shows the 75<sup>th</sup> percentile and the lower edge of the box shows the 25<sup>th</sup> percentile. The whiskers show the most extreme data points not considered to be outliers, where an outlier is defined as a point greater than 1.5 times the interquartile range away from the top or bottom of the box (none visible in the graph). Individual data points are shown in green.

HMM propels actin  $\sim 38 \text{ nm}^{105}$  above the surface, making the filament almost completely electrically screened if the CNT is placed on the channel floor. As seen in **Figure 6.8**, the allowed gap between the CNT and filament can be increased by decreasing the ionic strength, but as seen in **Figure 6.9** we want to use an as high  $[\text{KCl}]$  as possible to prevent a decrease in velocity and an increase in filament fragmentation. To bring the CNT and filaments as close together as possible, optimally completely removing the gap, we placed the CNTs on  $\text{SiO}_2$  pedestals. To

create the SiO<sub>2</sub> pedestals we selectively protected the pedestal area with EBL resist and lowered the surrounding channel floor by wet-etching with hydrogen fluoride (HF).

To examine what effect the HF-etch might have on the actin filament motility, we performed IVMAs with nanostructures comparing the etched and non-etched surfaces. **Figure 6.10** shows the summed stacks of the maximum intensity for 60 s of a non-etched and HF-etched nanostructured surface as well as the actin filament sliding velocity. No detectable difference in motility could be observed in terms of filament gliding velocity, indicating that the resulting surface supports appropriate HMM binding. This means it is possible to create SiO<sub>2</sub> pedestals for the actin-myosin system by this approach.

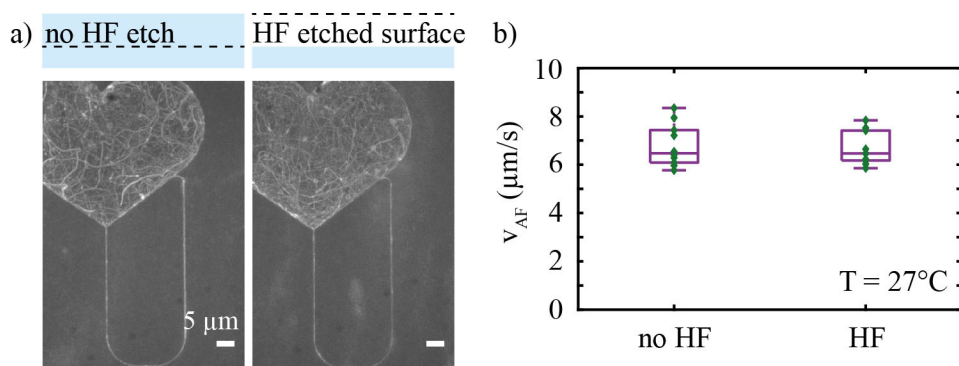


**Figure 6.10.** a) Fluorescence micrographs of non-etched and HF-etched SiO<sub>2</sub> surfaces inside polymer nanostructures. b) Actin filament sliding velocity on non-etched and HF-etched SiO<sub>2</sub> surfaces (n=10 filaments). No difference in motility quality in terms of actin filament sliding velocity is observed. See boxplot details in **Figure 6.9**. Individual data points are shown in green.

As the purpose of the pedestals is to bring the CNT and actin filament in closer contact, a major drawback would be if the filament was simply raised and actively transported across by HMM bound to the pedestal surface. To avoid this, we plan to cover the pedestals with a thin non-motile layer of parylene-C (~3 nm). The simulations in **Figure 6.8** take this additional passivating layer into account. We performed IVMA experiments on parylene-C surfaces (supplied by Jan Gluschke, UNSW) treated with oxygen plasma and found that it is possible to completely suppress motility on these surfaces, similar to the polymer walls (see **Figure 3.5**).

Finally, a basic, but key requirement for electrically detecting the actin filaments, is to be able to perform simultaneous optical and electric measurements and to correlate these two signals. To be able to bond the samples and connect them to our electronic instrumentation and to prevent the fragile cover slips from breaking due to the extra weight of the additional electronics, we created a set of 3D-printed sample holders

to support the samples in the correct positions and enable easy handling. The most successful holder is demonstrated in **Figure 6.11**.

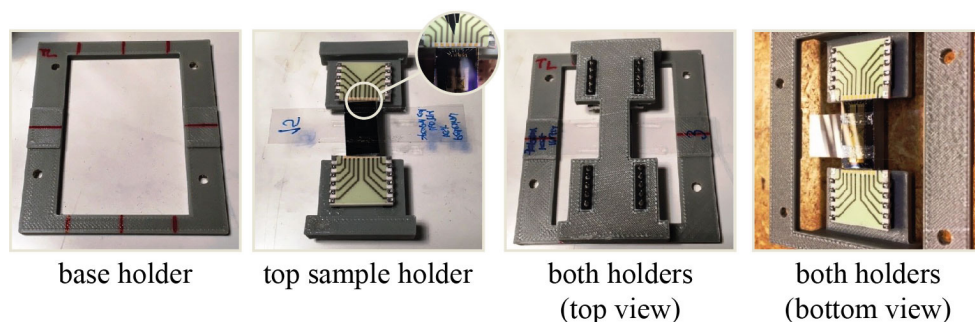


**Figure 6.11.** Pictures of the 3D-printed sample holders supporting the flow cell and sample to avoid that the flow cells break. The first image shows the base holder and the second images shows the top holder with the sample glued between two packages. The inset shows the bond wires electrically connecting the sample and package. The third image shows the top view of both holders together, and displays how the cover slip is supported by the base holder. The electric pins connected to the package protrude out through holes in the top sample holder. The fourth image shows both holders from the bottom view.

## 6.4 Concluding remarks

By using a polymer linker, PGMA, to graft selective areas with the thermo-responsive polymer PNIPAM, we successfully show local on/off switching of microtubule-kinesin 1 motility. We describe the development of the PGMA processing parameters on both flat surfaces, larger patches and inside nanoscale channels. These findings provide a stepping stone towards developing dynamic encodings for NBC with molecular motors.

To electrically detect actin filaments passing specific check-points we have begun the development of a nanoFET based on a single-walled CNT. We describe how actin filaments need to pass in close proximity of the CNTs to be detectable, and how this distance varies with the local charge environment. To reduce the distance between the filament and the CNT, we have developed a method of raising the CNTs onto SiO<sub>2</sub> pedestals that suppress motility. Furthermore, to support the cover slips and samples from the additional weight of the electronics we created easy-to-handle 3D-printed holders. Though not yet successful in measuring an actin filament passing, these results provide major steps towards an electrical readout method, although further device optimisation is most likely necessary to increase the sensitivity of the devices to enable a detectable change in the electric output.

# 7 Conclusions and outlook

This thesis focuses on the processing and fabrication development of devices for NBC with molecular motors.

In the first section of the thesis we describe three techniques that strengthen and expand the study of chemically confining molecular motors. We describe a method to improve the modification of the surface chemistry for selective protein binding by using a dedicated CVD system, where the content of TMCS, and silanisation duration can be varied. This enables a reliable surface treatment providing a high yield of motile samples, and provides an opportunity to study surface interactions of proteins on different surfaces with different hydrophobicity, without changing the chemical compound.

During the investigation of two new lithography resists we discovered that it is also possible to fabricate nanostructures without the necessity of silanisation altogether. Instead, we use the intrinsic, motility promoting properties of the negative tone NIL resist TU7, and the possibility to suppress motility on the EBL resist CSAR62 by oxidation with oxygen plasma. The filament velocity and the number of filaments across the surface is still low, but could potentially be improved by reducing the surface roughness and EBL resist-residues by using a different developer or by other chemical cleaning without loss of function.

Furthermore, we developed a method for chemically cleaning our devices from salt residue and motors, to be able to re-use our devices without the necessity of additional processing modifications. By recycling devices, we are able to decrease the overall time and material consumption, providing a more sustainable fabrication process.

As with many other parallel computation techniques, solving combinatorial problems with molecular motors is limited by various practical limitations, i.e., there are certain engineering aspects that require improvement before being able to create a viable contender that can outperform an electronic computer. One basic aspect is being able to upscale the fabrication of the physically confining structures without loss of resolution. In the second section of the thesis we present two methods for improving the throughput of molecular motor-based devices.

We switched to a more sensitive resist, CSAR62, as compared to the previously used PMMA, and describe the optimisation of the EBL patterning parameters. We

also developed a new method for patterning the large aspect ratio loading zone structures by NIL in TU7.

By redesigning the loading zones to include pillar-structures we could create areas into which polymer could be displaced during imprint. We also found that these newly introduced pillars can be used to tailor the directionality of the overall filament movement, a very useful feature within e.g., sensing applications. **Figure 7.1** shows a possible design for a sensor exploiting this directionality. The loading zone pillars here, correspond to design F in **Figure 4.4**, and will push the filaments from the large central circle towards each sensing area. An alternative design would be to use structures that cause a variety of emptying rates. These structures could for instance, be fabricated by a combination of UVL and NIL.

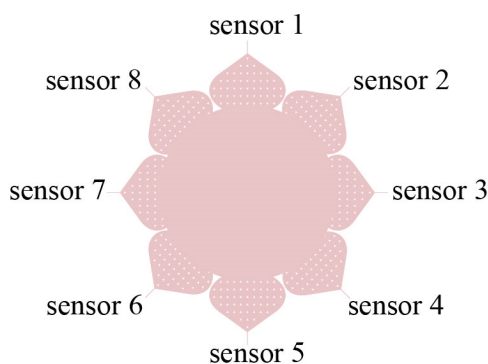


**Figure 7.1.** Possible biosensor design utilising the directional properties of the pillar-shapes and configuration described in design F, **Figure 4.4**. The filaments in solution would diffuse down into the large open central (pink) area and be pushed toward each sensor due to the shape and position of the (white) pillars.

Within this thesis we also present an algorithm for translating the NP-complete problem EXCOV into another NP-complete problem, the SSP. We describe a method of reducing the network size to reduce the number of filaments required, and we describe how challenges related to carrying numbers in binary addition can be avoided. We try to solve a large-scale network with  $\sim 1000$  solutions, but the current error-rates i.e., wrong turns within the network, are too high to find a statistically significant solution.

To reduce the error-rates and thus, the number of filaments required, we are currently developing a new type of junction with three dimensional crossings, fabricated by two photon polymerisation technology. In such a structure, filaments will move across “bridges” and through “tunnels” (**Figure 7.2**). If successful, this would enable complete elimination of the risk of filaments taking a wrong turn at pass junction crossings. However, these types of junctions are not compatible with the switchable junctions described in Chapter 6.

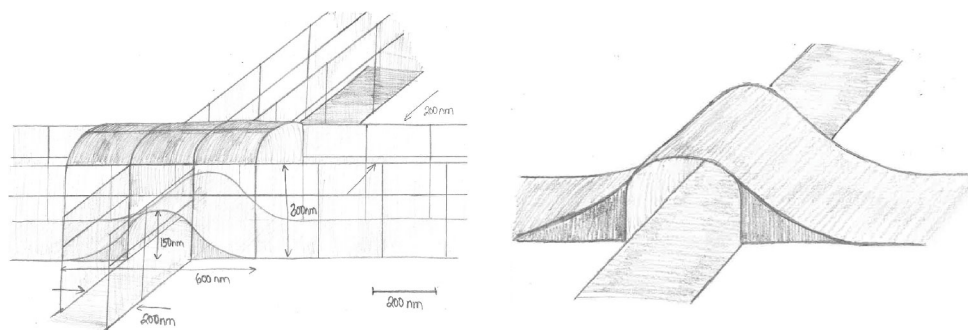


**Figure 7.2.** Schematic illustrations of a 3D-junction that eliminates the risk of filaments making wrong turns at pass junctions. By creating bridges and tunnels, there is only one possible pathway for the filaments.

Another draw-back with the current network design is the relatively slow input of exploring agents. Despite describing a method of increasing the number of locations at which filaments are fed in, they are still all inserted at the top of the network through a limited number of entrance points. For very large networks, this will cause a major bottle-neck due to the vast number of filaments required to solve large networks. To remove this bottle-neck, we are currently working on a method to split and grow our filamentous agents while in the network. However, if any information is stored on the filament itself, a split and regrowth process will continuously cause this information to dilute.

Storing data on filaments is important in problems that require information about what paths have been explored, e.g., in the travelling salesman problem Sarah encountered in the introduction. In principle, all NP-complete problems can be translated into each other, and the network encoding presented in this thesis might not always be the most optimum design for all problems. At the moment, we are working on a second, compact network design for solving the Boolean Satisfiability problem, which we translate into the travelling salesman problem. The current design (not shown here) will however, only work if the filaments can be tagged with information on where they have been. Any methods for splitting and re-growing filaments must therefore, also include the transfer of this information. However, we are currently unable to store and manipulate information on our filaments. Nevertheless, in the future, barcoding by bleaching fluorophores or tagging by e.g., attaching DNA oligonucleotides might be feasible options.

In the final section of this thesis we described the development of two architectural elements for NBC with molecular motors, a programmable gating mechanism and an electric sensor.

We describe a new method of selectively grafting the thermo-responsive polymer PNIPAM on nanostructures, allowing local switching of motility by creating physical roadblocks, veiling and unveiling the surface-bound molecular motors. By

introducing switchable paths, we can create dynamic encodings that allow different numbers and a different number of numbers to be encoded within the same algorithm. This allows the fabrication of very versatile devices that can be patterned with a standard, predefined, large-scale network structure e.g., using high throughput NIL. In combination with our regeneration process, these advancements are steps towards real-life applications of NBC with molecular motors due to the reduced fabrication costs and upscaling properties.

There are also other methods one could envisage to tune the motility. One possible method would be to not physically block the motors but instead switch the motor function itself. Another method could be to include a tuneable surface chemistry to selectively collapse the motors, e.g., by changing the surface hydrophobicity, or to change the binding affinity. A precondition for any future method is however, that it must be reversible to ensure maximum flexibility.

The NBC method presented in this thesis relies on an optical readout and counting filaments by hand. In collaboration with a group of students, our research group is currently developing a deep learning algorithm for analysis of filaments in our IVMA experiments, regarding the number of exiting events, the number of wrong turns, the relationship between certain filament behaviour and specific filament dimensions or device structures. This would simplify the data analysis during development, and provide the possibility to map a wide range of variables providing massive information on how our system can be optimised further. Naturally, only visible information can be analysed, restricting the amount of area that can be studied simultaneously as we are limited by the microscope field of view. For counting the filament exit events, we would instead like to employ an electrical readout method using a single-walled CNT as a nanoFET as this removes the restraints of using a microscope all together.

Though we are yet to integrate these nanoFETs and detect filaments exiting, we describe how close by filaments need to pass in order to be detectable. We also describe methods of how the filaments can be brought within this range, by raising the CNT onto pedestals, and by decreasing the ionic strength to decrease the screening of the electric potential. Furthermore, we show a way to perform optical and electrical measurements simultaneously without breaking the samples due to the additional weight of the electronics.

These improvements, together with other, new and promising ideas, have the potential to boost the field of NBC using not only molecular motors as agents, but also other agents, such as bacteria, artificial motors or perhaps some other self-propelling, highly energy-efficient agent. I do believe, that solving combinatorial problems beyond what has been possible so far, is actually within reach in the nearby future.

# References

1. Nicolau, D. V. J. *et al.* Parallel computation with molecular motor-propelled agents in nanofabricated networks. *PNAS* **113**, 2591–2596 (2016).
2. Goldreich, O. *P, NP, and NP-Completeness-The Basics of Computational Complexity.* (Cambridge university press, 2010).
3. Mukhanov, O. A. Energy-efficient single flux quantum technology. *IEEE Trans. Appl. Supercond.* **21**, 760–769 (2011).
4. Madden, P. H. Dispelling the myths of parallel computing. *IEEE Des. Test* **30**, 58–64 (2013).
5. Adleman, L. M. Molecular Computation of Solutions to Combinatorial Problems. *Science (80-. )*. **266**, 1021–1024 (1994).
6. Lipton, R. J. DNA Solution of Hard Computational Problems. *Science (80-. )*. **268**, 542–545 (1995).
7. Braich, R. S. *et al.* Solution of a 20-variable 3-SAT problem on a DNA computer. *Science* **296**, 499–502 (2002).
8. Chiu, D. T., Pezzoli, E., Wu, H., Stroock, a D. & Whitesides, G. M. Using three-dimensional microfluidic networks for solving computationally hard problems. *Proc. Natl. Acad. Sci. U. S. A.* **98**, 2961–2966 (2001).
9. Ladd, T. *et al.* Quantum computers. *Nature* **464**, 45–53 (2010).
10. Barclay, C. J. Estimation of cross-bridge stiffness from maximum thermodynamic efficiency. *J. Muscle Res. Cell Motil.* **19**, 855–864 (1998).
11. Korten, T., Månsson, A. & Diez, S. Towards the application of cytoskeletal motor proteins in molecular detection and diagnostic devices. *Curr. Opin. Biotechnol.* **21**, 477–488 (2010).
12. Kron, S. J. & Spudich, J. A. Fluorescent actin filaments move on myosin fixed to a glass surface. *Proc. Natl. Acad. Sci. U. S. A.* **83**, 6272–6276 (1986).
13. Howard, J., Hudspeth, A. J. & Vale, R. D. Movement of microtubules by single kinesin molecules. *Nature* **342**, 154–158 (1989).
14. Sheetz, M. P. & Spudich, J. A. Movement of myosin-coated fluorescent beads on actin cables in vitro. *Nature* **303**, 31–35 (1983).
15. Kron, S. J., Toyoshima, Y. Y., Uyeda, T. Q. P. & Spudich, J. A. Assays for

- Actin Sliding Movement over Myosin-Coated Surfaces. *Methods Enzymol.* **196**, 399–416 (1991).
16. Kishino, A. & Yanagida, T. Force measurements by micromanipulation of a single actin filament by glass needles. *Nature* **334**, 74–76 (1988).
  17. Murphy, C. T., Rock, R. S. & Spudich, J. A. A myosin II mutation uncouples ATPase activity from motility and shortens step size. *Nat. Cell Biol.* **3**, 311–315 (2001).
  18. Toyoshima, Y. Y. *et al.* Myosin subfragment-1 is sufficient to move actin filaments in vitro. *Nature* **328**, 536–539 (1987).
  19. Homsher, E., Kim, B., Bobkova, A. & Tobacman, L. S. Calcium regulation of thin filament movement in an in vitro motility assay. *Biophys. J.* **70**, 1881–1892 (1996).
  20. Bunk, R. *et al.* Actomyosin motility on nanostructured surfaces. *Biochem. Biophys. Res. Commun.* **301**, 783–788 (2003).
  21. Lard, M. *et al.* Ultrafast molecular motor driven nanoseparation and biosensing. *Biosens. Bioelectron.* **48**, 145–152 (2013).
  22. ten Siethoff, L. *et al.* Molecular motor propelled filaments reveal light-guiding in nanowire arrays for enhanced biosensing. *Nano Lett.* **14**, 737–742 (2014).
  23. Månsson, A. Translational actomyosin research: Fundamental insights and applications hand in hand. *J. Muscle Res. Cell Motil.* **33**, 219–233 (2012).
  24. Sundberg, M. *et al.* Actin filament guidance on a chip: Toward high-throughput assays and lab-on-a-chip applications. *Langmuir* **22**, 7286–7295 (2006).
  25. Clemmens, J. *et al.* Mechanisms of microtubule guiding on microfabricated kinesin-coated surfaces: Chemical and topographic surface patterns. *Langmuir* **19**, 10967–10974 (2003).
  26. Hiratsuka, Y., Tada, T., Oiwa, K., Kanayama, T. & Uyeda, T. Q. P. Controlling the direction of kinesin-driven microtubule movements along microlithographic tracks. *Biophys. J.* **81**, 1555–1561 (2001).
  27. Bunk, R. *et al.* Guiding motor-propelled molecules with nanoscale precision through silanized bi-channel structures. *Nanotechnology* **16**, 710–717 (2005).
  28. Hess, H. *et al.* Molecular Shuttles Operating Undercover: A New Photolithographic Approach for the Fabrication of Structured Surfaces Supporting Directed Motility. *Nano Lett.* **3**, 1651–1655 (2003).
  29. Nicolau, D. V., Suzuki, H., Mashiko, S., Taguchi, T. & Yoshikawa, S. Actin motion on microlithographically functionalized myosin surfaces and tracks.

- Biophys. J.* **77**, 1126–1134 (1999).
30. Suzuki, H., Yamada, A., Oiwa, K., Nakayama, H. & Mashiko, S. Control of actin moving trajectory by patterned poly(methylmethacrylate) tracks. *Biophys. J.* **72**, 1997–2001 (1997).
  31. Månsson, A., Bunk, R., Sundberg, M. & Montelius, L. Self-organization of motor-propelled cytoskeletal filaments at topographically defined borders. *J. Biomed. Biotechnol.* **2012**, (2012).
  32. Lin, C.-T., Kao, M.-T., Kurabayashi, K. & Meyhofer, E. Self-Contained, Biomolecular Motor-Driven Protein Sorting and Concentrating in an Ultrasensitive Microfluidic Chip. *Nano Lett.* **8**, 1041–1046 (2008).
  33. Katira, P. & Hess, H. Two-stage capture employing active transport enables sensitive and fast biosensors. *Nano Lett.* **10**, 567–572 (2010).
  34. Bokhari, S. S. Parallel solution of the subset-sum problem: an empirical study. *Concurr. Comput. Pract. Exp.* **24**, 2241–2254 (2012).
  35. Hodge, R. *The molecules of life: DNA, RNA and proteins*. (Infobase publishing, 2009).
  36. Holmes, K. C., Popp, D., Gebhard, W. & Kabsch, W. Atomic model of the actin filament. *Nature* **347**, 44–49 (1990).
  37. Gittes, F., Mickey, B., Nettleton, J. & Howard, J. Flexural rigidity of microtubules and actin filaments measured from thermal fluctuations in shape. *J. Cell Biol.* **120**, 923–934 (1993).
  38. Hackney, D. D. Highly processive microtubule-stimulated ATP hydrolysis by dimeric kinesin head domains. *Nature* **377**, 448–450 (1995).
  39. Albet-Torres, N. *et al.* Mode of heavy meromyosin adsorption and motor function correlated with surface hydrophobicity and charge. *Langmuir* **23**, 11147–11156 (2007).
  40. Nakanishi, K., Sakiyama, T. & Imamura, K. On the adsorption of proteins on solid surfaces, a common but very complicated phenomenon. *Biosci. Bioeng.* **91**, 233–244 (2001).
  41. van der Veen, M., Stuart, M. C. & Norde, W. Spreading of proteins and its effect on adsorption and desorption kinetics. *Colloids Surfaces B Biointerfaces* **54**, 136–142 (2007).
  42. Hanson, K. L. *et al.* Polymer surface properties control the function of heavy meromyosin in dynamic nanodevices. *Biosens. Bioelectron.* **93**, 305–314 (2017).
  43. Sundberg, M. *et al.* Silanized surfaces for in vitro studies of actomyosin function and nanotechnology applications. *Anal. Biochem.* **323**, 127–138 (2003).

44. Clemmens, J. *et al.* Motor-protein roundabouts : Microtubules moving on kinesin-coated tracks through engineered networks. *Lab Chip* **4**, 83–86 (2004).
45. Bunk, R. *et al.* Guiding molecular motors with nano-imprinted structures. *Jpn. J. Appl. Phys.* **44**, 3337–3340 (2005).
46. Scheer, H.-C. Problems of the nanoimprinting technique for nanometer scale pattern definition. *J. Vac. Sci. Technol. B Microelectron. Nanom. Struct.* **16**, 3917 (1998).
47. Schroeder, V., Korten, T., Linke, H., Diez, S. & Maximov, I. Dynamic Guiding of Motor-Driven Microtubules on Electrically Heated, Smart Polymer Tracks. *Nano Lett.* **13**, 3434–3438 (2013).
48. Cui, Y., Wei, Q., Park, H. & Lieber, C. M. Nanowire nanosensors for highly sensitive and selective detection of biological and chemical species. *Science* (80-. ). **293**, 1289–1292 (2001).
49. Sorgenfrei, S. *et al.* Label-free single-molecule detection of DNA-hybridization kinetics with a carbon nanotube field-effect transistor. *Nat. Nanotechnol.* **6**, 126–132 (2011).
50. Vedala, H. *et al.* Nanoelectronic Detection of Lectin-Carbohydrate Interactions Using Carbon Nanotubes. *Nano Lett.* **11**, 170–175 (2010).
51. Lerner, M. B. *et al.* Hybrids of a Genetically Engineered Antibody and a Carbon Nanotube Transistor for Detection of Prostate Cancer Biomarkers. *ACS Nano* **6**, 5143–5149 (2012).
52. Governatori, G., Olivieri, F., Scannapieco, S., Rotolo, A. & Cristani, M. Strategic argumentation is NP-complete. in *Frontiers in Artificial Intelligence and Applications* **263**, 399–404 (2013).
53. Verma, T. S. & Pearl, J. Deciding Morality of Graphs is NP-complete. in *Uncertainty in Artificial Intelligence* 391–399 (1993). doi:10.1016/b978-1-4832-1451-1.50052-4
54. Fraenkel, A. S. Complexity of protein folding. *Bull. Math. Biol.* **55**, 1199–1210 (1993).
55. Berger, B. & Leighton, T. Protein Folding in the Hydrophobic-Hydrophilic ( HP ) Model is NP-Complete. *J. Comput. Biol.* **5**, 27–40 (1998).
56. Yan, G., Zhou, T., Hu, B., Fu, Z.-Q. & Wang, B.-H. Efficient routing on complex networks. *Phys. Rev. E* **73**, 046108 (2006).
57. Homsher, E., Wang, F. & Sellers, J. R. Factors affecting movement of F-actin filaments propelled by skeletal muscle heavy meromyosin. *Am. J. Physiol.* **262**, C714–C723 (1992).
58. Huxley, A. F. Muscle structure and theories of contraction. *Prog Biophys*

- Biophys Chem* **7**, 255–318 (1957).
59. Huxley, H. E. The Mechanism of Muscular Contraction. *Science* (80-. ). **164**, 1356–1366 (1969).
  60. Rayment, I. *et al.* Structure of the Actin-Myosin Complex and Its Implications for Muscle Contraction. *Science* (80-. ). **261**, 58–65 (1993).
  61. Alberts, B. *et al.* *Essential cell biology*. (Garland Science, 2010).
  62. Moore, P. B., Huxley, H. E. & DeRosier, D. J. Three-dimensional reconstruction of F-actin, thin filaments and decorated thin filaments. *J. Mol. Biol.* **50**, 279–296 (1970).
  63. Jockusch, B. M. *The Actin Cytoskeleton*. (Springer, 2017).
  64. Bengtsson, E. *et al.* Myosin-Induced Gliding Patterns at Varied [MgATP] Unveil a Dynamic Actin Filament. *Biophys. J.* **111**, 1465–1477 (2016).
  65. Vikhorev, P. G., Vikhoreva, N. N. & Månsson, A. Bending flexibility of actin filaments during motor-induced sliding. *Biophys. J.* **95**, 5809–5819 (2008).
  66. Odronitz, F. & Kollmar, M. Drawing the tree of eukaryotic life based on the analysis of 2,269 manually annotated myosins from 328 species. *Genome Biol.* **8**, R196 (2007).
  67. Hartman, M. A. & Spudich, J. a. The myosin superfamily at a glance. *J. Cell Sci.* **125**, 1627–1632 (2012).
  68. Bordas, J. *et al.* Extensibility and symmetry of actin filaments in contracting muscles. *Biophys. J.* **77**, 3197–207 (1999).
  69. Margossian, S. & Lowey, S. Preparation of myosin and its subfragments from rabbit skeletal-muscle. *Methods Enzymol.* **85**, 55–71 (1982).
  70. Lu, R. C. Identification of a region susceptible to proteolysis. *PNAS* **77**, 2010–2013 (1980).
  71. Mellema, J. E., Van Bruggen, E. F. J. & Gruber, M. Uranyl oxalate as a negative stain for electron microscopy of proteins. *Biochim. Biophys. Acta* **140**, 180–182 (1967).
  72. Kodama, T. Thermodynamic analysis of muscle ATPase mechanisms. *Physiol. Rev.* **65**, 467–551 (1985).
  73. Ebashi, S., Ebashi, F. & Kodama, A. Troponin as the Ca<sup>++</sup>-receptive Protein in the Contractile System. *J. Biochem.* **62**, 137–138 (1967).
  74. Walcott, S., Warshaw, D. M. & Debold, E. P. Mechanical coupling between myosin molecules causes differences between ensemble and single-molecule measurements. *Biophys. J.* **103**, 501–510 (2012).
  75. Howard, J. *Mechanics of motor proteins and the cytoskeleton*. (Sinauer

Associates, 2001).

76. Nitta, T. & Hess, H. Dispersion in active transport by kinesin-powered molecular shuttles. *Nano Lett.* **5**, 1337–1342 (2005).
77. Goldstein, L. S. B. & Philp, A. V. The road less traveled: Emerging principles of kinesin motor utilization. *Annu. Rev. cell Dev. Biol.* **15**, 141–83 (1999).
78. Rice, S. *et al.* A structural change in the kinesin motor protein that drives motility. *Nature* **402**, 778–84 (1999).
79. Nitta, T. *et al.* Comparing guiding track requirements for myosin-and kinesin-powered molecular shuttles. *Nano Lett.* **8**, 2305–2309 (2008).
80. Zhang, M., Desai, T. & Ferrari, M. Proteins and cells on PEG immobilized silicon surfaces. *Biomaterials* **19**, 953–960 (1998).
81. van den Heuvel, M. G. L., Butcher, C. T., Smeets, R. M. M., Diez, S. & Dekker, C. High rectifying efficiencies of microtubule motility on Kinesin-coated gold nanostructures. *Nano Lett.* **5**, 1117–1122 (2005).
82. Gangnaik, A. S., Georgiev, Y. M. & Holmes, J. D. New Generation Electron Beam Resists: A Review. *Chem. Mater.* **29**, 1898–1917 (2017).
83. Manfrinato, V. R. *et al.* Resolution limits of electron-beam lithography towards the atomic scale. *Nano Lett.* **13**, 1555–1558 (2013).
84. Raith GmbH, Dortmund. Available at: [www.raith.com](http://www.raith.com).
85. Stepanova, M. & Dew, S. *Nanofabrication: Techniques and Principles.* (Springer, 2012). doi:10.1007/978-3-7091-0424-8
86. Kyser, D. F. & Ting, C. H. Voltage dependence of proximity effects in electron beam lithography. *J. Vac. Sci. Technol.* **16**, 1305–8 (1979).
87. Chou, S. Y., Krauss, P. R., Zhang, W., Guo, L. & Zhuang, L. Sub-10 nm imprint lithography and applications. *J. Vac. Sci. Technol.* **15**, 2897–2904 (1997).
88. Chou, S., Krauss, P. & Renstrom, P. Imprint of sub-25nm vias and trenches in polymers. *Appl. Phys. Lett.* **67**, 3114 (1995).
89. Tang, M.-J., Xie, H.-M., Li, Y.-J., Li, X.-J. & Wu, D. A New Grating Fabrication Technique on Metal Films Using UV-Nanoimprint Lithography. *Chinese Phys. Lett.* **29**, 098101 (2012).
90. Guo, L. J. Recent progress in nanoimprint technology and its applications. *J. Phys. D. Appl. Phys.* **37**, R123–R141 (2004).
91. Rey, A., Rothe, J. & Marple, A. Path-Disruption Games: Bribery and a Probabilistic Model. *Theory Comput. Syst.* **60**, 222–252 (2017).
92. Diffie, W. & Hellman, M. E. New Directions in Cryptography. *IEEE Trans.*

- Inf. Theory* **22**, 644–654 (1976).
93. Cook, S. A. The complexity of theorem proving procedures. *Proc. 3rd Annu. ACM Symp. Theory Comput.* 151–158 (1971).
  94. Levin, L. A. Universal Sequential Search Problems. *Probl. Inf. Transm.* **9**, 115–116 (1973).
  95. Karp, R. M. *Reducibility among combinatorial problems. Complexity of Computer Computations* (Plenum, 1972). doi:10.1007/978-3-540-68279-0\_8
  96. Whitesides, G. M. The origins and the future of microfluidics. *Nature* **442**, 368–373 (2006).
  97. Qian, L. & Winfree, E. Scaling up digital circuit computation with DNA strand displacement cascades. *Science (80-. )*. **332**, 1196–1201 (2011).
  98. Boneh, D., Dunworth, C., Lipton, R. J. & Sgall, J. On the computational power of DNA. *Discret. Appl. Math.* **71**, 79–94 (1996).
  99. Ouyang, Q., Kaplan, P. D., Liu, S. & Libchaber, A. DNA solution of the maximal clique problem. *Science (80-. )*. **278**, 446–449 (1997).
  100. R Landauer. Irreversibility and Heat Generation in the Computing Process. *IBM J. Res. Dev.* **5**, 183–191 (1961).
  101. Jaber, J. a., Chase, P. B. & Schlenoff, J. B. Actomyosin-Driven Motility on Patterned Polyelectrolyte Mono- and Multilayers. *Nano Lett.* **3**, 1505–1509 (2003).
  102. Harada, Y., Sakurada, K., Aoki, T., Thomas, D. D. & Yanagida, T. Mechanochemical coupling in actomyosin energy transduction studied by in vitro movement assay. *J. Mol. Biol.* **216**, 49–68 (1990).
  103. Albet-Torres, N., Gunnarsson, A., Persson, M., Balaz, M. & Höök, F. Molecular motors on lipid bilayers and silicon dioxide: different driving forces for adsorption. *Soft Matter* **6**, 3211–3219 (2010).
  104. Ramsden, J. J., Roush, D. J., Gill, D. S., Kurrat, R. & Willson, R. C. Protein Adsorption Kinetics Drastically Altered by Repositioning a Single Charge. *J. Am. Chem. Soc.* **117**, 8511–8516 (1995).
  105. Persson, M. *et al.* Heavy meromyosin molecules extending more than 50 nm above adsorbing electronegative surfaces. *Langmuir* **26**, 9927–9936 (2010).
  106. Warrick, H. M. *et al.* In vitro methods for measuring force and velocity of the actin-myosin interaction using purified proteins. *Methods Cell Biol.* **39**, 1–21 (1993).
  107. Rivelino, D. *et al.* Acting on actin: The electric motility assay. *Eur. Biophys. J.* **27**, 403–408 (1998).

108. Nicolau, D. V. *et al.* Surface hydrophobicity modulates the operation of actomyosin-based dynamic nanodevices. *Langmuir* **23**, 10846–10854 (2007).
109. van Zalinge, H. *et al.* Surface-Controlled Properties of Myosin Studied by Electric Field Modulation. *Langmuir* **31**, 8354–8361 (2015).
110. Lindberg, F. W. *et al.* Controlled Surface Silanization for Actin-Myosin Based Nanodevices and Biocompatibility of New Polymer Resists. *Langmuir* **34**, 877–8784 (2018).
111. Betzel, C., Gour, P. P. & Saenger, W. Three-dimensional structure of proteinase K at 0.15-nm resolution. *Eur. J. Biochem.* **178**, 155–171 (1988).
112. Higashi-Fujime, S., Suzuki, M., Titani, K. & Hozumi, T. Muscle actin cleaved by Proteinase K: Its polymerization and In Vitro motility. *J. Biochem.* **112**, 568–572 (1992).
113. Fan, D. & Ekinici, Y. Photolithography reaches 6 nm half-pitch using extreme ultraviolet light. *J. Micro/Nanolithography, MEMS, MOEMS* **15**, 33505 (2016).
114. Tallents, G., Wagenaars, E. & Pert, G. Optical lithography: Lithography at EUV wavelengths. *Nat. Photonics* **4**, 809–811 (2010).
115. Schirmer, M. *et al.* Chemical Semi-Amplified positive E-beam Resist (CSAR 62) for highest resolution. *Proc. SPIE* **8886**, 88860D–88860D–7 (2013).
116. Thoms, S. & Macintyre, D. S. Investigation of CSAR 62, a new resist for electron beam lithography. *J. Vac. Sci. Technol. B-Nanotechnology Microelectron.* **32**, 1–7 (2014).
117. Van Der Gaag, B. P. & Scherer, A. Microfabrication below 10 nm. *Appl. Phys. Lett.* **56**, 481–483 (1990).
118. Yasin, S., Hasko, D. G. & Ahmed, H. Comparison of MIBK/IPA and water/IPA as PMMA developers for electron beam nanolithography. *Microelectron. Eng.* **61–62**, 745–753 (2002).
119. Guo, J. L. Nanoimprint lithography: methods and material requirements. *Adv. Mater.* **19**, 495–513 (2007).
120. Nitta, T., Tanahashi, A., Hirano, M. & Hess, H. Simulating molecular shuttle movements: Towards computer-aided design of nanoscale transport systems. *Lab Chip* **6**, 881–885 (2006).
121. Lindberg, F. W. *et al.* Design and development of nanoimprint-enabled structures for molecular motor devices. *Mater. Res. Express* **6**, (2019).
122. Korten, T., Diez, S. & Jr, D. N. *Encoding Exact Cover Into Network Form and Solving it by Biocomputation.* (2019).

123. Ionov, L., Stamm, M. & Diez, S. Reversible switching of microtubule motility using thermoresponsive polymer surfaces. *Nano Lett.* **6**, 1982–1987 (2006).
124. Gao, A. *et al.* Silicon-nanowire-based CMOS-compatible field-effect transistor nanosensors for ultrasensitive electrical detection of nucleic acids. *Nano Lett.* **11**, 3974–3978 (2011).
125. Gao, A. *et al.* Enhanced sensing of nucleic acids with silicon nanowire field effect transistor biosensors. *Nano Lett.* **12**, 5262–5268 (2012).
126. Taniguchi, Y. *et al.* PGMA as a High Resolution , High Sensitivity Negative Electron Beam Resist. *Jpn J Appl Phys* **18**, 1143–1148 (1979).
127. Synytska, A., Stamm, M., Diez, S. & Ionov, L. Simple and Fast Method for the Fabrication of Switchable Bicomponent Micropatterned Polymer Surfaces. *Langmuir* **23**, 5205–5209 (2007).
128. Lyttleton, R. W. Development of solid-state nanodevices for studying proteins. (University of New South Wales, 2018).
129. Sanders, L. K. *et al.* Control of electrostatic interactions between F-actin and genetically modified lysozyme in aqueous media. *Proc. Natl. Acad. Sci.* **104**, 15994–15999 (2007).
130. Tuszyński, J. A., Portet, S., Dixon, J. M., Luxford, C. & Cantiello, H. F. Ionic Wave Propagation along Actin Filaments. *Biophys. J.* **86**, 1890–1903 (2004).
131. Balaz, M. & Månsson, A. Detection of small differences in actomyosin function using actin labeled with different phalloidin conjugates. *Anal. Biochem.* **338**, 224–236 (2005).





There is a broad range of applications for multivariable, combinatorial problems such as electronic circuit optimisation, drug development, cryptography and route optimisation, just to mention a few. These problems are very challenging to solve in a sequential manner, and instead, parallel computation methods become a necessity.

This thesis describes the development of several techniques used to expand the capabilities of parallel computation with molecular motors: how problems are encoded, the physical and chemical requirements and different architectural elements to optimise the system.